The effects of teleconnections on climate variability of the North Atlantic-European area

Ivasić, Sara

Doctoral thesis / Disertacija

2022

Degree Grantor / Ustanova koja je dodijelila akademski / stručni stupanj: **University of Zagreb, Faculty of Science / Sveučilište u Zagrebu, Prirodoslovno-matematički fakultet**

Permanent link / Trajna poveznica: https://urn.nsk.hr/urn:nbn:hr:217:767143

Rights / Prava: In copyright/Zaštićeno autorskim pravom.

Download date / Datum preuzimanja: **2025-02-17**

FACULTY OF SCIENCE

DEPARTMENT OF GEOPHYSICS

Sara Ivasić

THE EFFECTS OF TELECONNECTIONS ON CLIMATE VARIABILITY OF THE NORTH ATLANTIC-EUROPEAN AREA

DOCTORAL THESIS

Zagreb, 2022

University of Zagreb

Faculty of Science

Department of Geophysics

Sara Ivasić

THE EFFECTS OF TELECONNECTIONS ON CLIMATE VARIABILITY OF THE NORTH ATLANTIC-EUROPEAN AREA

DOCTORAL THESIS

Supervisors:

assoc. prof. Ivana Herceg Bulić, PhD

Fred Kucharski, PhD

Zagreb, 2022

Sveučilište u Zagrebu

Prirodoslovno-matematički fakultet

Geofizički odsjek

Sara Ivasić

DALJINSKI UTJECAJI NA KLIMATSKU VARIJABILNOST PODRUČJA SJEVERNOG ATLANTIKA I EUROPE

DOKTORSKI RAD

Mentori:

izv. prof. dr. sc. Ivana Herceg Bulić

dr. sc. Fred Kucharski

Zagreb, 2022.

List of abbreviations

20CRV3 – NOAA-CIRES-DOE 20th Century Reanalysis Version 3

2xCO2 - ICTP AGCM experiment forced with globally prescribed sea surface temperature anomalies and double concentration of carbon dioxide

AGCM – atmospheric general circulation model

ARC – Arctic Ocean

ATL – Atlantic Ocean

Clim – ICTP AGCM experiment containing only climatological sea surface temperatures

Ctrl – ICTP AGCM experiment forced with globally prescribed sea surface temperature anomalies

EM - El Niño Modoki

ENSO – El Niño-Southern Oscillation

EOF analysis – Empirical Orthogonal Functions analysis

EOFOPT – optimal patterns method

GH200 – geopotential height at 200 hPa level

ICTP – International Centre for Theoretical Physics

JFM – January, February, March

MSLP – mean sea level pressure

NAE area– North Atlantic-European area

NAO – North Atlantic Oscillation

NOAA – National Oceanic and Atmospheric Administration

PC – principal component

PCAVG – time series connected to the optimal pattern in the signal-to-noise optimal patterns method

PNA – Pacific North America

SIC – sea-ice concentration

SST – sea surface temperature

SSTA – sea surface temperature anomaly

TroAtl – ICTP AGCM experiment forced with sea surface temperature anomalies prescribed in the tropical Atlantic Ocean

TroInd – ICTP AGCM experiment forced with sea surface temperature anomalies prescribed in the tropical Indian Ocean

TroPac – ICTP AGCM experiment forced with sea surface temperature anomalies prescribed in the tropical Pacific Ocean

Tropics – ICTP AGCM experiment forced with sea surface temperature anomalies prescribed in the whole tropical zone

Abstract

Observed data, reanalysis and an intermediately complex general circulation model of the atmosphere (ICTP AGCM) have been employed to study the effects of teleconnections on the North Atlantic-European region as a part of this thesis. Modulation of the El Niño-Southern Oscillation (ENSO) teleconnection to the North Atlantic-European (NAE) region and its relationship with the North Atlantic Oscillation (NAO) have been tested via regression maps, running correlation, composite analysis and probability distributions. The impact of tropical ocean sea surface temperatures (SSTs) on the variability and predictable components of the late-winter atmospheric circulation over the NAE area has been investigated by employing advanced analysis techniques, such as the Empirical Orthogonal Functions (EOF) analysis and the signal-to-noise optimal patterns method. Targeted model simulations were designed to detect which ocean areas are the most important for establishing potentially predictable modes of atmospheric circulation in the NAE area. Finally, specific numerical model simulations were used to assess the impact of the warmer climate conditions on the variability and predictable components of the late winter circulation in the area of interest.

Results have shown that the ENSO teleconnection to the NAE region is not stationary. Its spatial pattern has changed from resembling the negative NAO at the surface to a different pattern with weak, statistically non-significant values after the 1970s. Meanwhile, targeted ICTP AGCM simulations confirmed the importance of sea-ice concentration and the background state of the sea surface temperatures in the modulation of the ENSO-NAE teleconnection. The change was detected at the surface and upper levels of the atmosphere in several variables and different datasets. Regarding the impact of tropical SSTs, it is suggested that the lower-boundary forcing originating from the tropics, especially the tropical Pacific, is essential for establishing the potentially predictable modes of atmospheric circulation over the North Atlantic on the seasonal and sub-seasonal scale.

Keywords: Climate variability; North Atlantic-European climate; Tropical-extratropical teleconnections; ENSO teleconnections; Boundary-forced predictability

Prošireni sažetak

Uvod i ciljevi istraživanja

Atmosfera u umjerenim širinama karakterizirana je velikom unutarnjom varijabilnošću što otežava predviđanje stanja atmosfere na sezonskim i duljim vremenskim skalama. S druge strane, atmosfera je u stalnom kontaktu s ostalim komponentama klimatskog sustava te između njih dolazi do različitih vrsta međudjelovanja. Pod glavne sastavnice klimatskog sustava pripada i ocean, te površinske temperature mora, posebno u tropskom području, svojim prinudnim djelovanjem mogu značajno utjecati na gibanja u atmosferi. Dakle, do povećanja potencijalne prediktabilnosti može doći uslijed dovoljno jakog prinudnog djelovanja na donjoj granici atmosfere ili smanjenja kaotične unutarnje varijabilnosti, tj. šuma.

Cijelo istraživanje predstavljeno u ovoj doktorskoj disertaciji usmjereno je na područje sjevernog Atlantika i Europe (eng. *North Atlantic-European region* – NAE) koje je karakterizirano velikom unutarnjom varijabilnosti atmosfere te se nalazi pod dominantnim utjecajem Sjevernoatlantske oscilacije (eng. *North Atlantic Oscillation* – NAO). Utjecaj NAO-a na sjeverni Atlantik i Europu prisutan je tijekom cijele godine, ali je najizraženiji tijekom zimske.

Izmjereni podatci, reanalize te simulacije modela opće cirkulacije atmosfere srednje složenosti (ICTP AGCM, SPEEDY) korišteni su za proučavanje daljinskih utjecaja na odabrano područje. Promjene u daljinskoj vezi El Niño-južne oscilacije (eng. *El Niño-Southern Oscillation* – ENSO) prema promatranom području i veza sa Sjevernoatlantskom oscilacijom promatrane su pomoću mapa regresije, kliznih korelacija, analize kompozita i distribucija vjerojatnosti. Uz napredne statističke metode, kao što su metoda empirijskih ortogonalnih funkcija (EOF) te metoda optimalnih polja, razmatran je utjecaj površinskih temperatura mora u tropskom području na varijabilnost i prediktabilne komponente atmosferske cirkulacije nad sjevernim Atlantikom tijekom kasne zimske sezone. Ciljane numeričke simulacije osmišljene su kako bi se utvrdilo može li se prinudno djelovanje oceana ili tropskih pojasa odabranih oceana povezati s uspostavljanjem sezonske atmosferske cirkulacije na području sjevernog Atlantika i Europe te posljedično povećati potencijalnu prediktabilnost atmosferske cirkulacije na tom području.

Prvo se poglavlje disertacije sastoji od sažetog pregleda dosadašnjih istraživanja, teorijskih temelja i motivacije za provedeno istraživanje. U drugom su poglavlju opisani korišteni podatci,

numerički model te metode analize podataka. Opis rezultata počinje u trećem poglavlju gdje su predstavljeni dokazi o nedavnom slabljenju daljinske veze El Niño-južne oscilacije prema području sjevernog Atlantika i Europe. U četvrtom poglavlju su opisani izlazni podatci integracije numeričkog modela na temelju kojih se procijenio utjecaj prinudnog djelovanja površinskih temperatura mora u pojedinim dijelovima oceana na varijabilnost i prediktabilne komponente atmosferske cirkulacije na području sjevernog Atlantika. Analiza variance signala na mjesečnoj skali i usporedba s područjem Pacifika i sjeverne Amerike prezentirana je u petom poglavlju. Šesto poglavlje sadrži opis rezultata numeričkih simulacija u uvjetima toplije klime. Razmotren je utjecaj zagrijavanja atmosfere na varijabilnost i prediktabilne komponente zimske atmosferske cirkulacije na području sjevernog Atlantika i Europe. Najvažniji rezultati izdvojeni su i sažeti u posljednjem, sedmom poglavlju.

Glavni ciljevi ovog doktorskog rada su unaprjeđivanje razumijevanja daljinskih utjecaja na klimatsku varijabilnost područja sjevernog Atlantika i Europe . Također, jedan od ciljeva bio je istraživanje vremenske varijabilnosti daljinske veze El Niño-južne oscilacije s područjem sjevernog Atlantika i Europe te opis međudjelovanja ENSO događaja sa Sjevernoatlantskom oscilacijom. U drugom dijelu istraživanja naglasak je stavljen na analizu posebno postavljenih numeričkih simulacija modelom opće cirkulacije atmosfere. Cilj je bio procijeniti doprinos oceana u tropskom pojasu na varijabilnost atmosfere te istražiti povezanost tog prinudnog djelovanja na donjoj granici modela s uspostavnom potencijalno prediktabilnih oblika sezonske atmosferske cirkulacije na području sjevernog Atlantika i Europe. Na kraju je uz pomoć istog numeričkog modela trebalo istražiti utjecaj povećanja koncentracije ugljikovog dioksida na atmosfersku cirkulaciju u kasnoj zimskoj sezoni.

Metode

Analiza empirijskim ortogonalnim funkcijama (EOF) smanjuje dimenzionalnost promatranog sustava te rješavajući problem svojstvenih vrijednosti pronalazi modove koji objašnjavaju najveći udio varijabilnosti (Kutzbach 1967). Rezultat su polja EOF-a koja su ortogonalna u prostoru i pripadajući vremenski nizovi – glavne komponente, koje su ortogonalne u vremenu. U ovom je radu EOF analiza primijenjena na srednjake ansambla numeričkih simulacija, a zatim uzimajući u obzir sve pojedinačne simulacije unutar jednog ansambla.

Metoda optimalnih polja preuzeta je iz rada Straus i sur. (2003.), a cilj joj je pronaći hijerarhiju polja koja optimiziraju omjer signal i šuma, tako prvo optimalno polje ima maksimalni pripadajući omjer signala i šuma, iduće optimalno polje drugi po veličini omjer signala i šuma itd. Kao ulazni podatci koriste se polja EOF-a, a rezultat metode su optimalna polja i pripadajući

vremenski nizovi. Ova metoda pri računu uzima u obzir sve članove ansambla numeričkih simulacija te je nije moguće primijeniti na izmjerene podatke.

Pristup procjeni signala i šuma u ansamblu numeričkih simulacija temelji se na definicijama iz rada Branković i Molteni (2004.), gdje je varijanca signala definirana preko srednjeg kvadratnog odstupanja srednjaka ansambla od klimatološkog srednjaka ansambla, dok je varijanca šuma definirana kao srednje kvadratno odstupanje pojedinih simulacija unutar ansambla od srednjaka ansambla.

Numeričke simulacije dobivene su pomoću modela opće cirkulacije atmosfere Međunarodnog centra za teorijsku fiziku Abdus Salam u Trstu, Italija (ICTP AGCM, SPEEDY). Model SPEEDY (T30, L8) ima spektralno-dinamičku jezgru, osam vertikalnih nivoa, te ekvivalentnu horizontalnu rezoluciju od 3.75° geografske širine × 3.75° geografske duljine. Unutar modela uključene su parametrizacijske sheme za konvekciju, naoblaku, kondenzaciju na velikoj skali, kratkovalno i dugovalno zračenje, površinske tokove energije i količine gibanja te vertikalnu difuziju. Model je dosada korišten u brojnim istraživanjima te se pokazao uspješnim u simuliranju glavnih karakteristika atmosferskih daljinskih veza između tropskog područja i umjerenih širina.

Rezultati i zaključak

Predstavljeni rezultati pokazali su kako daljinska veza između El Niño-južne oscilacije i područja sjeverni Atlantik-Europa nije stacionarna, te da se prostorno polje odziva promijenilo od prizemnog polja nalik na negativnu fazu Sjevernoatlantske oscilacije do odziva drugačijeg oblika i smanjene amplitude nakon 1970.-ih godina. Promjena je zabilježena pri tlu te u višim slojevima atmosfere u poljima različitih varijabli (tlak na srednjoj razini mora, geopotencijalna visina pri plohi od 200 hPa, 500 hPa i 850 hPa, temperatura, zonalni vjetar) i nekoliko skupova podataka (HadSLP i NOAA-CIRES-DOE reanaliza za 20. stoljeće). Analiza kompozita na temelju tlaka na srednjoj razini mora (HadSLP) pokazala da je uočeno slabljenje daljinske veze ENSO događaja s područjem sjevernog Atlantika i Europe. Uočeno slabljenje može se pretežno povezati sa smanjenjem frekvencije istovremenog nastupa El Niño događaja s negativnom fazom NAO-a.

Osmišljene su numeričke simulacije u kojima su modelu opće cirkulacije atmosfere SPEEDY zadane različite kombinacije smanjene i povećane koncentracije morskog leda, tj. klimatologije površinskih temperatura mora u odabranom ranijem (1979.-1999.) i kasnijem razdoblju (2005.-2015.) kako bi se istražila uloga ta dva faktora na promjene ENSO-NAE daljinske veze. Simulacije su ukazale na suprotan učinak odabranih faktora. Smanjenje koncentracije morskog leda na

području Arktika djeluje u smjeru jačanja promatrane daljinske veze, s prostornim poljem nalik na Sjevernoatlantsku oscilaciju. S druge strane, nedavne promjene klimatoloških vrijednosti površinske temperature mora, posebice na području Arktika i Atlantskog oceana, doprinose slabljenju povezanosti ENSO događaja sa sjevernim Atlantikom i Europom.

Pomoću istog numeričkog modela opće cirkulacije atmosfere (SPEEDY) provedene su numeričke simulacije u razdoblju od 1854. do 2010. godine u kojima je zadano ograničeno područje djelovanja anomalija površinskih temperatura mora na donju granicu atmosfere, dok su u ostatku domene korištene samo klimatološke vrijednosti SST-a. Provedeno je šest različitih numeričkih eksperimenata, s prinudnim djelovanjem anomalija SST-a u tropskom području Atlantika (30° S-30° N, 100° W-20° E), tropskom Pacifiku (30° S-30° N, 120° E-60° W), tropskom Indijskom oceanu (30° S-30° N, 30° -120° E), cijeloj tropskoj zoni (30° S-30° N, 0°-360° E) te uz globalno zadane anomalije SST-a (90° S-90° N, 0°-360° E). Unutar svakog od opisanih numeričkih eksperimenata provedeno je 35 simulacija koje se međusobno razlikuju po početnim uvjetima u prvoj godini integracije modela koja je odbačena iz daljnje analize. Dodatno je proveden eksperiment bez prinudnog djelovanja na donjoj granici atmosfere, tj. samo uz klimatološke vrijednosti SST-a.

Simulacije su pokazale da prinudno djelovanje mora u tropskom području, posebice u tropskom Pacifiku, dovodi do uspostave određenih oblika polja geopotencijalne visine pri izobarnoj plohi od 200 hPa (GH200) te se može posredno iskoristiti u svrhu poboljšanja potencijalne prediktabilnosti zimske atmosferske cirkulacije na području sjevernog Atlantika i Europe. Odziv prinudnog djelovanja površinskih temperatura mora na atmosferu uočen je u polju EOF-a izračunatih na temelju srednjaka ansambla te prvom polju dobivenom metodom optimalnih polja. Relativno visoka razina korelacije vremenskog niza prve glavne komponente izmjerenih površinskih temperatura mora s prvom glavnom komponentom GH200, te vremenskim nizom prvog optimalnog polja, dodatno su potvrdili povezanost prinudnog djelovanja SST-a u tropskom području i potencijalno prediktabilnih oblika sezonske atmosferske cirkulacije nad područjem sjevernog Atlantika i Europe u kasnoj zimskoj sezoni.

Analiza mjesečnih vrijednosti varijance signala GH200 nad područjem sjevernog Atlantika i Europe provedena je za već opisane eksperimente modela SPEEDY sa zadanim prinudnim djelovanjem površinskih temperatura mora na ograničenim područjima u razdoblju od 1855. do 2010. godine. Prostorno polje varijance signala razlikuje se od polja Sjevernoatlantske oscilacije koje objašnjava najveći udio varijabilnosti atmosferske cirkulacije područja sjevernog Atlantika i Europe zimi. Prostorno polje varijance signala nad NAE područjem ima maksimum nad sjevernim Atlantikom koji je najjače izražen kada se pri analizi u obzir uzmu samo ENSO godine,

koje su izdvojene na temelju jačine Niño3.4 indeksa u kasnoj zimskoj sezoni. Međutim, sličan prostorni oblik varijance signala, ali slabije izražen, zadržava se i unutar ne-ENSO kompozita (tj. godinama bez ENSO događaja). Najveća razlika između ENSO i ne-ENSO kompozita dobivena je u slučaju eksperimenta s prinudnim djelovanjem anomalija površinskih temperatura mora zadanim samo u tropskom Pacifiku.

Naposljetku, koristeći rezultate modela SPEEDY, napravljena je usporedba kontrolnog ansambla numeričkih simulacija sa simulacijama sa zadanom dvostrukom koncentracijom ugljikovog dioksida, ali uz iste rubne uvjete. Sve simulacije provedene su i analizirane za razdoblje između 1855. i 2010. godine. Zabilježeno je povećanje varijance signala u veljači i ožujku za ENSO kompozit u ansamblu s povećanom koncentracijom CO_2, što ukazuje na značajnu ulogu ENSO događaja na klimatsku varijabilnost područja sjevernog Atlantika i Europe u uvjetima toplije klime.

Ključne riječi: Klimatska varijabilnost; klima područja sjevernog Atlantika i Europe; daljinske veze El Niño-južne oscilacije; potencijalna prediktabilnost

Table of contents

1. Introduction

The atmosphere in the midlatitudes is characterised by its large internal variability (Colfescu and Schneider 2017), which makes seasonal predictions difficult. For example, this internal variability, or "climate noise", can be up to ten times larger than the boundary-forced ENSO signal (Lopez and Kirtman 2019). Therefore, the increase in potential predictability can occur due to the strengthening of the boundary forcing or a decrease of the chaotic, internal variability.

Due to its large heat capacity and stable stratification, the ocean is considered to be a slow component of the climate system. The evaporation of water at the air-sea boundary leads to the transfer of latent heat from the ocean to the atmosphere (Behera 2020). Therefore, sea surface temperatures (SSTs) can act as a source of heat for the atmosphere. Also, the atmosphere and the surface below can have different angular momentum. This difference is especially pronounced as air travels in the meridional direction since angular momentum increases with the distance from the planetary axis of rotation. The main two ways in which the atmosphere exchanges angular momentum with the surface are by low-level wind shear and small-scale wave motions over topography (Toniazzo et al. 2020). Depending on the intensity of this oceanic boundary forcing, a significant impact on the seasonal predictability of the atmosphere in the midlatitudes is possible.

1.1. North Atlantic Oscillation

The North Atlantic Oscillation (NAO) is an atmospheric phenomenon characterized by a simultaneous fluctuation between the Icelandic low and the Azores high-pressure systems (Jung et al. 2003). A schematic overview of the state of the atmosphere and the ocean during the positive and negative NAO phase is given in Fig. 1.1 made by Wanner et al. (2001). During winter, the North Atlantic-European area is under the NAO's dominant influence, accounting for around 40% of the sea level pressure variability (Hurrell et al. 2003). The NAO impact extends from eastern North America to western and central Europe and is reflected in the temperature, precipitation, intensity and location of the North Atlantic storm tracks (Wettstein and Wallace

2010; Woollings et al. 2015). The NAO index based on the principal component (PC) of the sea level pressure (Fig. 1.2) over the Atlantic (20°-80° N, 90° W-40° E) is often used to measure the NAO (Hurrell 1995) alongside other, station-based NAO indices.

According to the existing evidence, the NAO may be a result of the internal atmospheric dynamical processes via the interaction between eddies and the mean flow (Lau 1981; Limpasuvan and Hartmann 1999; Vallis et al. 2004). Therefore, the NAO is a mode of climate variability with limited predictability beyond the weather timescales. However, recent studies point to the possible predictability of the NAO through driving physical climate processes, such as tropical precipitation and the North Atlantic subtropical gyre (Scaife et al. 2014, 2017; Domeisen et al. 2018).
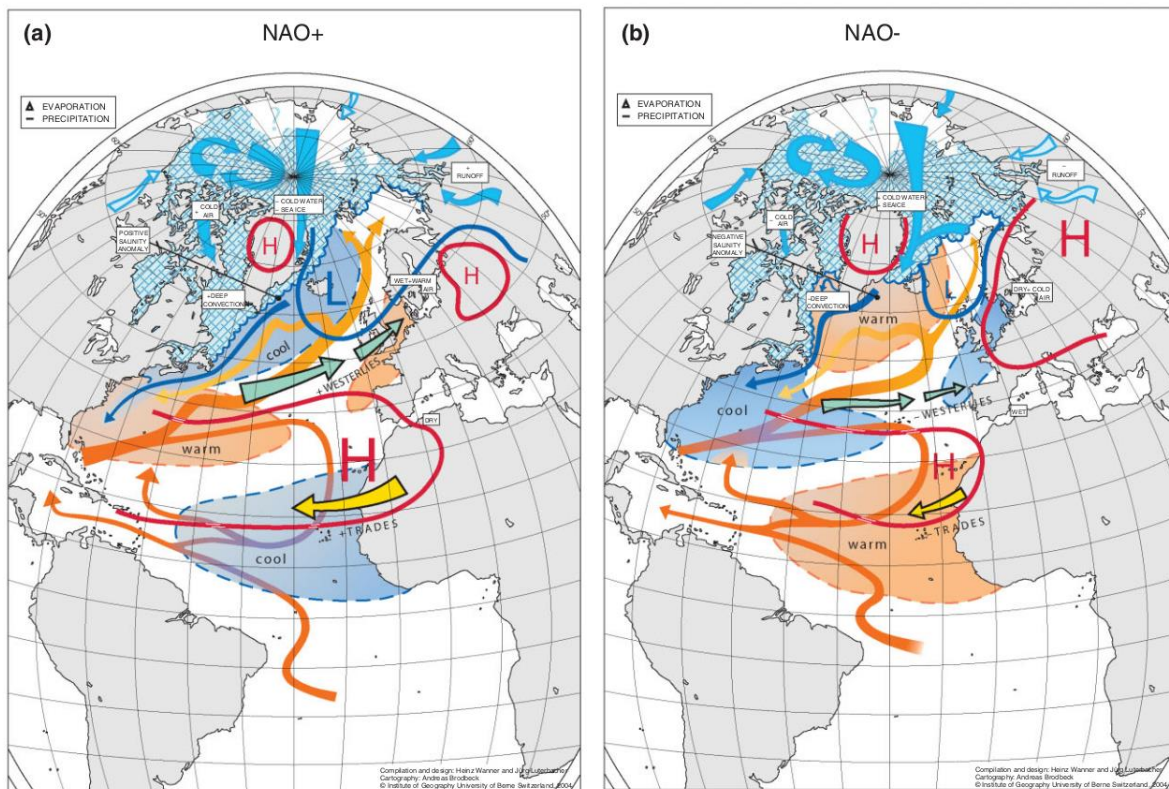

Figure 1.1 Overview of the (a) positive phase and (b) negative phase of the North Atlantic Oscillation. Here the shading represents the SST and the extent of sea ice, while arrows indicate the atmospheric, river and ocean circulation. The solid contours represent the sea level pressure systems. White rectangles label important processes and characteristic climate conditions. Source: Wanner et al. (2001) via Pinto and Raible (2012).
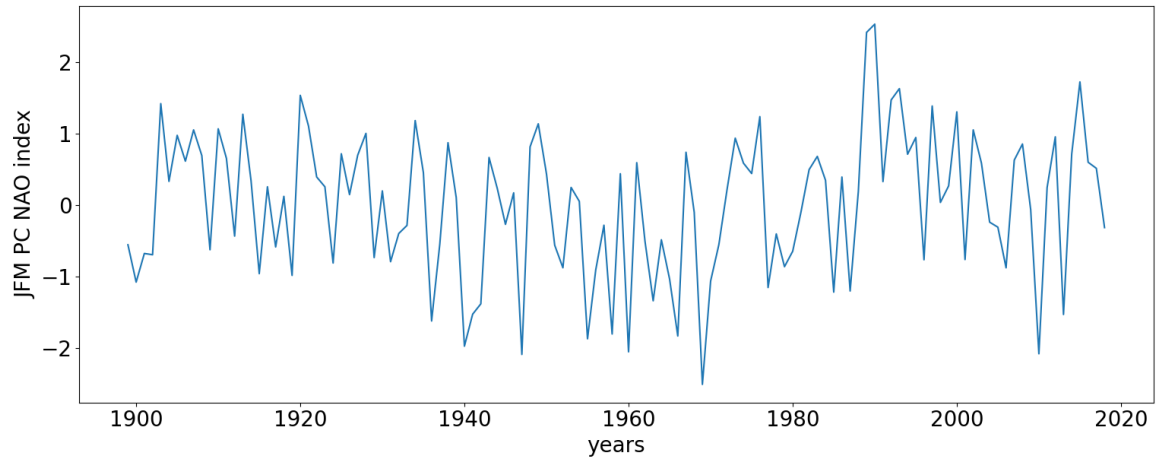
Figure 1.2 JFM PC-based Hurrell NAO index for the 1899-2018 period. The NAO index is calculated as the first principal component of sea level pressure averaged over the Atlantic sector (20°-80° N, 90° W-40° E).

1.2. El Niño-Southern Oscillation

El Niño-Southern Oscillation (ENSO) is a phenomenon driven by the atmosphere-ocean interactions in the tropical Pacific. During normal conditions (Fig. 1.3a), trade winds push the surface water mass from the east towards the western Pacific, characterized by warm sea surface temperatures, i.e., the western Pacific *warm pool*. Here, the warm surface of the ocean supports deep atmospheric convection, and this raising air mass establishes the ascending branch of the Walker Circulation. Descending branch of the Walker Circulation cell is located over the eastern Pacific, where the air subsides over the area containing colder sea surface temperatures, often referred to as the *cold tongue*. These colder waters are transported from the deeper layers of the ocean through equatorial upwelling. The thermocline has an east-west tilt in neutral conditions, which is related to the strength of the trade winds (McPhaden et al. 2020).

During La Niña (Fig. 1.3b), neutral conditions are intensified, i.e., strengthened trade winds support a sharper westward thermocline tilt, followed by the shift of the warm pool further west and more intense upwelling in the eastern Pacific. On the other hand, trade winds are weaker during El Niño events (Fig. 1.3c). Therefore, the tilt of the thermocline is less pronounced, and there is a shift of the warm pool to the east, with decreased upwelling in the cold tongue region. The centre of convection and heavy rainfall, previously located in the western Pacific, also moves eastward. Anomalous warming of the ocean surface leads to even weaker trade winds in a reinforcing positive feedback mechanism, called the Bjerknes feedback (Bjerknes 1969). The coupled ocean-atmosphere system stays inside this feedback loop until the delayed negative feedback mechanisms in oceanic dynamics work towards the decay of the El Niño event by transporting the anomalously warm water from the surface away from the equator (e.g., Schopf

and Suarez 1988; Jin 1997). The discharge of heat accumulated in the tropical Pacific restores the neutral conditions. However, if the discharge mechanisms are strong enough, La Niña conditions can be established (McPhaden et al. 2020).

The Niño3.4 index (Fig. 1.4a), based on SST anomalies averaged over the region 5° S-5° N, 120°-170° W (Fig. 1.4b), is commonly used in various teleconnection studies because of its strong correlation with climate anomalies in remote regions (McPhaden et al. 2020). The quasi-periodic nature of the ENSO phenomenon can be detected by examining the Niño3.4 time series, as the ENSO events occur approximately every 2-7 years.

ENSO has been the focus of scientific research because of its global impacts on climate (Ropelewski and Halpert 1989; Brönnimann 2007; Lin and Qian 2019), predictability (Ren et al. 2019), complex physical mechanisms (Barnett et al. 1991; Wang and Picaut 2004), and the possibility of influencing seasonal forecasts (Smith and O'Brien 2001; van Oldenborgh 2005; Scaife et al. 2014). In mid-latitudes, the ENSO-related signal is often modified and masked by the strong internal variability of the atmosphere and other stronger local influences.

The physical mechanisms through which ENSO forces climate anomalies in distant parts of the world include tropospheric propagation of the atmospheric Rossby waves (Horel and Wallace 1981; Hoskins and Karoly 1981; Kingtse and Livezey 1986). Alongside the tropospheric pathway, existing evidence shows that the tropical Pacific-NAE teleconnection can also be established via the stratosphere. Vertically propagating waves associated with ENSO may perturb the polar stratosphere, which in turn affects the troposphere (Bell et al. 2009; Iza and Calvo 2015; Calvo et al. 2017; Domeisen et al. 2019). In addition to the wintertime signal, the stratosphere may also support a prolonged ENSO impact from winter to the following spring by the persistence of the winter ENSO signal (Herceg-Bulić et al. 2017).

1.3. ENSO-NAE teleconnection

Despite certain disagreements between existing evidence, most authors report a detectable ENSO-related signal in the European climate anomalies. The canonical wintertime El Niño events are associated with a southward shift of the Atlantic cyclone track, more frequent cyclonic weather types over the NAE region and increased precipitation in the Mediterranean (Brönnimann 2007). Meanwhile, the La Niña phase is mainly connected to the opposite pattern compared to El Niño.

Describing the spatial pattern of the ENSO-NAE teleconnection, some authors state that during late winter, ENSO impact on the European region projects onto the NAO pattern, with El Niño

resembling the negative NAO and La Niña the positive NAO phase (Brönnimann 2007; Bell et al. 2009; Domeisen et al. 2015). However, Mezzina et al. (2019) argued that these two phenomena produce similar surface pressure patterns in the NAE area, but the dynamical mechanisms of their establishment are different, which is indicated by the upper-tropospheric fields.

Various atmospheric processes can impact and modulate the ENSO signature over the NAE area. A vital contribution to the observed variety of the ENSO teleconnections is the diversity of ENSO events, both in strength and pattern. ENSO diversity can produce various responses over the NAE region (Toniazzo and Scaife 2006; Li and Lau 2012; Zhang et al. 2015, 2019b; Calvo et al. 2017).

According to the increasing amount of evidence, there is a need to distinguish early from late winter when examining the ENSO impact on the NAE area, because of the seasonally-dependent role of the tropical Pacific and Indian Ocean in establishing the ENSO-NAE teleconnection (Ayarzagüena et al. 2018; King et al. 2018, 2021; Abid et al. 2020; Joshi et al. 2021).

The state of ENSO teleconnections under global warming will depend on the magnitude of the greenhouse gas forcing, changes in the mean state of the tropical Pacific and ENSO itself, and changes in other ocean basins (Taschetto et al. 2020). However, most state-of-the-art climate models point toward a strengthening and an eastward shift of the ENSO rainfall response in the equatorial Pacific, which would lead to the eastward intensification of the extratropical ENSO-related teleconnections (Cai et al. 2021). Also, climate models suggest that stronger ENSO events may become more frequent in the future due to the increasing greenhouse gas forcing (Cai et al. 2020).

(a) neutral conditions
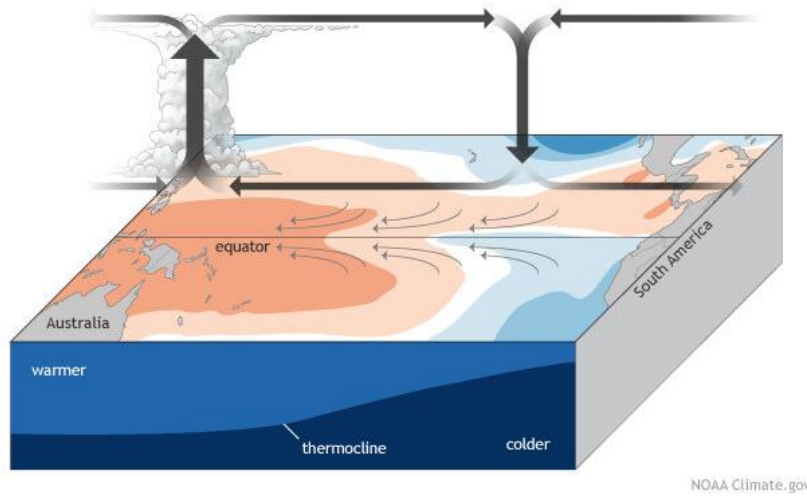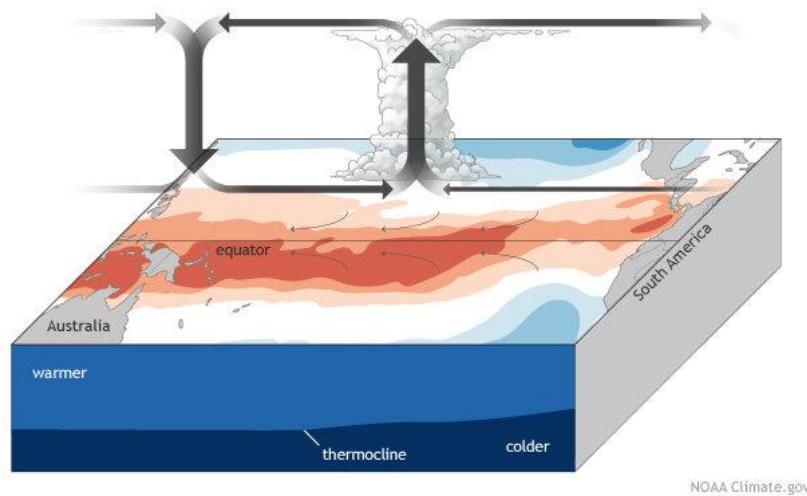

(b) La Niña conditions
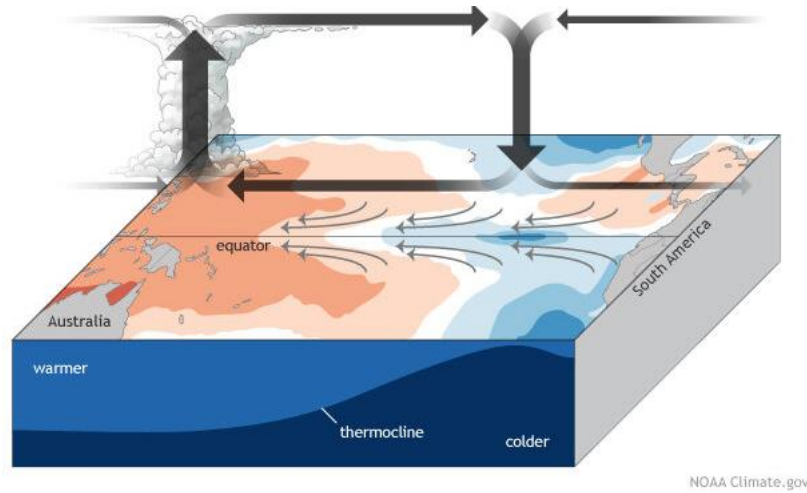
(c)El Niño conditions

Figure 1.3 Overview of the state of the atmosphere-ocean system in the tropical Pacific during (a) neutral, (b) La Niña, and (c) El Niño conditions. Shading indicates the sea surface temperatures, ranging from dark blue (cold) to red (warm). Thermocline depth and incline are depicted on the front-facing side of each

cuboid. Arrows indicate the direction of atmospheric circulation. The position of the clouds in each panel indicates the shifting centre of deep atmospheric convection. Climate.gov schematic by Emily Eng. Source: https://www.climate.gov/news-features/blogs/enso/rise-el-ni%C3%B1o-and-la-ni%C3%B1a (Accessed: 10 August 2022).
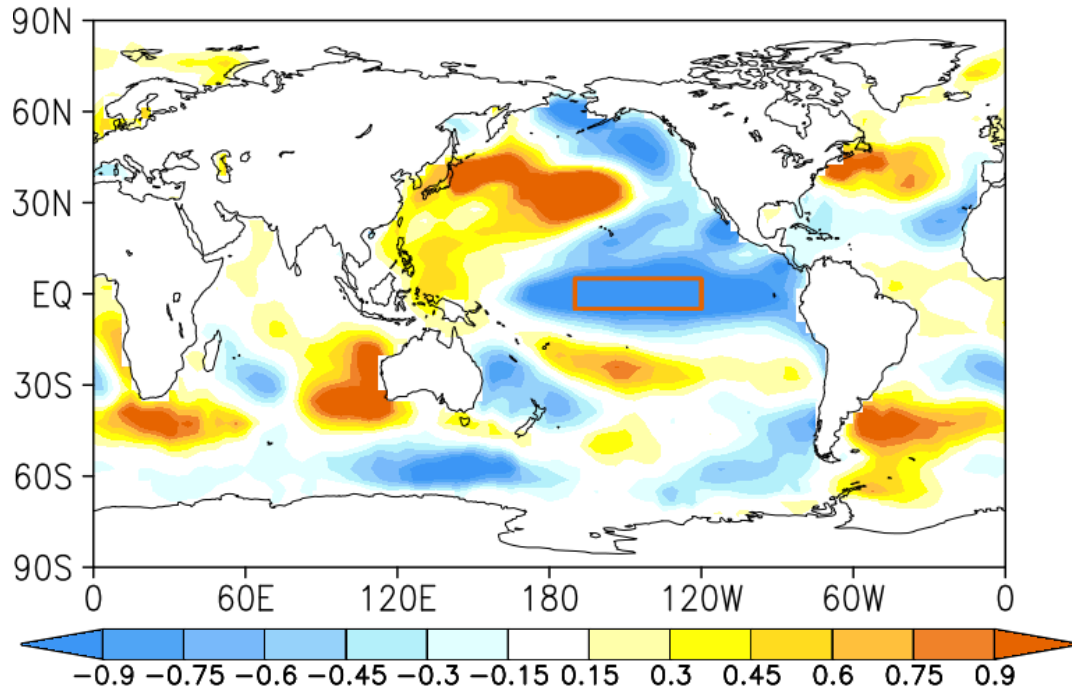
(a) JFM Niño3.4 index
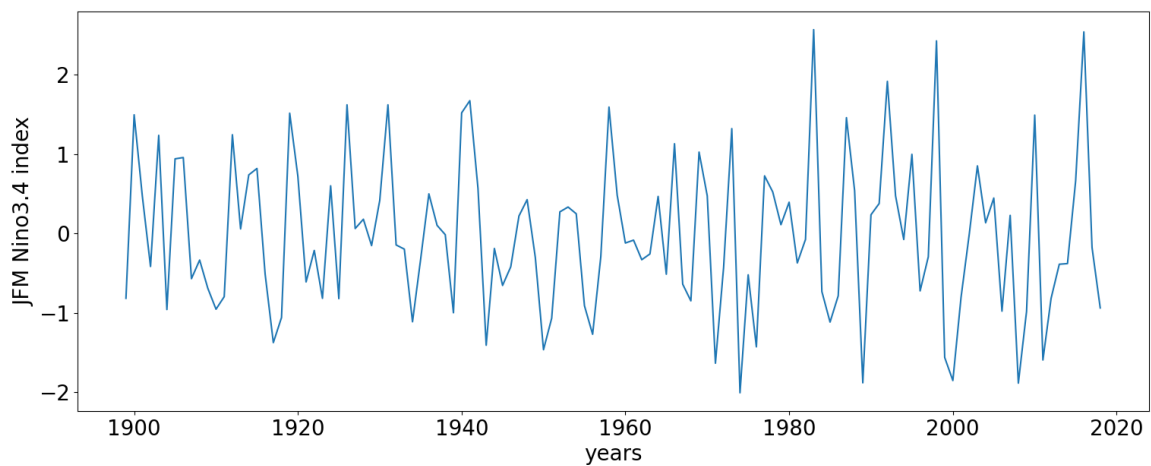
(b) Niño3.4 region

Figure 1.4 (a) JFM Niño3.4 index [K] for the period 1899-2018 based on SST anomalies from the HadISST dataset. (b) Global SST anomalies [K] in January 2000 from the NOAA ERSST V3 dataset, with the red rectangle in the tropical Pacific highlighting the Niño3.4 region (5° S-5° N, 120°-170° W).

1.4. Other remote influences

The ENSO-related atmospheric teleconnections can be impacted by the variability and dynamical mechanisms originating from the other oceans (Taschetto et al. 2020). The need to study ENSO teleconnections in an inter-basin framework has been highlighted recently. To further improve seasonal predictions, the effect that different ocean basins have on each other and climate variability, in general, should be understood more clearly (Cai et al. 2019; Wang 2019).

While a large number of teleconnection studies so far have been focused on seasonal means (e.g., Brönnimann 2007 and references therein), to obtain a clearer picture of the physical mechanisms in their background it is important to also consider the sub-seasonal scale (e.g., King et al. 2018). During the late-winter season, the wave train originating in the tropical Pacific is predominantly responsible for the ENSO influence on the NAE region. However, the interactions between the tropical Pacific, Indian Ocean and the Atlantic seem to be essential for establishing the ENSO-NAE teleconnection in early winter (Ayarzagüena et al. 2018; Abid et al. 2020; Joshi et al. 2021). In addition, the role of the Indian Ocean on the NAE climate variability has also been emphasized in other studies (Hoerling et al. 2001, 2004).

Meanwhile, the Atlantic as the nearest ocean basin has a recorded impact on the NAE climate variability as well (Venzke et al. 1999; Terray and Cassou 2002; Sutton and Hodson 2003). ENSO events affect the Walker Circulation, which also impacts the tropical Atlantic SSTs. The change in the tropical Atlantic SSTs can, in turn, modify the Atlantic section of the Hadley Circulation and cause changes in the storm tracks, NAO, and the Azores High, and trigger Rossby waves propagating towards the extratropics (Taschetto et al. 2020).

1.5. Research objectives

While the ENSO teleconnection towards the Pacific-North American region (Ropelewski and Halpert 1986; Chapman et al. 2021) and Australia (Power et al. 1999) has been extensively researched and well-understood, there are still several open questions regarding the ENSO impact on the NAE region. These unresolved issues include mechanisms of establishing the ENSO-NAE teleconnection (Bell et al. 2009; Ineson and Scaife 2009; Jiménez-Esteve and Domeisen 2018; Domeisen et al. 2019), (a)symmetry of the NAE atmospheric response to the El Niño and La Niña phase (Lopez and Kirtman 2019; Mezzina et al. 2020), the impact of diversity of ENSO events (Zhang et al. 2015; Calvo et al. 2017; Hardiman et al. 2019), the relationship between ENSO and NAO (Zhang et al. 2019a; Mezzina et al. 2020).

Motivated by these unresolved issues regarding the effects of teleconnections on the climate variability of the North Atlantic-European area, the present thesis aimed to further our general understanding of the topic, including different mechanisms that are responsible for the modification of the teleconnections toward the NAE region.

One of the main objectives of this thesis included the investigation of the ENSO-NAE teleconnection during different periods and the exploration of its temporal variability. Also, the aim was to test the co-occurrence of the two ENSO phases during a particular phase of the NAO in different periods, and the general characteristics of the ENSO-NAO relationship.

The next goal was to study the sub-seasonal-to-seasonal impact of the oceans in the tropical zone on the climate variability of the winter atmospheric circulation over the NAE area. The possible influence of the boundary forcing in the form of remote SSTs in establishing potentially predictable patterns was tested by designing and analysing targeted numerical simulations made with an atmospheric general circulation model.

Finally, the research goal was to assess the impact of warmer climate conditions on the variability and predictable components of the winter atmospheric circulation over the NAE area by comparing the control ensemble with an ensemble of numerical simulations prescribed with a double amount of the carbon dioxide forcing.

2. Data and methods

Observed data, reanalysis, and the atmospheric general circulation model used in investigating the effects of teleconnections on the North Atlantic-European region are listed in the following chapter. The methods employed for analysing the same data are also described.

2.1. Observed data

The Hadley Centre (HadSLP2r) dataset was used (Allan and Ansell 2006) to analyse the mean sea level pressure (MSLP) response to ENSO events (Chapter 3). The HadSLP2r dataset consists of monthly sea level pressure values on a 5° latitude by 5° longitude global grid. In this thesis, HadSLP values for the period between 1899 and 2018 were used. In addition, monthly values of several other meteorological parameters (MSLP, zonal wind, geopotential height, temperature, surface ice concentration) were taken from the NOAA-CIRE-DOE 20th Century Reanalysis V3 dataset (hereafter 20CRV3; Slivinski et al. 2019). The 20CRV3 contains data on a 1° latitude by 1° longitude global grid, also used in the period between 1899 and 2015.

For studying the relationship between ENSO and NAO events (Chapter 3), ENSO years were categorized according to the strength of the winter (January, February, March; hereafter JFM) HadISST Niño3.4 index (Rayner et al. 2003). Here, monthly SSTs from the HadISST dataset were used for the period from January 1899 to December 2018, in the spatial resolution of 1° latitude by 1° longitude. The Niño3.4 index is defined as the average of SST anomalies over the area 5° S-5° N and 120°-170° W (Fig. 1.4). NAO years in the period 1899-2018 were classified based on the strength of the JFM Hurrell NAO index (Hurrell 1995), calculated as the first principal component (PC1) of JFM MSLP over the North Atlantic sector (20°-80° N and 90° W-40° E). There are three categories for both of the standardized indices: negative ($I < -0.5\,\sigma$), neutral ($-0.5\,\sigma < I < 0.5\,\sigma$), and positive ($I > 0.5\,\sigma$).

For studying the ENSO impact on the signal variance in the ICTP AGCM simulations (Chapter 5), a stricter threshold is imposed for classifying ENSO events, where ENSO years are considered those with a standardized JFM HadISST Niño3.4 index greater than one standard deviation. Meanwhile, the non-ENSO or the neutral category remains unchanged.

2.2. Numerical model ICTP AGCM (SPEEDY)

General circulation models of the atmosphere are valuable tools for investigating predictability and, as such, have been used in various studies focusing on tropical-extratropical teleconnections. Numerical models of the atmosphere can provide an estimate of the signal and noise based on a large number of simulations with identical boundary forcing, which differ only in initial conditions. One of the shortcomings of this modelling approach, which cannot be dismissed, is the possible model bias.

In the research presented in this thesis, an intermediately complex general circulation model of the atmosphere developed at the Abdus Salam International Centre for Theoretical Physics has been employed. The ICTP AGCM, nicknamed SPEEDY, has eight vertical sigma levels (L8) and spectral triangular truncation at wavenumber 30 (T30), corresponding to a horizontal resolution of 3.75° longitude by 3.75° latitude (Molteni 2003; Kucharski et al. 2006a, 2013). The model's base is a hydrostatic spectral dynamical core from the Geophysical Fluid Dynamics Laboratory (Held and Suarez 1994). ICTP AGCM is a spectral transform model with a vorticity-divergence form, described by Bourke (1974), with the semi-implicit treatment of gravity waves. Also, the model utilises the σ-coordinate.

The model includes parametrisation schemes for surface fluxes of momentum, heat and moisture, shortwave and longwave radiation, vertical diffusion, large-scale condensation and convection due to its relatively coarse resolution. A single-layer thermodynamic model is used to calculate the land and sea-ice temperature anomalies(Kucharski et al. 2013). The NOAA ERSST V3 dataset (Smith et al. 2008) is used for the SST input, while the sea-ice climatology comes from the Hadley Centre's HadISST dataset (Rayner et al. 2003). The NOAA ERSST V3 contains the SST data on a 2° latitude by 2° longitude global grid covering the period between January 1854 and February 2020. Meanwhile, the HadISST dataset contains monthly sea-ice concentration records, starting from January 1870 to the present day, in the spatial resolution of 1° latitude by 1° longitude.

ICTP AGCM has been used in numerous studies, including those examining global ENSO teleconnections (Kucharski et al. 2006b, 2013; Herceg-Bulić and Branković 2007; Herceg-Bulić and Kucharski 2012; Dogar et al. 2017; Ruggieri et al. 2017; Herceg-Bulić et al. 2017; Abid et al. 2020). It has been found that the model can faithfully reproduce the key characteristics of the examined tropical-extratropical teleconnections during different seasons. Abid et al. (2020) recently showed that the ICTP AGCM could be used for studying sub-seasonal conditions. Also,

this AGCM was used to examine the sensitivity of the ENSO teleconnections on the model's mean state over the Pacific-North American region (Di Carlo et al. 2022).

In chapters four, five and six, all ICTP AGCM data were linearly detrended and treated with a high-pass filter with a cut-off period of 11 years to remove long-term trends before applying any of the analysis methods.

2.3. EOF analysis

Climate variability stems from complex nonlinear connections between many degrees of freedom in the climate system. The empirical orthogonal functions (EOF) analysis is one method for reducing the observed system's dimensionality and identifying important patterns that explain most of the variability. The EOF method seeks spatial patterns and the associated time series, which explain the largest amount of variability of a specific variable (Kutzbach 1967). The patterns are orthogonal, while the corresponding time series are mutually uncorrelated.

The EOF analysis is commonly used to extract individual atmospheric variability modes and study teleconnections. In chapters 3 and 6, the EOF analysis was applied in two different ways - to the ensemble means and to all ensemble members in the ICTP AGCM experiments. Also, the EOF analysis was applied to the data from the North Atlantic-European region (20°-80° N, 90° W-60° E), highlighted in Fig. 2.1.
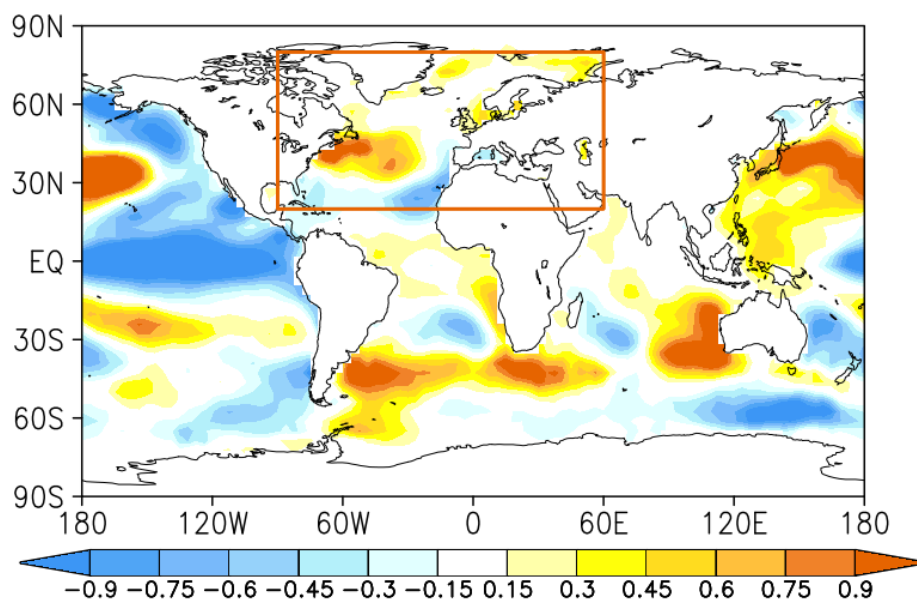
Figure 2.1 Global SST anomalies [K] in January 2000 with the red rectangle highlighting the North Atlantic-European region (20°-80° N, 90° W-60° E). Original data was taken from the NOAA ERSST V3 dataset.

2.4. Signal and noise analysis

The signal and noise analysis were employed to assess the boundary-forced predictability over the North Atlantic-European region. This analysis is based on the definitions from the paper by Branković and Molteni (2004). Signal variance (Eq. 2.1) is defined as the deviation of the ensemble mean from the climatological mean of the ensemble mean,

$$\sigma_s^2 = \frac{1}{N} \sum_{j=1}^{N} \left(\bar{x}_j - \bar{x} \right)^2, \tag{2.1}$$

where $\bar{x}_j = \frac{1}{M} \sum_{i=1}^{M} x_{ij}$ represents the ensemble mean in the j-th year and the term x_{ij} denotes the i-th ensemble member in the j-th year. Also, N represents the number of years, while M is the number of ensemble members. Meanwhile, the noise variance (Eq. 2.2) is defined by the deviations of particular simulations within the ensemble (x_{ij}) from the ensemble mean ($\bar{x}_j$),

$$\sigma_n^2 = \frac{1}{N} \sum_{j=1}^{N} \left[\frac{1}{M} \sum_{i=1}^{M} \left(x_{ij} - \bar{x}_j \right)^2 \right]. \tag{2.1}$$

This method cannot be applied to observations since an ensemble is needed to assess the signal and noise variance.

2.5. Signal-to-noise optimal patterns

Another way of determining the extent of the boundary-forcing is by finding the signal-to-noise optimal patterns using the method described by Straus et al. (2003). An equivalent method can be found in Venzke et al. (1999). The idea behind this approach is to calculate the spatial configurations of a particular variable which optimizes the signal-to-noise ratio. This method takes EOFs as input and calculates the optimal patterns (EOFOPT) and their associated time series, sorted according to the signal-to-noise ratio (i.e., the first mode has the maximal signal-to-noise ratio, the second mode has the second-highest signal-to-noise ratio, etc.). The signal for each optimal pattern is defined as the temporal variance of the ensemble mean of the time series connected to each optimal pattern. Meanwhile, the noise is defined by the average variance of the time series connected to each optimal pattern within the ensemble.

While the EOF method solves the eigenvalue problem, the optimal patterns method solves the generalized eigenvalue problem. This method cannot be applied to observations since it utilizes

all ensemble members. It is important to note that no information about the lower-boundary forcing (i.e., SST anomalies) is considered in calculating the optimal patterns.

In this thesis, the signal-to-noise optimal patterns method was applied to geopotential height at 200 hPa level from the ICTP AGCM experiments in the North Atlantic-European region (Fig. 2.1).

2.6. ENSO and non-ENSO signal composites

The composite analysis includes an assumption that the essential characteristics of the SST forcing can be contained in one index. Here, the Niño3.4 index was defined using the NOAA ERSST V3 SST anomalies (Smith et al. 2008) in the period 1855-2010 averaged over the area: 5° S-5° N and 120°-170° W (Fig. 1.4b). Composites are then averages of the signal variance of geopotential heights at 200 hPa (GH200) for the years when the Niño3.4 index is above or below a certain threshold.

The signal variance was calculated based on Eq. 2.1 for all years, then ENSO and non-ENSO years, respectively, to detect the extent of the ENSO influence on the monthly signal variance of GH200 over the NAE region (30°-60° N, 50° W-30° E) in the ICTP AGCM idealized experiments for the period 1855-2010. According to the value of the late-winter Niño3.4 index (January, February, March; JFM), 53 out of the total 156 years were categorised as ENSO years ($I < -1.0\sigma$ or $I > 1.0\sigma$), while 57 years were sorted into the non-ENSO category ($-0.5\sigma < I < 0.5\sigma$).

2.7. Other methods and statistical tests

Each grid point in a regression map (Chapter 3) represents a regression of a dependent variable onto an independent one, where the grid matches the dimensions of the variable which has both spatial and temporal coordinates. Therefore, the value of the regression map in a particular grid point is the expected value of the dependent variable departure given a unit departure in the independent variable. Units of the regression map values are based on the units of the input variables. The statistical significance of the regression maps was determined by a one-tailed Student's t-test at the 90% confidence level Meanwhile, the statistical significance of the calculated correlation coefficients was determined according to the two-tailed Student's t-test at the 95% significance level (Chapters 3-6).

In hypothesis testing, the p-value signifies the probability of obtaining a result at least as extreme as the test value under the assumption that the null hypothesis is correct. The evidence for the rejection of the null hypothesis can be deemed sufficient in case the p-value is less than

or equal to the chosen significance level. Therefore, the level of significance and the conclusion of a certain hypothesis test can be succinct by indicating the p-value.

The code for the signal-to-noise optimal pattern calculates the standard F-statistic to enable testing of the statistical significance of the signal-to-noise ratio associated with each of the optimal patterns (Chapter 4). The F-distribution is the null distribution for the ratio of variances (Wilks 2019). The level of statistical significance is determined according to the value of the F-statistic and the number of degrees of freedom. Here, the degrees of freedom are based on the number of years in each numerical simulation and the number of ensemble members in each model experiment.

3. The recent weakening of the ENSO-NAE teleconnection

In this chapter, we examine the possible variation of ENSO and NAO co-occurrence to test the theory that the ENSO impact on the North Atlantic-European region projects onto the NAO pattern in the late winter season. Results indicate non-stationarity of the ENSO teleconnection to the NAE area, which is found both in observed and modelled data. Also, the potential cause for the weakening of this ENSO teleconnection is proposed, considering the decrease of the Arctic sea-ice cover and the background SST state.

Text and figures were first published in *Climate Dynamics*: Ivasić S, Herceg-Bulić I, King MP (2021) Recent weakening in the winter ENSO teleconnection over the North Atlantic-European region. *Clim Dyn*. https://doi.org/10.1007/s00382-021-05783-z

3.1. Observational evidence

3.1.1. Variation of ENSO and NAO co-occurrence

According to the scientific literature concerning the ENSO-NAE teleconnection in late winter, it is often thought that the ENSO impact on the NAE region projects onto an NAO-like pattern at the surface level, with the positive ENSO phase being associated with the negative NAO. In that case, one would expect the ENSO index (which measures the strength and phase of an ENSO event) to be correlated with the NAO index (which describes the spatial distribution and strength of a particular NAO event). Therefore, probability distributions of NAO phases during the three ENSO states (Figs. 3.1 and 3.2) were made to examine the relative occurrence of ENSO and NAO events. ENSO events are sorted according to the value of the JFM Niño3.4 index, where the ENSOpos signifies the positive or warm ENSO phase (El Niño), negative or cold ENSO phase is labelled as ENSOneg, while ENSO0 stands for the neutral events. Following the same principle, the NAO events are sorted into positive, negative and neutral categories according to the value of the PC-based Hurrell NAO index.

Figure 3.1 shows how often a particular ENSO phase was accompanied by the negative, positive or neutral NAO in the 1899-2018 period. According to the HadSLP data, there are 40 ENSOneg events and 35% of them are associated with the positive NAO, 30% with the negative phase of the NAO and 35% with its neutral phase. However, the distribution for the 33 ENSOpos events is slightly different. Among all recorded ENSO events, 49% are accompanied by negative NAO, 30% by positive and 21% by neutral NAO. At first glance, distributions presented in Fig. 3.1 agree with the previous findings that El Niño is connected to the negative NAO (e.g., Brönnimann 2007; Bell et al. 2009; Domeisen et al. 2015) because a larger number of ENSOpos events co-occurs with the negative phase of the NAO.
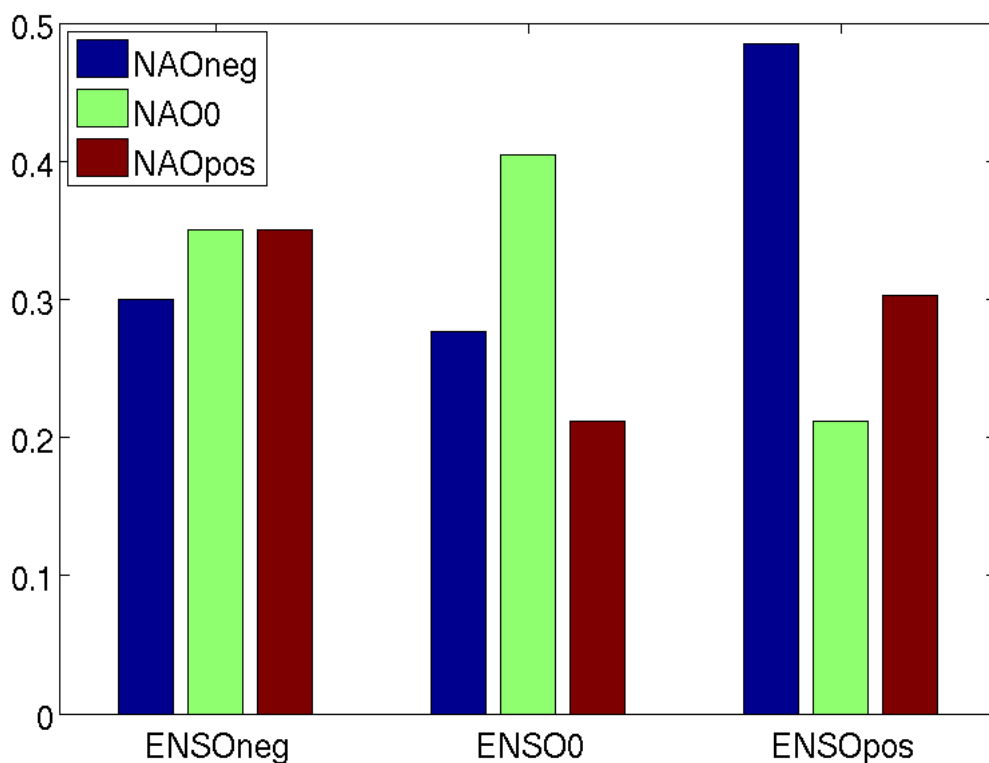
Figure 3.1 Probability distribution of NAO phases during a particular ENSO phase in the period 1899-2018. ENSO0 (neutral), ENSOneg (La Niña) and ENSOpos (El Niño) events are defined by the values of JFM HadISST Niño 3.4 index (ENSO0: $-0.5\sigma \leq I \leq 0.5\sigma$, ENSOneg: $I < -0.5\sigma$, ENSOpos: $I > 0.5\sigma$). An analogous definition is made for NAO events based on the NAO index (JFM Hurrell PC-based NAO index).

To examine if a similar distribution of ENSO and NAO phases is maintained on shorter time scales, probability distributions for successive 30-year long periods with an overlap of 20 years for the period 1899-2018 are presented in Fig. 3.2. Here, the NAO neutral cases were discarded.
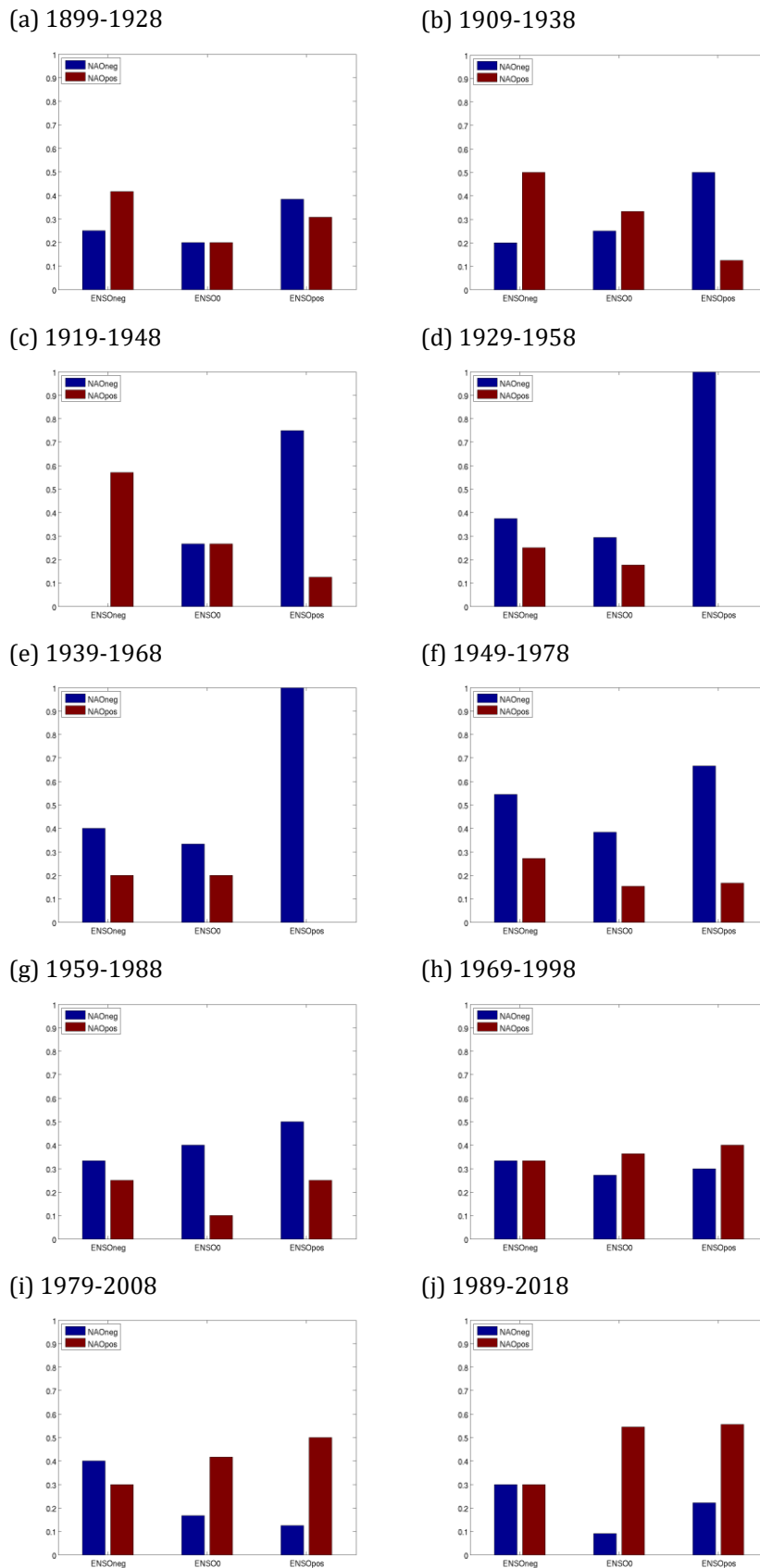
Figure 3.2 Probability distribution of NAO phases during a particular ENSO phase in the periods: (a) 1899-1928, (b) 1909-1938, (c) 1919-1948, (d) 1929-1958, (e) 1939-1968, (f) 1949-1978, (g) 1959-1988, (h) 1969-1998, (i) 1979-2008, and (j) 1989-2018. ENSO events are defined by the values of the JFM

HadISST Niño 3.4 index (ENSO0: -0.5σ ≤ I ≤ 0.5σ, ENSOneg: I < -0.5σ, ENSOpos: I > 0.5σ). An analogous definition is made for NAO events according to the NAO index (JFM Hurrell PC-based NAO index).

The distributions from Fig. 3.2 reveal temporal non-stationarity of the ENSO-NAO relationship. In the first seven periods, the positive ENSO phase is more frequently accompanied by the negative NAO. Particularly, the ENSOpos-NAO neg occurrences are predominant in the following sub-periods: 1909-1938, 1919-1948, 1929-1958, 1939-1968, and 1949-1978. However, in the sub-period 1969-1998, the situation has reversed, and there are more cases when ENSOpos is accompanied by the positive NAO phase (NAOpos). The difference is even more pronounced in the last two sub-periods (1979-2008 and 1989-2018). This finding indicates the non-stationary behaviour of the ENSO-NAO occurrence with a change in the relative distribution of the ENSO and NAO indices in the 1970s. The probability distribution of different ENSO and NAO phases in overlapping 30-year long sub-periods made for ERA-20C reanalysis data (Poli et al. 2016) confirms the previously described relationship (Appendix A1). When the decadal variability of the NAO index is removed by subtracting a 31-year moving average from the standardized NAO index, the available period is shortened due to filtering (Appendix A2). Nevertheless, the probability distribution also points to a similar observed change in the co-occurrence of ENSO and NAO phases.

In Fig. 3.2, ENSOneg (La Niña) events are more frequently accompanied by the positive NAO phase in the first three 30-year periods (Fig. 3.2 a-c). Starting from 1929 to 1958 (Fig. 3.2d), the ENSOneg-NAOneg combination became dominant in the following periods, except for 1969-1998 (Fig. 3.2f) and 1989-2018 (Fig. 3.2j), when there was an equal number of events in bot ENSOneg-NAOneg and ENSOneg-NAOpos categories.

The shift in the ENSO-NAO-occurrence is also supported by Fig. 3.3 showing a 31-year running correlation between the JFM HadISST Niño3.4 and JFM Hurrell PC-based NAO index. The 31-year-long correlation intervals are represented by the year in the centre of the interval, shown on the x-axis (e.g., the correlation interval 1899-1929 is shown as 1914). The correlation coefficients with a negative sign indicate that the El Niño phase is mainly accompanied by negative NAO. The 31-year running correlation displays the temporal variability of the correlation between the two indices. The correlation is not statistically significant at the beginning of the considered period. For the 31-year-long periods starting around 1910, the correlation becomes statistically significant. The correlation, however, drops to non-significant values again for 31-year periods starting around 1940.
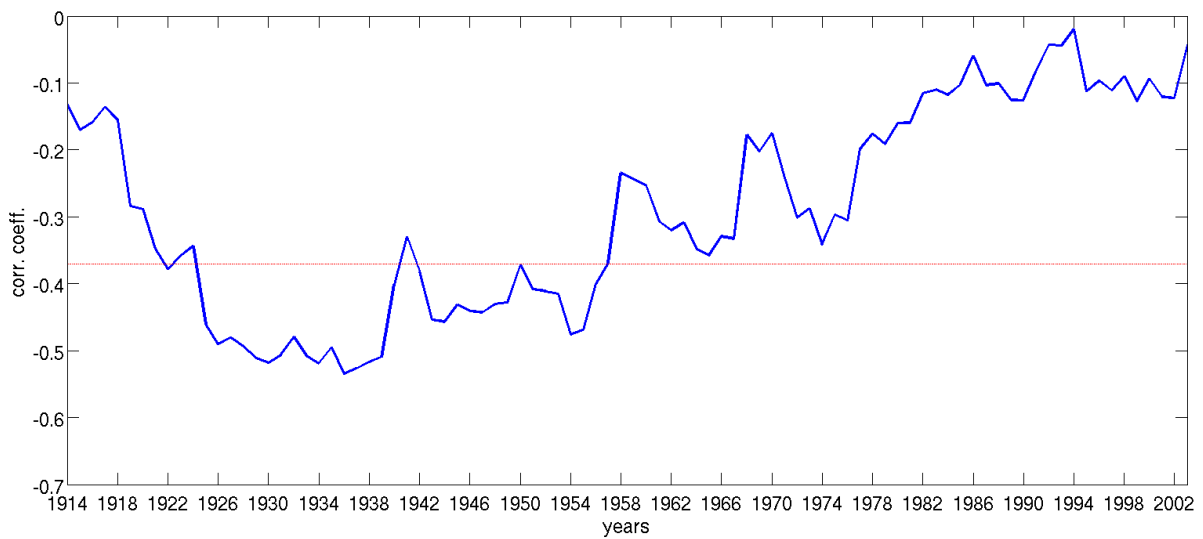
Figure 3.3 31-year running correlation between the observed HadISST JFM Niño 3.4 and JFM Hurrell PC-based NAO index for 1899-2018. The x-axis shows the centres of 31-year-long correlation intervals. The red line indicates statistically significant values at the 95% confidence level according to the two-tailed Student's t-test.

3.1.2. Non-stationarity in the ENSO teleconnection to the NAE region

Motivated by the non-stationarity of the ENSO-NAO connection illustrated in Figures 3.1-3.3, the teleconnection was investigated spatially with regression maps. Based on the results shown in Figures 3.2 and 3.3 we chose the 1929-1958 period as an example of the earlier conditions in the ENSO-NAE teleconnection, and the 1979-2008 period as an example of the ENSO-NAE teleconnection after the observed change. The regressions for the two periods (and their difference) are presented in Figures 3.4-3.7 for sea level pressure, zonal wind and geopotential heights at 200 hPa level.

Regression of the HadSLP onto the Niño3.4 index for the whole considered period (Fig. 3.4) indicates the existence of a weak ENSO-related signal over the western part of the North Atlantic. However, regression made for the two shorter (30-year) periods shows that the response resembles the negative NAO pattern for the 1929-1958 period (Fig. 3.4a). The area with negative regression coefficients extends from the eastern coast of North America across the Atlantic towards Europe and is accompanied by an area with positive regression coefficients to the north. On the other hand, the regression shows a significant change in the more recent period (1979-2008, Fig. 3.4b). The area with negative regression coefficients is weak and reduced to the middle of the Atlantic, while the other parts of the North Atlantic and Europe no longer show any statistically significant response. The change is evident when looking at the

difference between the two regression maps (Fig. 3.4d). The difference between the later and the earlier considered 30-year period is large and statistically significant over the northeastern part of North America, in the North Atlantic, and to the northwest of the Scandinavian Peninsula.
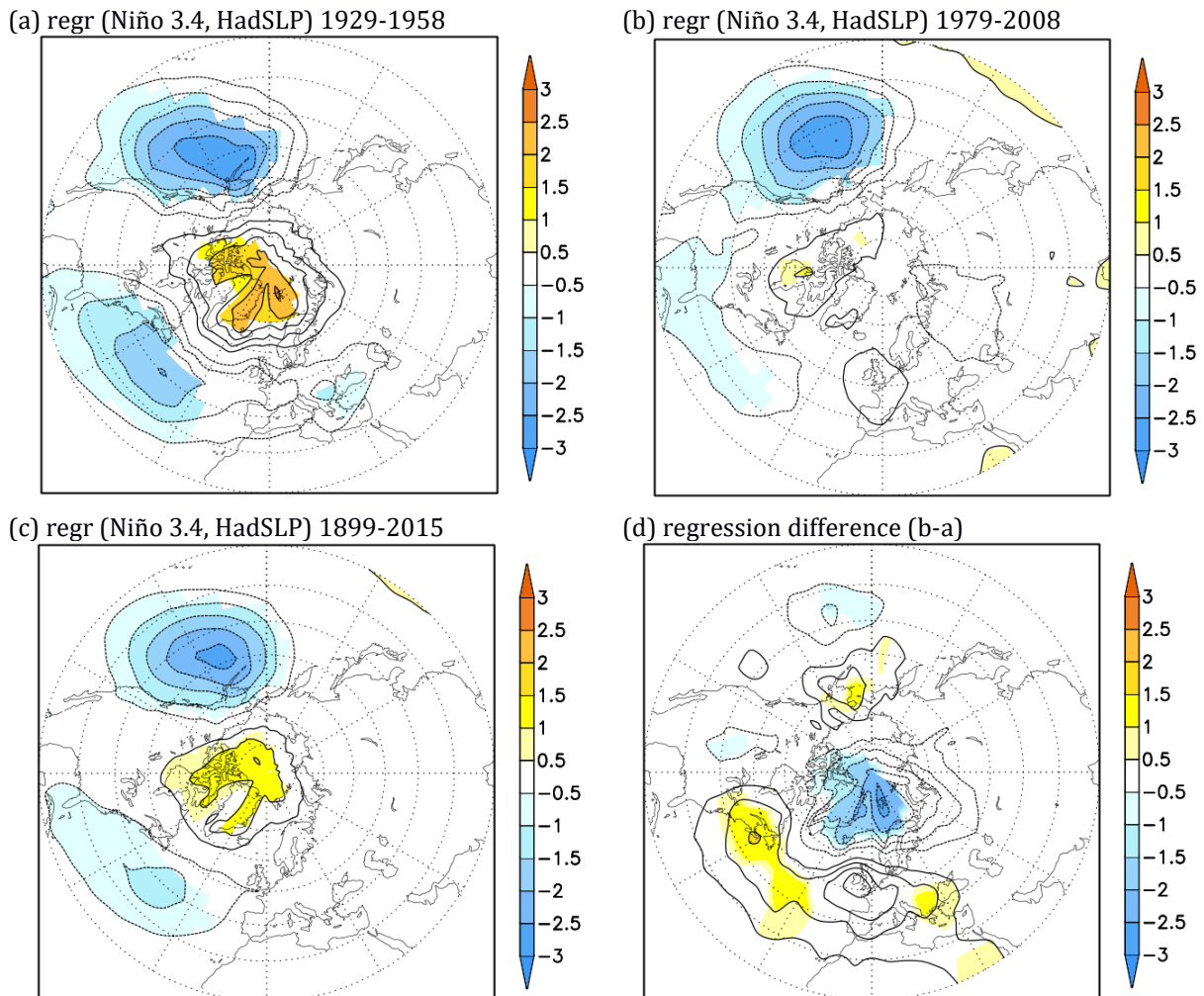
Figure 3.4 Regression of JFM HadSLP onto JFM Niño 3.4 index (HadISST) [hPa/ °C] for (a) 1929-1958, (b) 1979-2008, (c) 1899-2015, and (d) regression map in Fig. 3.4 (b) minus regression map in Fig. 3.4 (a). Statistically significant results (p < 10%) are shaded.

Another dataset, 20CRV3, indicated the same features of the ENSO teleconnection over the NAE region: weakening of the atmospheric response over the Atlantic and Arctic in the recent period (Fig. 3.5b). Again, the 20CRV3 dataset reveals a negative NAO-like response to ENSO in the earlier period (Fig. 3.5a). Similarly, as was obtained for HadSLP data (Fig. 3.4c), when the whole period is considered, the regression is relatively weak over the NAE region (Fig. 3.5c). Figure 3.5d shows the difference between the regressions for the more recent and earlier period indicating remarkable changes in the response over the Atlantic and Arctic. The difference is especially pronounced northwest of the Scandinavian Peninsula and in the North Atlantic, west of the European continent.
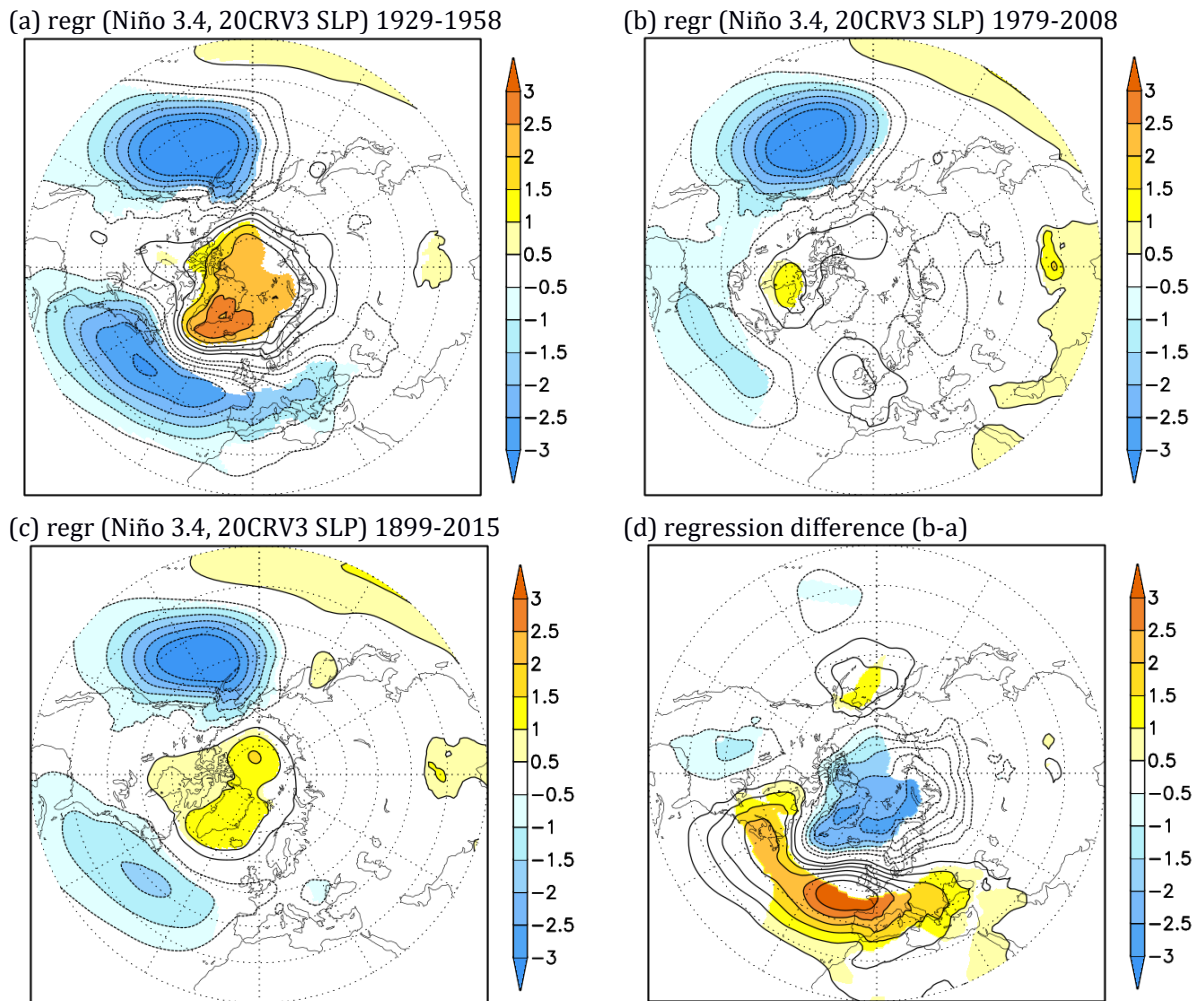
Figure 3.5 Same as Fig. 3.4 except for JFM NOAA-CIRES-DOE 20th Century Reanalysis V3 sea level pressure (SLP).

To analyse the changes over time in more detail, the whole considered period was divided into overlapping 30-year periods (Appendix A3), the same as the probability distributions presented in Fig. 3.2. Some of the earlier periods are associated with a strong and statistically significant negative NAO-like response (i.e., 1909-1938 in Appendix A3c, 1919-1948 in Appendix A3d, 1929-1958 in Appendix A3e, and 1939-1968 in Appendix A3f). During these periods, negative regression coefficients are found over Europe's southern and eastern parts, accompanied by positive coefficients over the Arctic region. However, the response started to weaken in 1949-1978 (Appendix A3g). It changes considerably in the later period (Appendix A3i) when the regression is non-significant over most of Europe. The weakening of the signal continues resulting in a non-significant response in the last period (Appendix A3j). As indicated by the Niño3.4 and NAO index connection (Figs. 3.1-3.3), these results imply there was a change in the ENSO-NAE teleconnection in the strength and spatial pattern of the atmospheric response.

Upper-level fields confirm the temporal variability in the ENSO-NAE teleconnection found for sea level pressure (Figs. 3.4 and 3.5). The geopotential height-regressions (GH200, GH500 and GH850) onto the Niño3.4 index (Appendix A4) show a barotropic response. The regression maps for periods before and after the turning point indicated considerably different patterns. Potential cause of the weakened ENSO-NAE teleconnection.

Focusing on the 200-hPa level (Fig. 3.6), the ENSO impact on the NAE region in the earlier period (Fig. 3.6a) is associated with positive regression coefficients over northern Canada, which is accompanied by a zonally oriented belt of negative regression coefficients extending from eastern North America across the Atlantic towards the European continent. In the later period (Fig. 3.6b), negative regression coefficients are weaker and do not reach the NAE region, unlike during the earlier period. The difference between the later and earlier periods (Fig. 3.6d) shows significant values over northern Canada and an area connecting North America's eastern coast to Europe.

(a) regr (Niño 3.4, 20CRV3 GH200) 1929-1958

(b) regr (Niño 3.4, 20CRV3 GH200) 1979-2008

(c) regr (Niño 3.4, 20CRV3 GH200) 1899-2015

(d) regression difference (b-a)
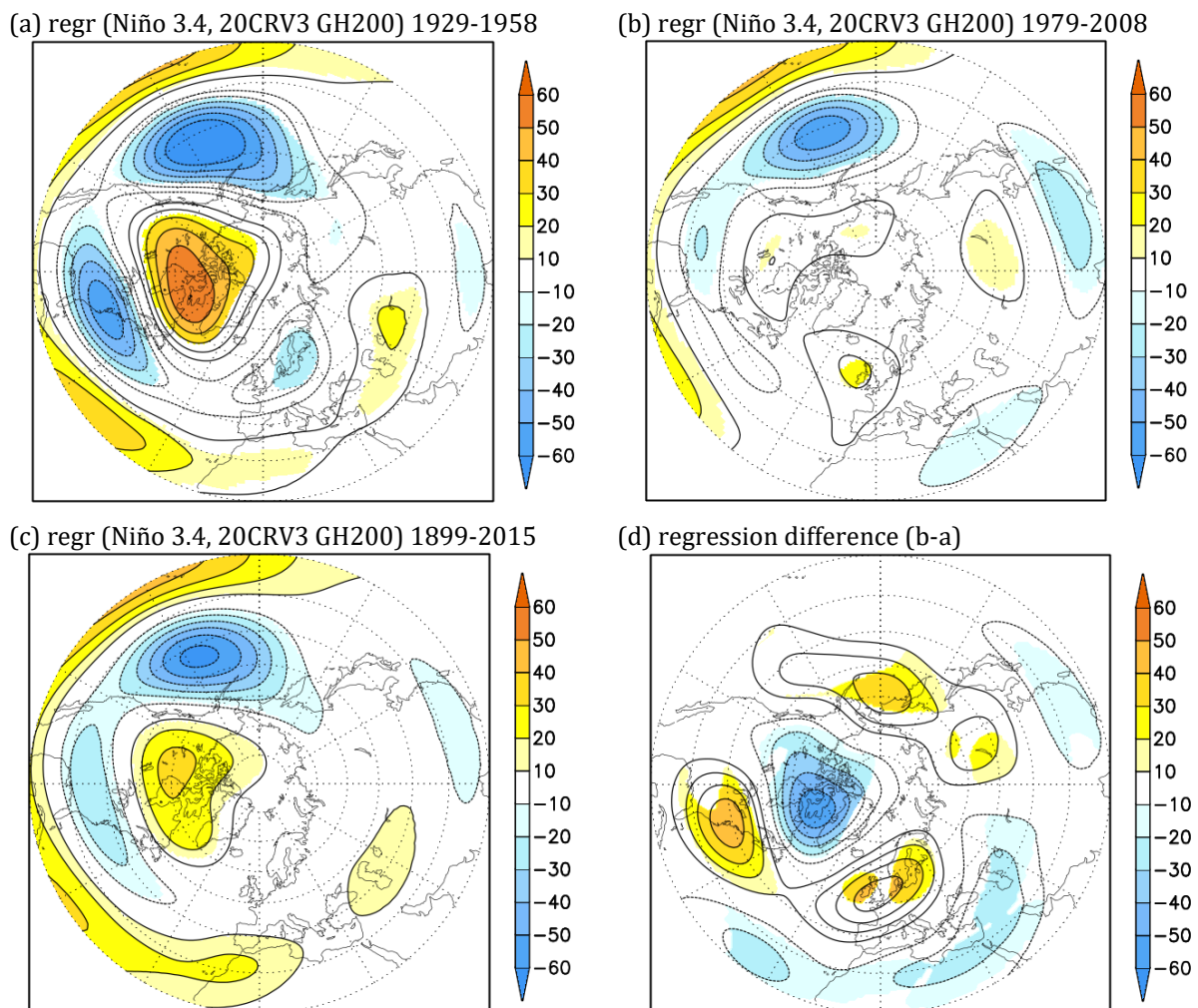
Figure 3.6 Same as Fig. 3.4 except for JFM NOAA-CIRES DOE 20th Century Reanalysis V3 geopotential heights at 200 hPa (GH200) [m/ °C].

The regression of zonal wind at 200 hPa onto the Niño3.4 index is modulated (Fig. 3.7), consistent with the geopotential height results. Zonal wind response to ENSO in the earlier period (Fig. 3.7a) contains positive regression coefficients on the southern part of the North Atlantic, linking North America and Europe, which are accompanied by negative regression coefficients in the northern, poleward side of the Atlantic (cf. Fig. 3.10c). However, the response shows the altered amplitude and spatial characteristics during the later period (Fig. 3.7b). In this later period, zonal wind response does not reach the Eastern Atlantic and is disconnected from the European continent. The significant change over the NAE region is also illustrated in the difference between the regression maps for the later and earlier period (Fig. 3.7d).

(a) regr (Niño 3.4, 20CRV3 u200) 1929-1958

(b) regr (Niño 3.4, 20CRV3 u200) 1979-2008

(c) regr (Niño 3.4, 20CRV3 u200) 1899-2015

(d) regression difference (b-a)
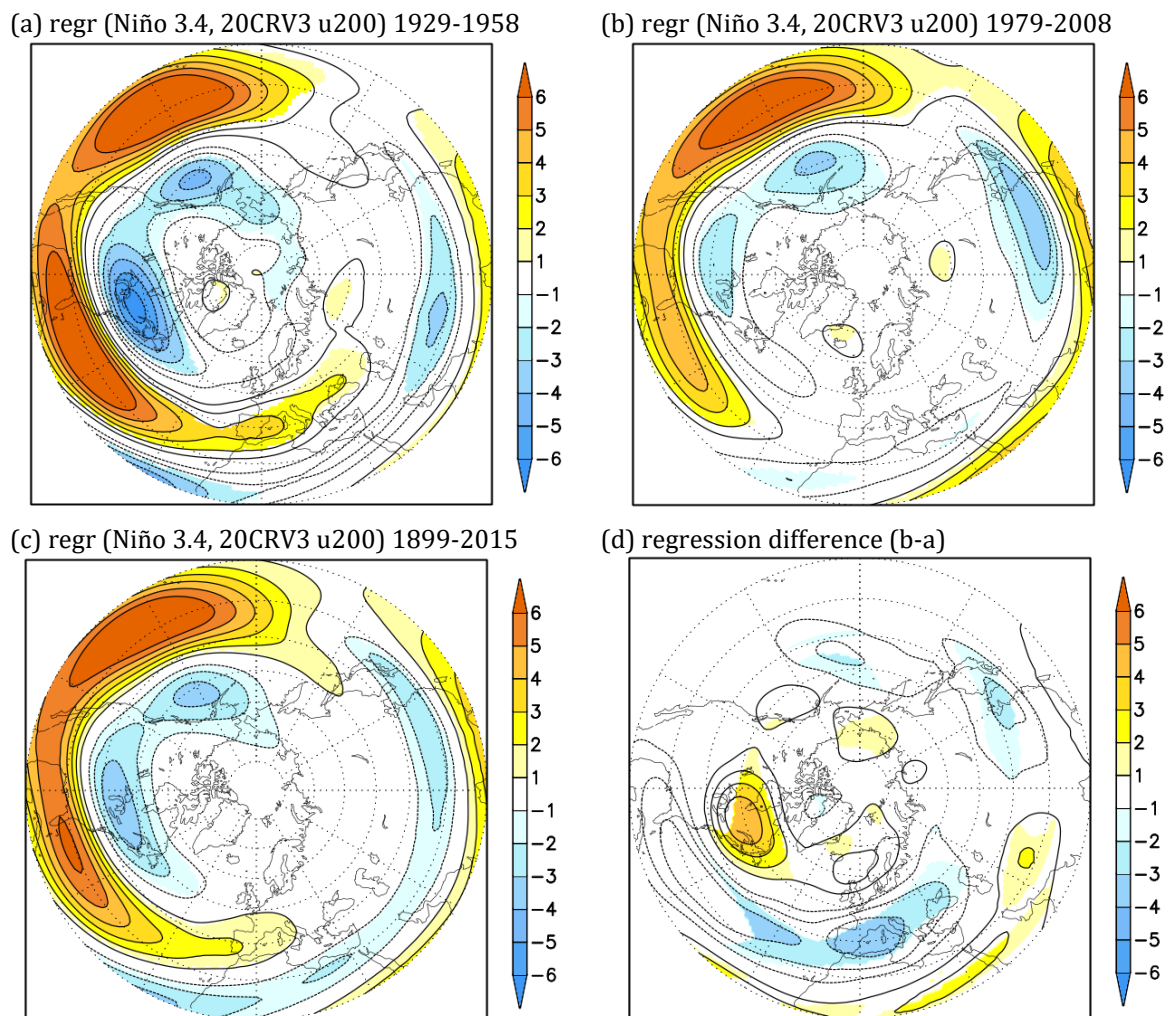
Figure 3.7 Same as Fig. 3.4 except for JFM NOAA-CIRES-DOE 20th Century Reanalysis V3 zonal wind at 200 hPa (u200) [m s^{-1} °C^{-1}]

Changes in both patterns and strengths of geopotential height, mean sea level pressure, and zonal wind regression maps indicate a shift in the ENSO impact on the NAE region in the 1970s. Before the 1970s, the atmospheric response to ENSO over the NAE region had the form of two zonally oriented belts with a stronger connection in terms of the values of the regression

coefficients (Fig. 3.7a). However, after the 1970s, the overall response over the NAE area weakened (Fig. 3.7b), and anomalies do not reach Europe (also compare Fig. 3.6 a with b). It is found that during the most recent period, the teleconnection pattern has changed, and the mean sea level pressure response faded to non-significant values (Fig. S1j). It is shown that the results of the regression depend on the considered period and its length.

By examining the regression maps, we are focusing only on the linear part of the ENSO-NAE teleconnection. However, the signal related to ENSOneg (La Niña) phase over the NAE region is found to be nonlinear (Zhang et al. 2015). To distinguish the nonlinear signal, a separate analysis of the two ENSO phases, in the form of ENSOpos (El Niño) and ENSOneg (La Niña) composites for HadSLP (Fig. 3.8) was made. The spatial distribution of the ENSO regression onto HadSLP (Fig. 3.4) and its change from earlier (Fig. 3.4a) to the later 30-year period (Fig. 3.4b) are consistent with ENSOpos composites (Fig. 3.8 a, c). The ENSOpos composite in the later 30-year period (Fig. 3.8c) changes the sign of the spatial pattern over the NAE area, which agrees with the results shown in Fig. 3.2. Meanwhile, the HadSLP composites for ENSOneg events for the same two 30-year periods (Fig. 3.8 b, d) have an overall weaker response over the NAE area and the spatial pattern is of the opposite sign. Despite the relatively small size of the presented composites, they imply that the observed change in the ENSO-NAE teleconnection is mainly due to the weakened ENSOpos-NAE connection. Also, results of the composite analysis revealed that the teleconnections associated with both ENSO phases become weaker over the NAE region in the later 30-year period (Fig. 3.8 c, d).
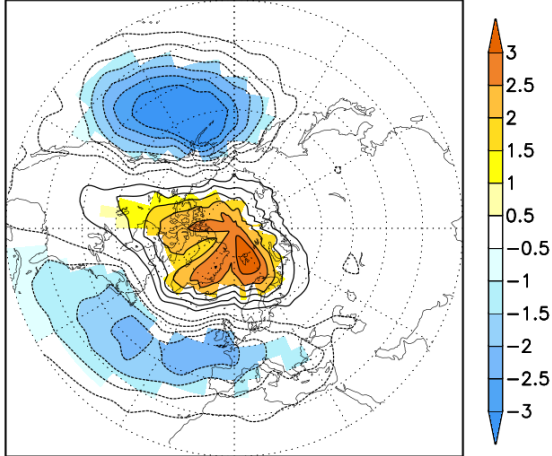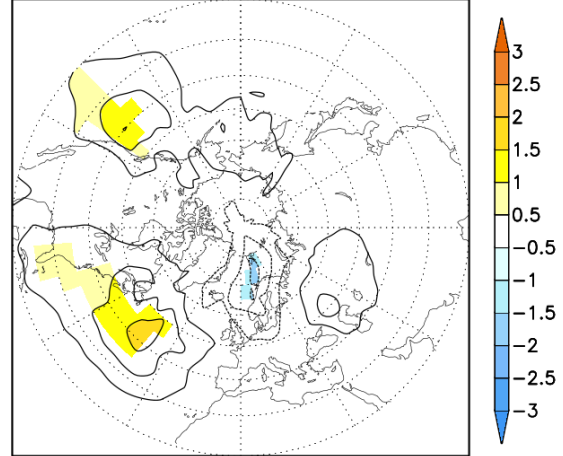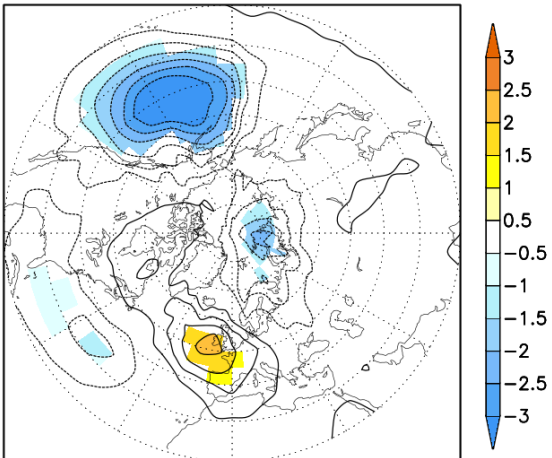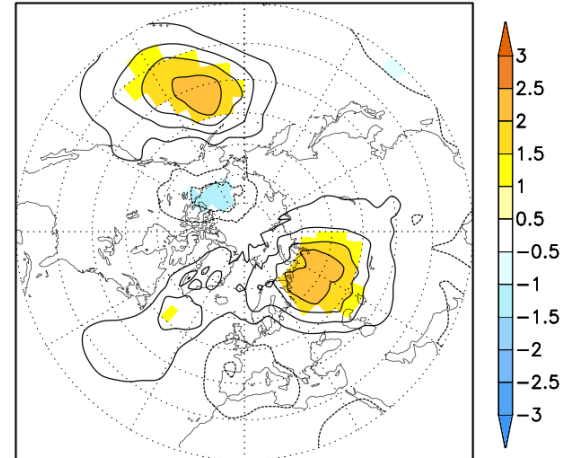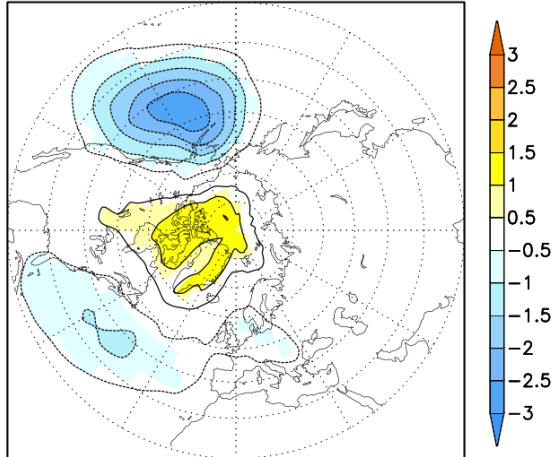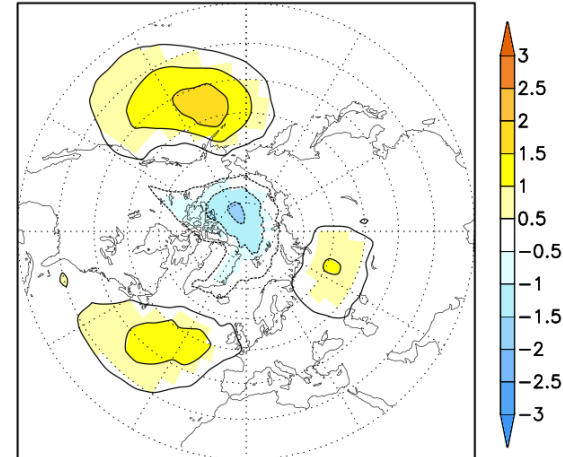
Figure 3.8 Composites of JFM HadSLP [hPa] for ENSOpos (El Niño) and ENSOneg (La Niña) events for (a)-(b) 1929-1958, (c)-(d) 1979-2008, and (e)-(f) 1899-2015. ENSOpos events are defined as JFM HadISST Niño 3.4 index > 0.5 σ, while ENSOneg are defined as JFM HadISST Niño 3.4 index < -0.5 σ. The number (n) of ENSOpos and ENSOneg events in each period is written in the parenthesis. Statistically significant results (p < 10%) are shaded.

3.2. Potential cause of the weakened ENSO-NAE teleconnection

Inspection of the regression maps from early to late 30-year periods indicates a temporal modulation of the ENSO-NAE teleconnection. Therefore, results for other variables suggesting the cause of the nonstationarity are offered. First, temperature anomalies (based on the climatology for the 1899–2015 period) at 200 hPa for two 30-year periods (Fig. 3.9) are presented. Comparing T200 anomalies in the earlier (Fig. 3.9a), later period (Fig. 3.9b), and their difference (Fig. 3.9c), the warming of the subpolar northern Canada atmosphere is evident. In the earlier period, temperature anomalies over the polar region are weakly negative. However, in the later period, anomalies over the polar region strengthen and change their sign.

(a) 20CRV3 T200 JFM anom 1929-1958

(b) 20CRV3 T200 JFM anom 1979-2008

(c) difference of anomalies (b-a)
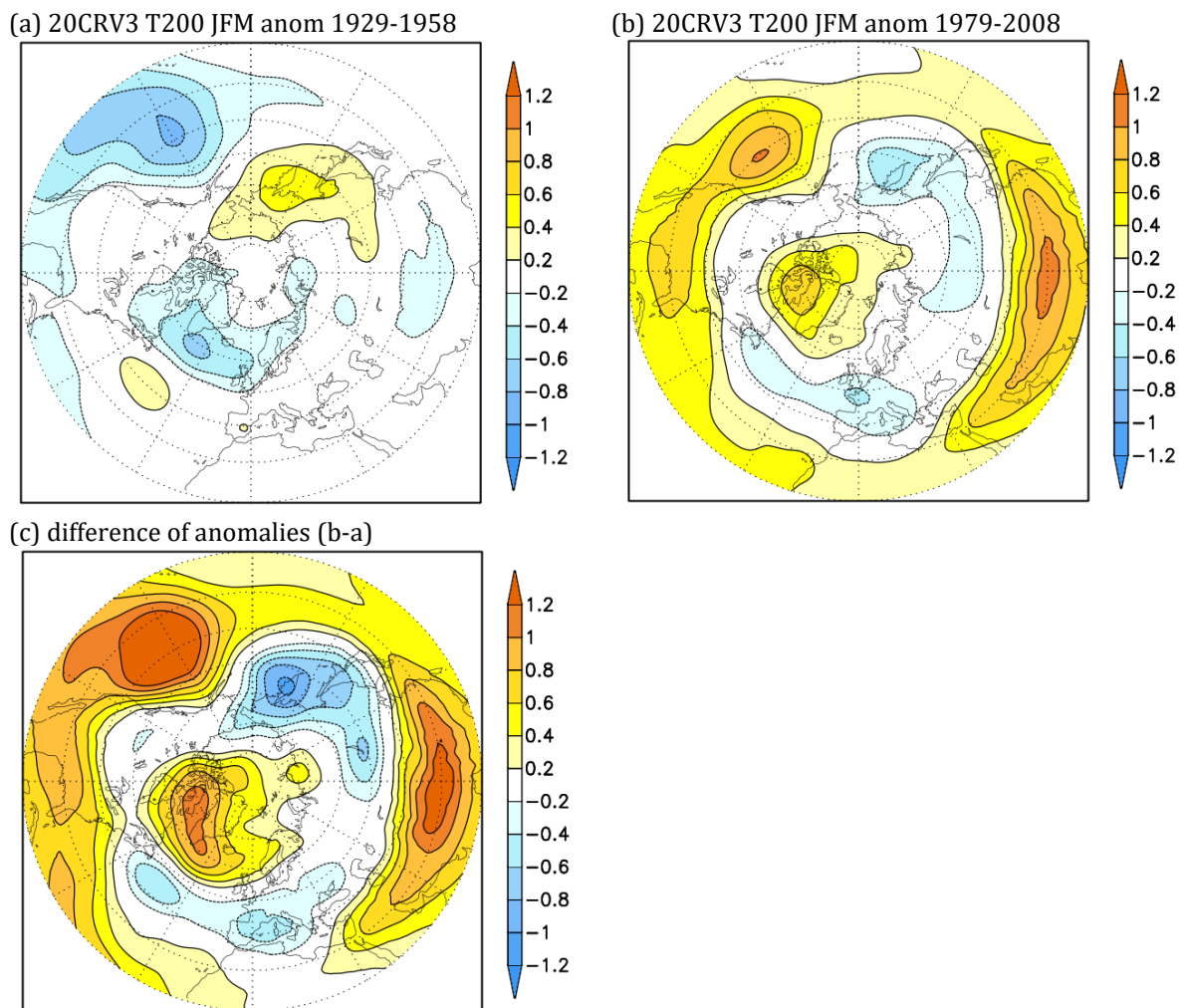
Figure 3.9 NOAA-CIRES-DOE 20th Century Reanalysis V3 averaged JFM temperature anomalies (using 1899-2015 climatology) at 200 hPa (T200) [°C] for (a) 1929-1958, (b) 1979-2008, and (c) anomalies in Fig. 3.9 (b) minus anomalies in Fig. 3.9 (a).

The warming of the polar atmosphere modifies the meridional temperature gradient, which may induce changes in the jet stream's speed and structure (e.g., waviness) (Cohen et al. 2014; Francis and Vavrus 2015; Cattiaux et al. 2016). Because the jet stream has a vital role in

teleconnections acting as waveguides (Branstator 2002), zonal wind change is also presented. Figure 3.10 shows zonal wind anomalies at 200 hPa for two periods as above: earlier (1929–1958; Fig. 3.10 a) and later (1979–2008; Fig. 3.10 b). The difference between the later and earlier period, compared to the u200 climatology (Fig. 3.10 c), reveals that in the later period, the southern flank of the Atlantic jet has strengthened, indicating its equatorward shift. Therefore, the change in the strength and position of the jet coincides with the weakening of the ENSO-NAE teleconnection.

(a) 20CRV3 u200 JFM anom 1929-1958

(b) 20CRV3 u200 JFM anom 1979-2008

(c) difference of anomalies (b-a)
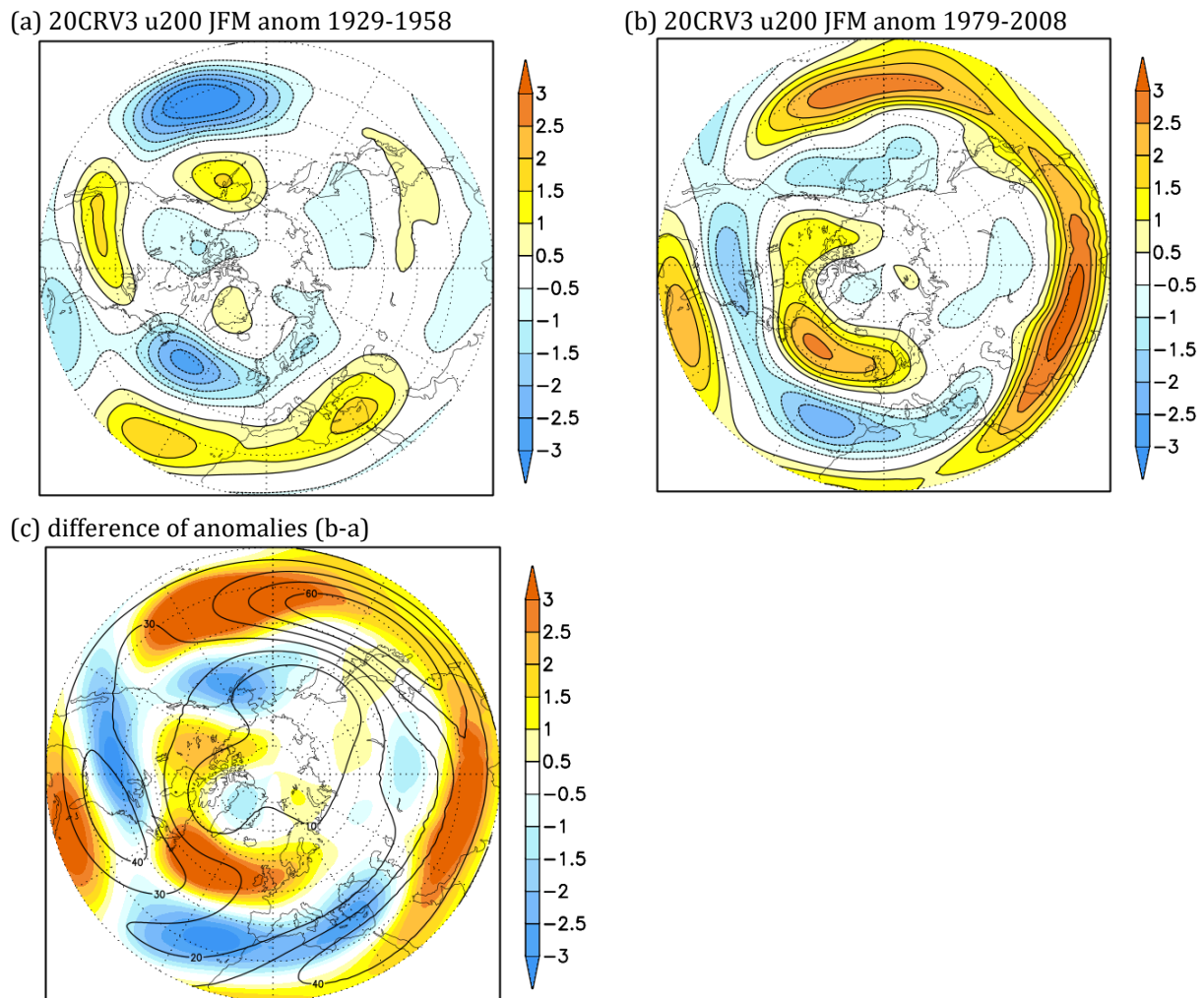
Figure 3.10 NOAA-CIRES-DOE 20th Century Reanalysis V3 averaged JFM zonal wind anomalies (using 1899-2015 climatology) at 200 hPa (u200) [m/s] for (a) 1929-1958, (b) 1979-2008, and (c) anomalies shown in Fig. 11 (b) minus anomalies in Fig. 11 (a) [m/s] (shaded) with overlaid contours of JFM zonal wind (u200) climatology for period 1899-2015 (contour interval = 10 m/s).

Variability of the midlatitude atmospheric circulation has been widely investigated, and many studies proposed Arctic warming and sea-ice loss as important contributors (Gastineau and Frankignoul 2015; Screen et al. 2018; Warner et al. 2019). Furthermore, century-scale sea-ice extent analysis has shown that the sea-ice extent changed considerably in the Northern Hemisphere and accelerated over the past several decades (Walsh and Chapman 2001). The

NOAA-CIRES-DOE 20CR V3 surface ice concentration anomalies averaged over the Arctic polar cap (−180° to 180° E, 70°–90° N) for the period 1899–2015 (Fig. 3.11) show that the significant drop in the ice concentration coincides with the changes in the ENSO-NAO teleconnection over the NAE area. Moreover, both tropical and extratropical SSTs affect the atmosphere through remote forcing and local ocean-atmosphere interaction (Gastineau and Frankignoul 2015; Czaja et al. 2019). In the next section, we pose the following question using model experiments: what are the roles of Arctic sea-ice loss and change in SSTs in controlling the ENSO-NAE teleconnection?
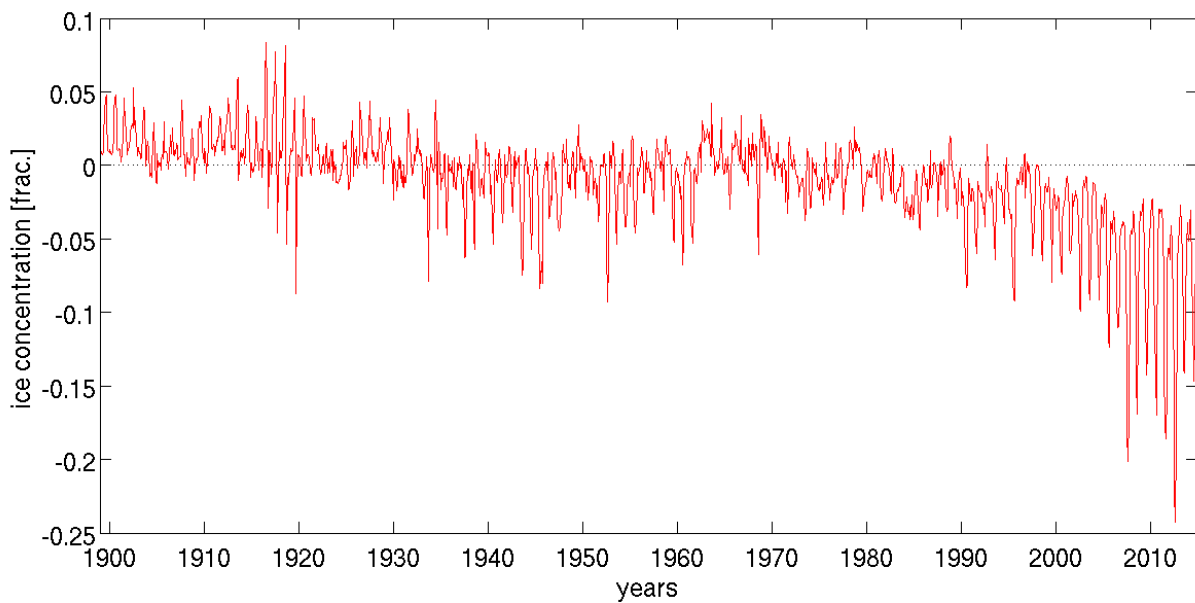
Figure 3.11 NOAA-CIRES-DOE 20th Century Reanalysis V3 surface ice concentration anomalies [frac.] averaged over the Arctic polar cap (-180°-180° E, 70°-90° N) for the period 1899-2015.

3.3. Modelling evidence

Previously in this chapter, observational evidence of the weakening of the ENSO-NAE teleconnection was presented. In this sub-section, the model results of investigating the modulation of the ENSO-NAE teleconnections through background states controlled by SST climatology and sea-ice concentration are reported.

3.3.1. Experimental design

ICTP AGCM experiments consisting of 210-year-long simulations (the first ten years are discarded) were designed to test the role of SST and SIC in the modulation of the ENSO-NAE

teleconnection. The model was forced with monthly-varying anomalous El Niño SSTs that are repeating annually (Fig. 3.12b). The same anomalous ENSO SSTs are superimposed on different SST and sea-ice climatologies in the different experiments. Investigation of the modulation of the ENSO teleconnections by the background states due to changes in SST and sea-ice concentration (SIC) climatologies is based on different combinations of 'early' or 'late' SST and 'high' or 'low' SIC climatologies. Here, the 'early'/'high' climatologies are calculated from the 1979-1999 period, and the 'late'/'low' climatologies from the 2005-2015 period. The difference between 'early' and 'late' SST climatologies used in the model experiments is shown in Fig. 3.12a.

(a) 'Early' – 'late' SST, Jan/Feb, CI=0.25K

(b) El Nino SST, Jan/Feb, CI=0.25K
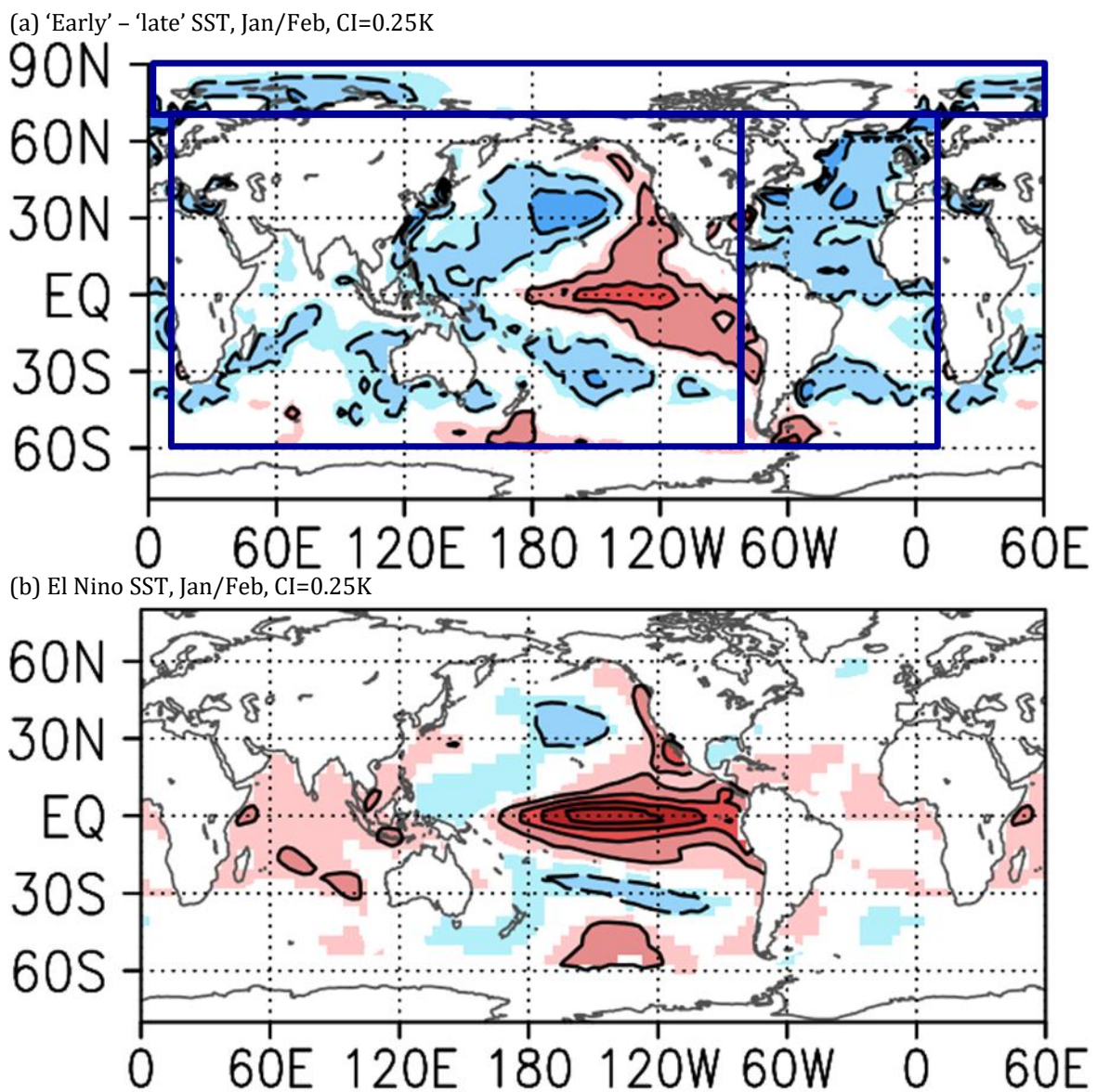
Figure 3.12 (a) 'Early' (1979-1999) minus 'late' (2005-2015) SST climatologies used in the model experiments. (b) El Niño SST anomaly applied. The climatology and anomalous SST applied in the model experiments vary monthly, but only Jan/Feb are shown here. The original data is from HadISST.

The atmospheric response, in terms of anomalies of certain variables, due to ENSO is calculated by subtracting a control run (forced globally prescribed climatological SST and SIC with no

ENSO) from another experiment with ENSO SST anomaly superimposed on the same SST and SIC climatologies. To isolate the modulating impact of the SST climatology in different ocean basins, we have also performed further 'low' sea-ice experiments with different combinations of 'early' and 'late' SST climatologies prescribed in three different ocean regions (the Arctic, Indian and Pacific, and Atlantic Oceans).

3.3.2. *Role of the SST climatology and sea-ice concentration in the modulation of the ENSO-NAE teleconnection*

Figure 3.13 shows the mean sea-level response to El Niño in simulations with differently prescribed climatological values of SIC and SST. The experiment forced with El Niño SST under 'high' SIC and 'early' SST climatologies (Fig. 3.13a) simulated a canonical response to ENSO with a negative NAO-like pattern over the NAE region. However, the experiment forced with 'low' sea-ice and 'late' climatological SST (representing more recent conditions) turned out considerably different (Fig. 3.13b). Not only is the spatial pattern of the response changed (the pattern does not project onto the NAO pattern), but the area of statistically significant values in the NAE sector has also shrunk. In particular, the anomaly over the Atlantic, which links the action centres over the Gulf of Mexico and Europe, is absent in the experiment with recent sea-ice and SST conditions.

What are the relative roles of sea-ice and SST changes in the weakening of the NAE teleconnection? The ENSO forcing on background conditions with 'low' sea ice but with a switch to 'early' SST climate produces a strengthened response (compare Fig. 3.13 b and d, and also Fig. 3.13 f and h). On the other hand, the weakening of the signal is obtained for the experiment retaining the 'late' SST climatology but with a switch to 'high' sea-ice concentration (Figs. 3.13 c and g). The switch suggests that the 'late' SST climatology is responsible for the weakened ENSO teleconnection in the NAE. The GH200 response to ENSO (Figs. 3.13 e-h) is consistent with the result for mean-sea level pressure, manifesting similar dependence on the SST and sea-ice climatology throughout the atmosphere.

These results highlight the role of the 'late' SST climatological state in weakening the atmospheric response to ENSO, while the 'low' sea-ice climatology could have the opposite effect. The biggest difference in SSTs is found in the Pacific and northern Atlantic (Fig. 3.12a).
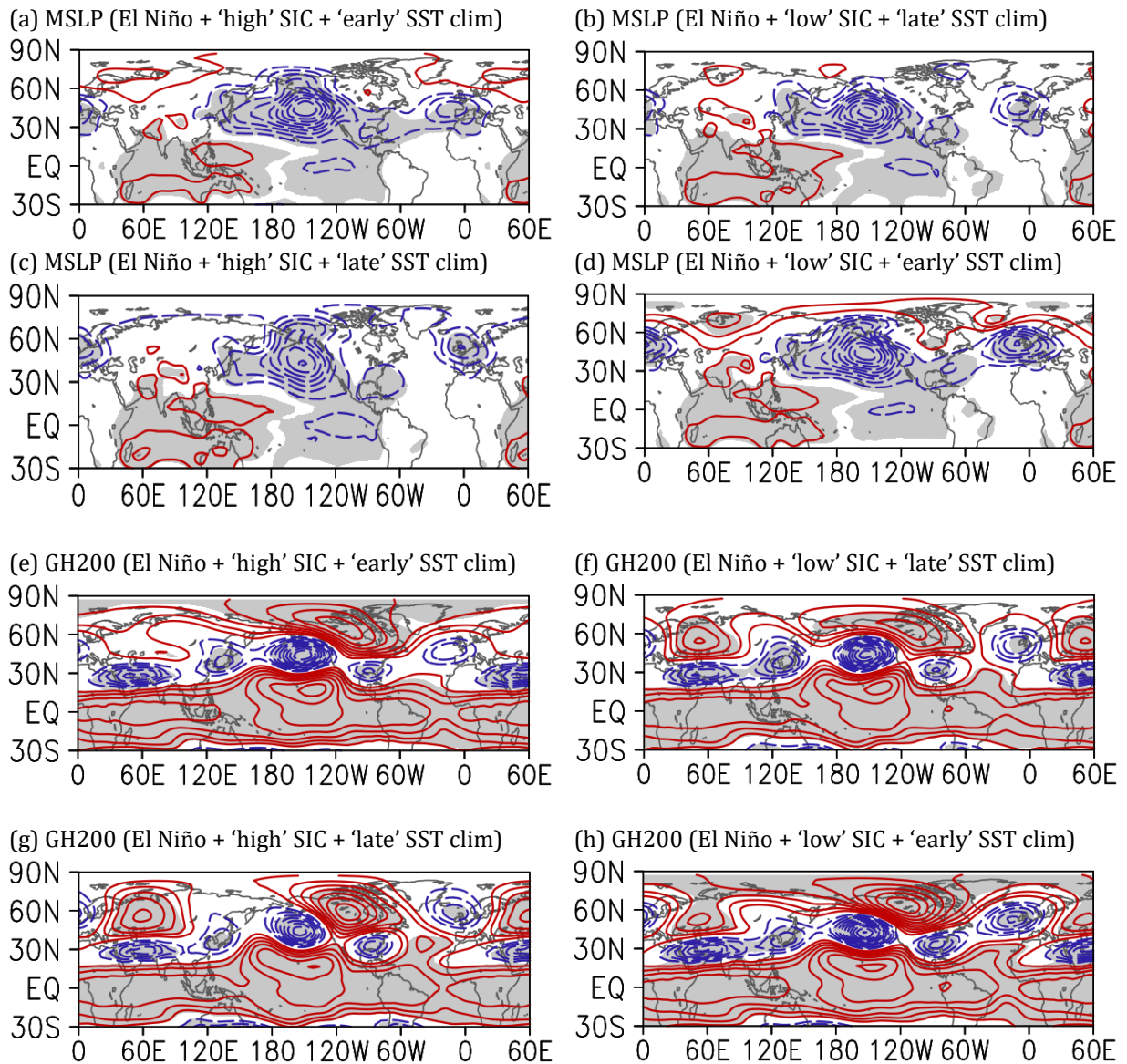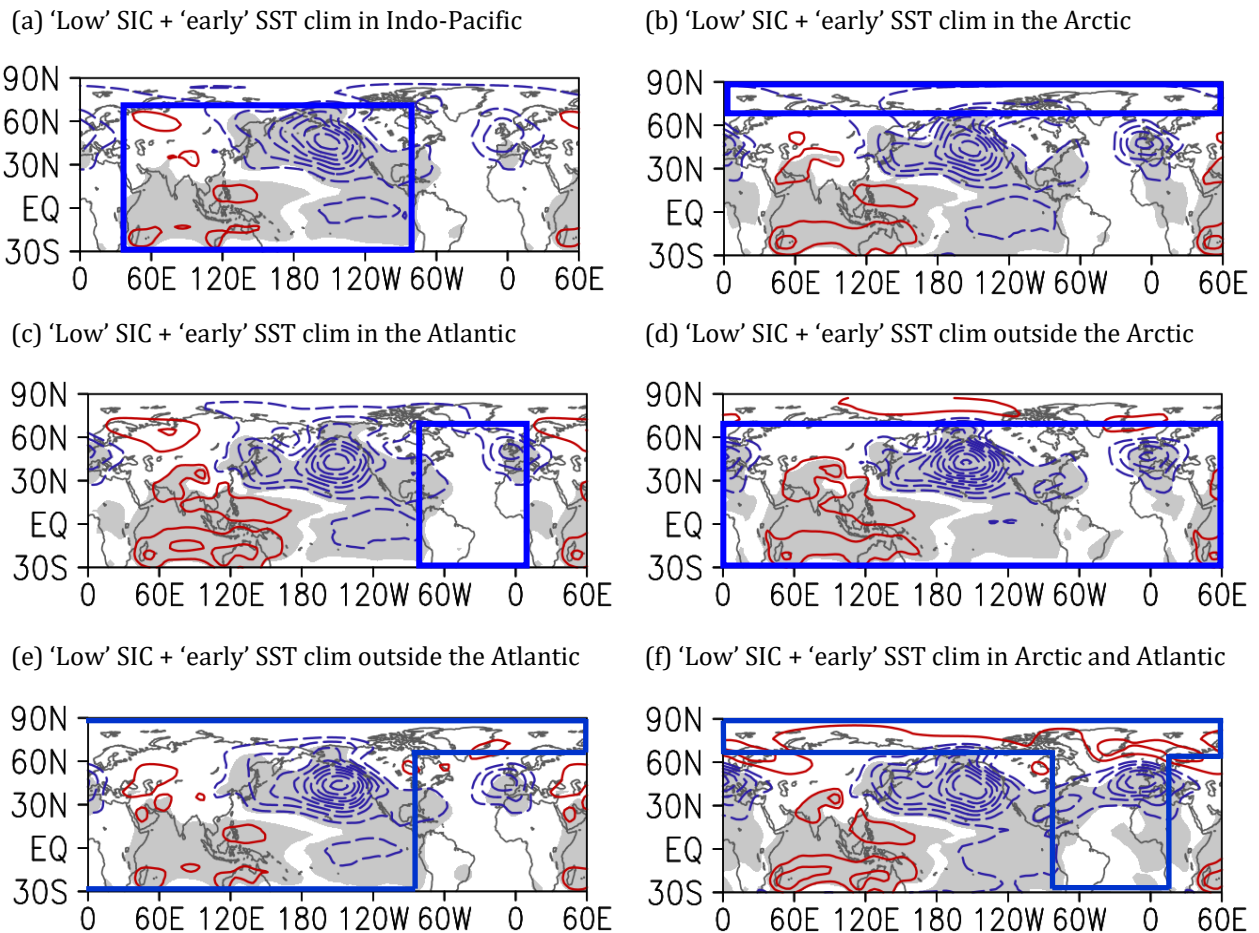
Figure 3.13 ICTP AGCM simulated MSLP response to El Niño in conditions with (a) 'high' sea-ice concentration and 'early' SST climatology, (b) 'low' sea-ice concentration and 'late' SST climatology, (c) 'high' sea-ice concentration and 'late' SST climatology and (d) 'low' sea-ice concentration and 'early' SST climatology. 'High' sea-ice concentration and 'early' SST climatology refer to the period 1979-1999, while the 'low' sea-ice concentration and 'late' SST climatology refer to the period 2005-2015. Panels (e)-(h): same as panels (a)-(g) but for the GH200 response. Contouring interval is 0.5 hPa in (a)-(d) and 5 m in (e)-(h). Red contours – positive values, blue contours – negative values. Statistically significant results (p < 5%) are shaded in grey.

3.3.3. Ocean areas responsible for the weakening of the ENSO-NAE teleconnection

To explore the impact of the SST climatology in more detail, intending to identify which parts of the global oceans are necessary for the weakening, we repeated the 'low' sea-ice experiments with 'early' and 'late' SST climatologies prescribed in the different oceans. Three separate ocean basins are delineated for this purpose – the Indian and Pacific Oceans, the Arctic Ocean, and the

Atlantic Ocean, as shown by the boxes with blue borders in Fig. 3.12a. Also, shown in Fig. 3.12b is the anomalous SST applied in all El Niño experiments. Since there are two climatological SSTs to choose from for each of the three ocean basins, eight unique combinations of 'early' or 'late' SST climatologies prescribed in these regions exist. All these eight experiments have been carried out. Results from two of them (all basins at 'early' or 'late' SST) are already shown in Fig. 3.13. Figure 3.14 shows results from the other six, with the blue borders indicating the areas where the SST climatology is from the 'early' period and the area outside of that is from the 'late' period. Atmospheric responses to El Niño under these conditions are then compared with the response to the 'low' sea-ice conditions with globally prescribed 'late' SST climatology (Fig. 3.13b). The idea is to see which one(s) of these experiments revert from a weakened to a strengthened ENSO response similar to the 'low' sea-ice and 'early' SST everywhere, shown in Fig. 3.13d. This approach allows examination of the sensitivity of the modelled atmospheric response to the background SST states.

With the experiment presented in Fig. 3.13b as a starting point, we consider the impact of reverting the SST climatology in the Indo-Pacific region to the 'early' SST climatology, while the 'late' SST climatology is kept elsewhere (Fig. 3.14a). The pattern is similar to that in Fig. 3.13b (i.e., anomalies form a monopole over the Eastern Atlantic detached from the anomalies covering Central America). In comparison with Fig. 3.13a, the NAE response in Fig. 3.14a is much weaker, with statistically significant anomalies covering a very small area. The response is somewhat stronger when 'early' SST climatology is prescribed over the Arctic Ocean (Fig. 3.14b), but it still retains the monopole form. Similar weak teleconnections in the NAE area are obtained for the experiment with 'early' SST climatology prescribed in the Atlantic (Fig. 3.14c). The results of Fig. 3.14a-c suggest that the change of SST climatology in these three ocean areas independently is not enough to modify the result of Fig. 3.13b substantially. The response still does not change significantly from Fig. 3.13b when we revert to 'early' SST climatology everywhere outside the Arctic Ocean (Fig. 3.14d) or outside the Atlantic Ocean (Fig. 3.14e). However, when 'early' SST climatology is prescribed in both the Arctic and Atlantic, the response changes simultaneously in strength and pattern (Fig. 3.14f). The response then consists of a non-significant positive northern centre and a significant negative southern centre across the Atlantic (connected with anomalies covering Central America) and is a reminiscence of the responses under 'early' SST conditions (Figs. 3.13a, d). Experiments in Fig. 3.14 reveal that if the SST climatology in the Arctic and Atlantic is reverted to 'early' SST values, the teleconnection in the NAE region stays similar to that for low sea-ice and globally prescribed 'early' SST climatology, i.e., it is strengthened like in Fig. 3.13d. Equivalently, it means that if 'late' SST climatology is prescribed in the Arctic or Atlantic, the response is weaker, with anomalies forming a similar pattern as the one in 'late' SST conditions (Fig. 3.13b, c). The total SST (i.e., El Niño anomaly + climatology) in

the later period is less than that of the early period because the climatology in the tropical Pacific has weakened (Fig. 3.12a) in the late period. However, in this instance, it turns out the change in SST climatology in the Pacific is not a factor.

(a) 'Low' SIC + 'early' SST clim in Indo-Pacific

(b) 'Low' SIC + 'early' SST clim in the Arctic

(c) 'Low' SIC + 'early' SST clim in the Atlantic

(d) 'Low' SIC + 'early' SST clim outside the Arctic

(e) 'Low' SIC + 'early' SST clim outside the Atlantic

(f) 'Low' SIC + 'early' SST clim in Arctic and Atlantic

Figure 3.14 ICTP AGCM simulated MSLP response to El Niño in conditions with 'low' sea-ice concentration and 'early' SST climatology prescribed in (a) Indian and Pacific Ocean, (b) Arctic Ocean, (c) Atlantic Ocean, (d) Atlantic, Indian and the Pacific Ocean, (e) Arctic, Indian and Pacific Ocean and (f) Arctic and Atlantic Ocean. Blue rectangles illustrate regions with prescribed 'early' SST climatology; the 'late' SST climatology is prescribed outside those regions. 'High' sea-ice concentration and 'early' SST climatology refer to the period 1979-1999, while the 'low' sea-ice concentration and 'late' SST climatology refer to the period 2005-2015. Statistically significant results (p < 5%) are shaded in grey. The contouring interval is 0.5 hPa. Red contours – positive values, blue contours – negative values.

3.3.4. Discussion

The recent weakening of the ENSO-NAE teleconnection is found in the observed data, reanalysis, and the targeted ICTP AGCM simulations coincide with a climate shift which happened in the late 1970s. The changes in the climate state are documented in the study by Jung et al. (2003). These include the change from low to high values of the NAO (Hurrell 1995), the change from low to high values of the PNA pattern (Trenberth and Hurrell 1994), an increase in the Northern

Hemisphere mean temperature (Hurrell 1996), an eastward shift of the centres of action of the interannual variability of the Azores low (Jung et al. 2003), changes in the link between the polar night jet and the tropospheric NAO (Kodera et al. 1999) and the changes in the characteristics of ENSO events (e.g., Wang and An 2001).

The ICTP AGCM results together indicate that the Atlantic and Arctic SST change in recent decades can weaken the ENSO teleconnection in the NAE area separately. The later warming of the North Atlantic is related to the Atlantic Multidecadal Oscillation, both in pattern and timing. We suggest that SST in the Atlantic affects the background winds which determine the Rossby wave propagation and interaction with the mean flow that is so important for ENSO teleconnection in the NAE (e.g., Hoskins and Karoly 1981; Hoskins and Ambrizzi 1993). A simple inspection of the model experiments performed here indicates a common feature: the weaker subtropical jet in the North Atlantic in the earlier period compared to the more recent one. Consistent with the modulation of the El Niño teleconnections presented above, this only occurs for experiments prescribed with Atlantic and Arctic SST changes (Appendix Fig. A5 shows three examples). This result in Appendix A5 agrees with Fig. 3.10, suggesting that the subtropical jet in the North Atlantic is stronger for periods with weaker teleconnections. Investigation of the changes in complex tropospheric and stratospheric pathways (Jiménez-Esteve and Domeisen 2018; King et al. 2018; Domeisen et al. 2019; Mezzina et al. 2020; Li et al. 2020), and how well models and reanalyses agree with each other, could be investigated in a future study.

For completeness, we have conducted additional experiments with El Niño SST anomalies placed in the central Pacific (El Niño Modoki SST pattern, Appendix Fig. A6). In terms of the effect on the strength of atmospheric teleconnections in the NAE area, the obtained results are similar to those for the canonical El Niño (Figs. 3.12 and 3.13.)

It is well-known that natural variability is an important source of uncertainty in the ENSO-NAE teleconnection. As highlighted in van Oldenborgh and Burgers (2005), the relatively short period of observations, weak ENSO signal and large atmospheric noise in the extratropics are all limiting factors for investigating the strength and long-term variations of ENSO teleconnections. The modulations of ENSO teleconnections can be small compared to the effects of the internal atmospheric variability, and it is often challenging to demonstrate high statistical significance (van Oldenborgh et al. 2000; Sterl et al. 2007). However, we believe that our conclusion here regarding the role of the Arctic and Atlantic oceans in weakening the ENSO teleconnection in NAE is robust (although it might still be model-dependent) due to the consistency of the results across a large number of sensitivity experiments performed.

4. Impact of tropical SSTs on the NAE climate variability in late winter

In the following chapter, various methods are applied to 200-hPa geopotential heights to extract modes of variability occurring in the ensemble of numerical simulations made with the ICTP AGCM. Different idealised experiments were conducted to detect the potential impact of tropical sea surface temperatures on the North Atlantic-European area.

Text and figures from this chapter were first published in *Climate Dynamics*: Ivasić S, Herceg-Bulić I (2022) A modelling study of the impact of tropical SSTs on the variability and predictable components of seasonal atmospheric circulation in the North Atlantic–European region. *Clim Dyn*. https://doi.org/10.1007/s00382-022-06357-3

4.1. ICTP AGCM simulations

Six experiments based on a 35-member ensemble of numerical simulations have been designed to detect the potential impact of tropical SSTs on the North Atlantic-European region (NAE; 20°-80° N, 90° W-60° E). All experiments cover the period between 1854 and 2010. The first year of the model integration is left out of the analysis. Each ensemble member within a single experiment has identical boundary forcing in the form of monthly SSTs taken from the NOAA ERSST V3 dataset (Smith et al. 2008). Members of the same experiment differ only in initial conditions set by the duration of random diabatic forcing during the first year of the model integration.

The ocean areas where SST anomalies are prescribed are unique to each experiment, while the rest of the ocean basins contain SSTs set to climatological values. Thus, the area of boundary forcing is limited to the part of the domain with prescribed SST anomalies. Lower boundary forcing in each is defined as follows: Ctrl (control) experiment has global SST anomalies (90° S-90° N, 0°-360° E); SST forcing in the Tropics experiment is prescribed in the entire tropical zone (30° S-30° N, 0°-360° E); TroAtl experiment has SST forcing constrained to the tropical Atlantic (30° S-30° N, 100° W-20° E); TroPac experiment is forced by SSTs prescribed in the tropical Pacific (30° S-30° N, 120° E-60° W); TroInd experiment has SST anomalies prescribed in the

tropical zone of the Indian Ocean (30° S-30° N, 30°-120° E), and Clim experiment contains only climatological SSTs in the whole domain (i.e., the climatological experiment has no SST forcing). As an illustration of the monthly varying SST boundary forcing set up for the ICTP AGCM experiments described above, SST anomalies in January 2000 are shown in Fig. 4.1. The climatological experiment is not shown in Fig. 4.1 since it does not contain any SST anomalies.

Empirical orthogonal functions (EOF) analysis and signal-to-noise optimal patterns method were conducted on seasonal geopotential height anomalies over the NAE region. The first 20 EOF modes were used as input for the signal-to-noise optimal patterns analysis.
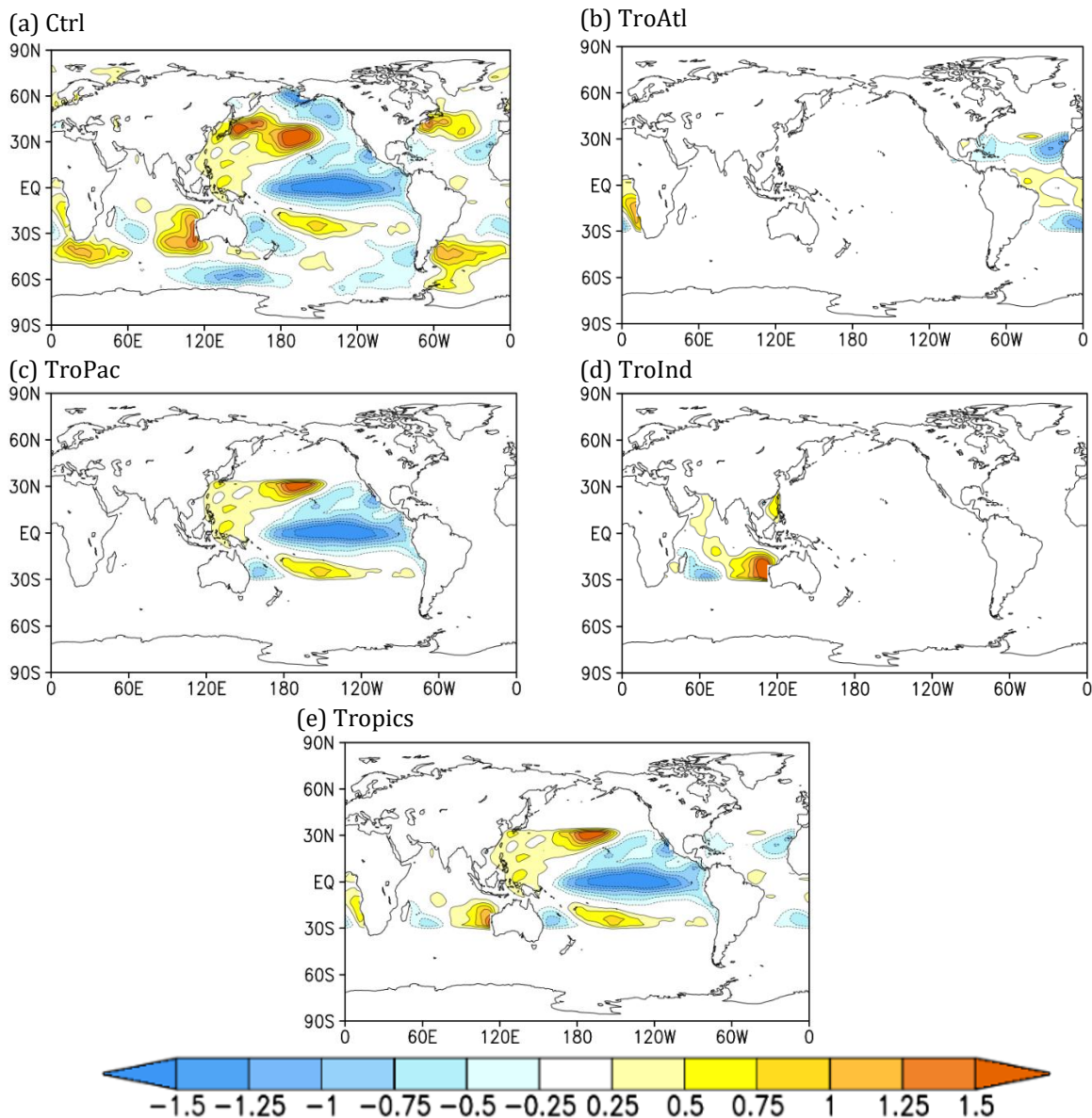
Figure 4.1 SST anomalies (SSTA) [K] in January 2000 as an illustration of the experimental setup of monthly-varying SST boundary forcing in the ICTP AGCM experiments: (a) Ctrl, (b) TroAtl, (c) TroPac, (d) TroInd, and (e) Tropics.

4.2. EOF analysis

The climate system consists of an externally forced component and a component arising from internal variability. There is no straightforward way of separating these two components, although using an ensemble of numerical simulations made by a climate model is one of the possible methods. Therefore, we employed the EOF analysis on the ensemble of numerical simulations in two ways – using the average of the ensemble simulations, i.e., the ensemble mean, and considering all individual simulations (35 simulations in each experiment). The ensemble-mean approach mainly reflects the forced component of the signal, while the method using all ensemble members includes the signal due to the internal variability of the climate system.

Figure 4.2 shows the EOF1 patterns of JFM geopotential heights at 200 hPa (GH200). The main feature of the leading EOF mode of GH200 based on all ensemble members (Fig. 4.2 left column) is a dipole between high and midlatitudes, reminiscent of the NAO, which is the dominant mode of internal variability of the NAE region. The first of the dipole centres is located between Greenland and North America (55°-80° N), while the second one is positioned in the zone connecting the east coast of North America and Western Europe (30°-50° N). The main spatial characteristics of the first EOF mode based on all ensemble members, namely the position of the dipole between high and midlatitudes, remain unchanged in the experiments with different areas of SST boundary forcing. The similarity of the EOF1 patterns in SST-forced experiments (Figs. 4.2 c, e, g, i, k) with the EOF1 pattern in the Clim experiment (Fig. 4.2a), which contains only climatological SSTs, indicates that the spatial distribution of the EOF1 mode based on all ensemble members is not considerably affected by the SST boundary forcing. The explained variance (ExpVar) is around 30% for each EOF calculated using all ensemble members.

The spatial pattern of the leading EOF mode of GH200 in the JFM season calculated for the ensemble mean of each experiment is also shown in Fig. 4.2 (right column). The spatial patterns of the ensemble mean EOFs differ from the patterns of the leading EOF mode calculated using all ensemble members (Fig. 4.2 left column) both in amplitude, spatial characteristics and percentage of explained variance. The first EOF patterns based on the ensemble mean have a smaller amplitude than their counterparts based on all ensemble members. The EOF1 patterns in the Clim and TroInd experiments (Fig. 4.2b and j) retain the dominantly dipolar shape. Still, these Clim and TroInd EOFs have a smaller percentage of explained variance than in the case of EOF1 mode taking all ensemble members into account. Besides the dominant dipole, the late-winter ensemble-mean EOF1 patterns in Ctrl, TroPac and Tropics experiments (Fig. 4.2d, h and l) have two additional centres over the south-eastern edge of the domain. Meanwhile, the first

EOF mode in the TroAtl experiment (Fig. 4.2f) has a centre over the North Atlantic (50° N, 90°-10° W) and a band connecting two centres - a weaker one over the Atlantic (20° N, 90° W-0° E) to the other over Europe (40°-75° N, 0°-60° E). The leading EOFs based on the ensemble mean of each experiment explain a smaller percentage of the variance of GH200 compared to the all-member EOFs, except for the TroPac and Tropics experiments (Fig. 4.2h and l). Results presented in Fig. 4.2 suggest that the imposed SST boundary forcing impacts the spatial distribution of GH200 variability represented by EOF1 patterns based on the ensemble mean (Fig. 4.2 right column).

Figure 4.3 shows the second EOF pattern of JFM GH200, which is orthogonal to the first EOF mode by definition. The EOF2 pattern for all ensemble members (Fig. 4.3 left column) has the shape of a dipole in all experiments, with the first centre located southeast of Greenland (55°-75° N), and the second above continental Europe (25°-70° N). The second centre has a "tail" of weaker amplitude extending from Western Europe, across the Atlantic to the east coast of North America. Similar to its first mode (Fig. 2 left column), the main spatial characteristics of the EOF2 pattern based on all ensemble members remain unchanged in different experiments, implying that the SST forcing does not impact the spatial characteristics of this second EOF mode. The explained variance is around 17% in all AGCM experiments (Fig. 4.3a, c, e, g, i, k). Also, the second all-members EOF mode projects onto the East Atlantic pattern (Barnston and Livezey 1987). The first and second EOF modes explain around 50% of the JFM GH200 variability over the NAE region.

The second EOF mode of JFM GH200 calculated for the ensemble mean of each experiment is shown in the right column of Fig. 4.3. The Clim, Ctrl, and TroPac ensemble-mean EOFs (Fig. 4.3b, d, h) resemble their counterparts calculated using all ensemble members (Fig. 4.3 left column). Meanwhile, the Tropics EOF2 (Fig. 4.3l) has a dipolar shape with the locations of its two most prominent centres (around 30° N and 50° N) coinciding with those in the Tropics EOF1 based on the ensemble mean (Fig. 4.2l). The ensemble-mean EOF2 patterns in the TroAtl and TroInd experiments (Fig. 4.3f and j) are similar to the EOF1 mode based on all members (Fig. 4.2 left column). The second EOF is responsible for 14-17% of the GH200 variability in late winter for both methods (cf. Fig. 4.3 left and right), except in the TroAtl and TroPac experiments, which have a higher percentage in the case of the ensemble-mean EOFs (around 19%).

(a) All Members EOF1 Clim (ExpVar 33.3%)
(b) Ensemble Mean EOF1 Clim (ExpVar 25.0%)
(c) All Members EOF1 Ctrl (ExpVar 33.3%)
(d) Ensemble Mean EOF1 Ctrl (ExpVar 27.4%)
(e) All Members EOF1 TroAtl (ExpVar 31.1%)
(f) Ensemble Mean EOF1 TroAtl (ExpVar 22.6%)
(g) All Members EOF1 TroPac (ExpVar 32.8%)
(h) Ensemble Mean EOF1 TroPac (ExpVar 32.3%)
(i) All Members EOF1 TroInd (ExpVar 29.4%)
(j) Ensemble Mean EOF1 TroInd (ExpVar 26.6%)
(k) All members EOF1 Tropics (ExpVar 27.2%)
(l) Ensemble mean EOF1 Tropics (ExpVar 31.9%)
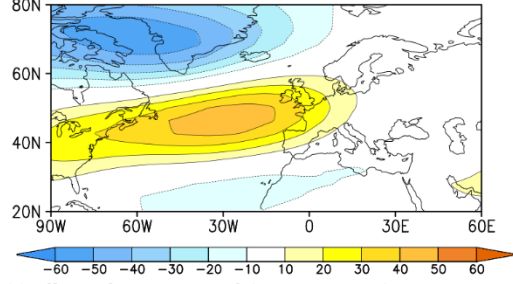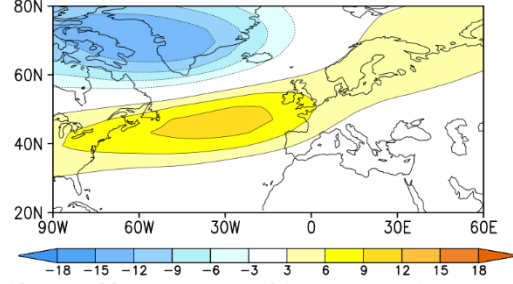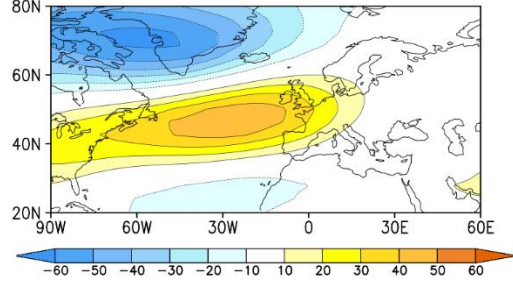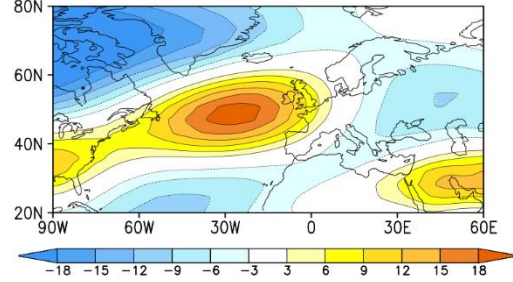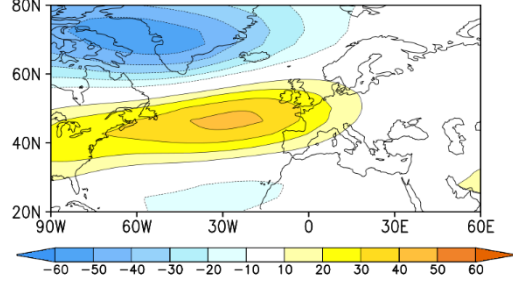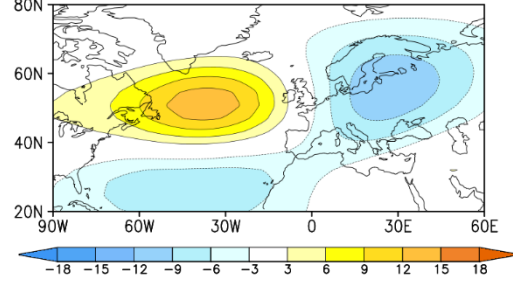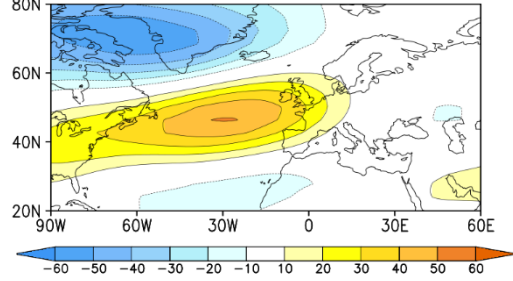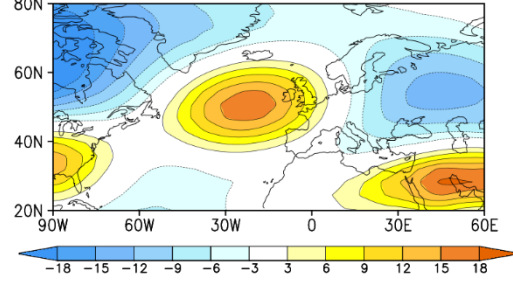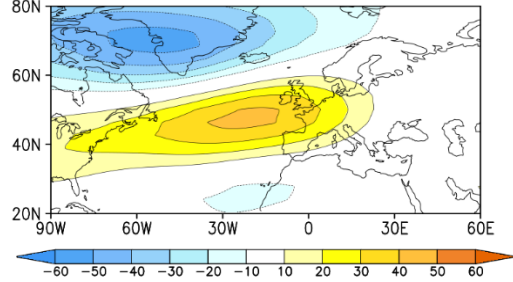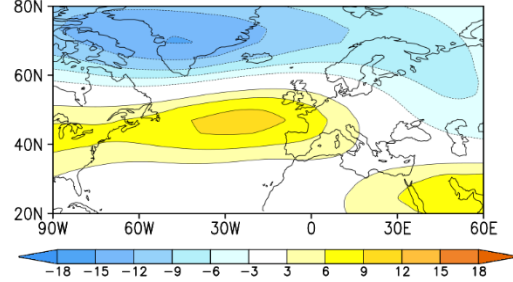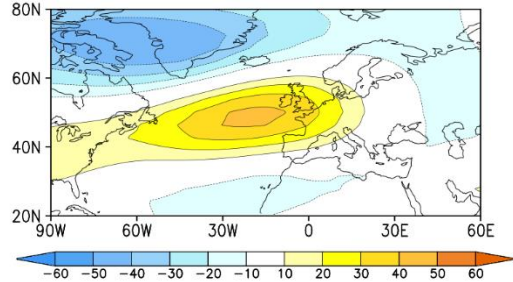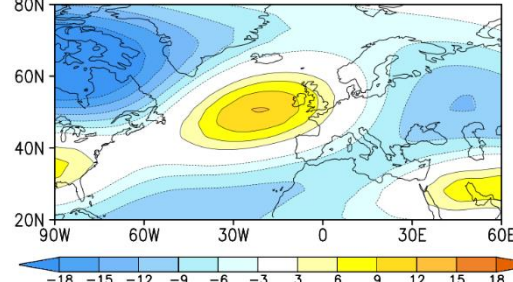
Figure 4.2 EOF1 pattern of geopotential heights at 200 hPa (GH200) [m] based on all ensemble members (left column) and the EOF1 pattern based on the ensemble mean (right column) in the period 1855-2010 in ICTP AGCM experiments: Clim, Ctrl, TroAtl, TroPac, TroInd, and Tropics. All in the JFM season. The percentage of explained variance (ExpVar) associated with each EOF pattern is indicated by the number in brackets.
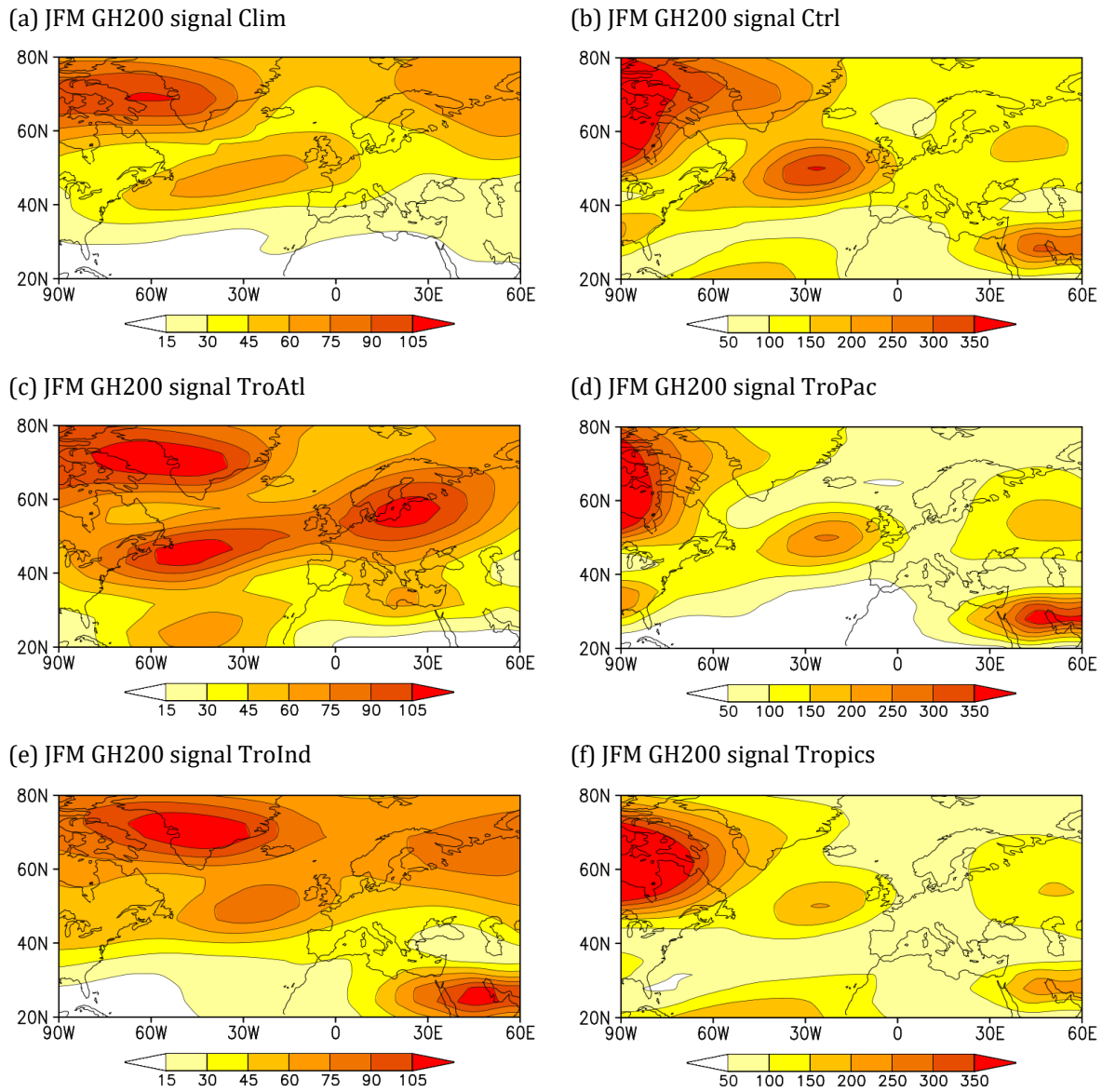
The first two EOF modes of JFM GH200 from the NOAA-CIRES-DOE 20th Century Reanalysis V3 dataset (Slivinski et al. 2019) for 1855-2010 are shown in Appendix B1. Both EOFs from the NOAA-CIRES-DOE reanalysis resemble the EOF1 and EOF2 patterns calculated based on all ensemble members of ICTP AGCM experiments (Figs. 4.2 and 4.3), respectively. However, NOAA-CIRES-DOE reanalysis EOF1 has a lower percentage of the explained variance than the EOF1 based on the ensemble mean (Fig. 4.2 left column), while the reanalysis EOF2 has a lower percentage of explained variance compared to both EOF2 patterns in AGCM experiments (Fig. 4.3).

4.3. Signal, noise and optimal patterns

The late-winter signal variance for GH200 (Fig. 4.4) is defined by the difference between the climatological and ensemble mean (Eq. 2.1). The Ctrl experiment has the strongest signal (Fig. 4.4b; NB different contouring intervals). Meanwhile, the GH200 signal over the NAE region in experiments with a smaller area of SST forcing (TroAtl: Fig. 4.4c; TroInd: Fig. 4.4e) and in the experiment without SST forcing (Clim, Fig. 4.4a) has a considerably smaller amplitude (cf. Figs. 4.4a, c, e with Figs. 4.4b, d, f). The signal in the Clim experiment (Fig. 4.4a), which is the weakest among all AGCM experiments, can be interpreted as a sort of numerical residual from applying Eq. 1 to the ensemble of climatological simulations. Since the individual simulations within the Clim experiment differ in initial conditions, the ensemble mean is not identical to the climatological mean, and, consequently, a weak numerical residual is obtained. Furthermore, since the signal for the other SST-forced experiments (Fig. 4.4b-f) consists of the forced component and this numerical residual, the Clim experiment could be used as a certain measure of significance for the signal in the rest of the AGCM experiments. Therefore, SST boundary forcing is essential for establishing a significant signal in the NAE region.

(a) All Members EOF2 Clim (ExpVar 16.8%)
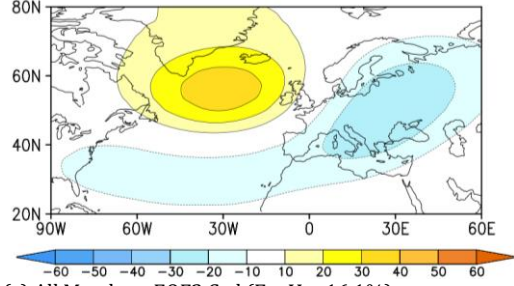
(b) Ensemble Mean EOF2 Clim (ExpVar 16.5%)
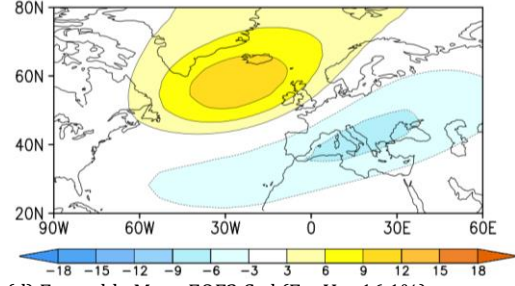
(c) All Members EOF2 Ctrl (ExpVar 16.1%)
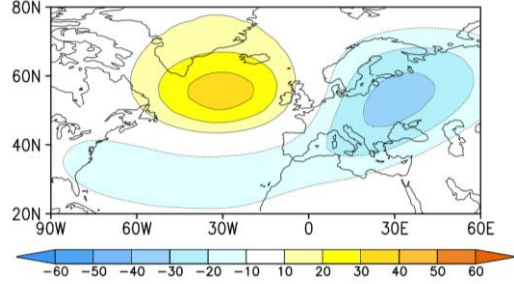
(d) Ensemble Mean EOF2 Ctrl (ExpVar 16.1%)
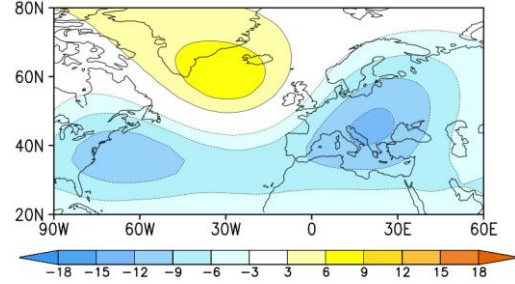
(e) All Members EOF2 TroAtl (ExpVar 17.6%)
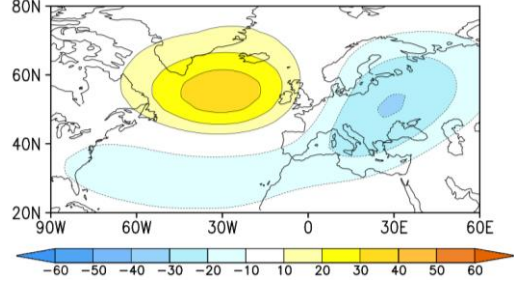
(f) Ensemble Mean EOF2 TroAtl (ExpVar 19.6%)
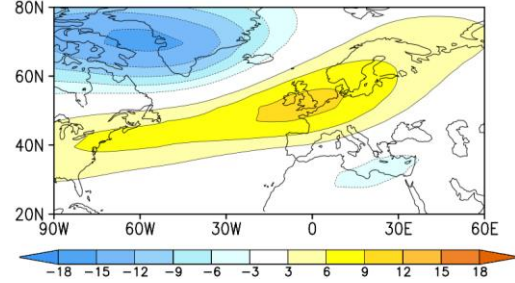
(g) JFM All Members EOF2 GH200 TroPac (ExpVar 17. 4%)
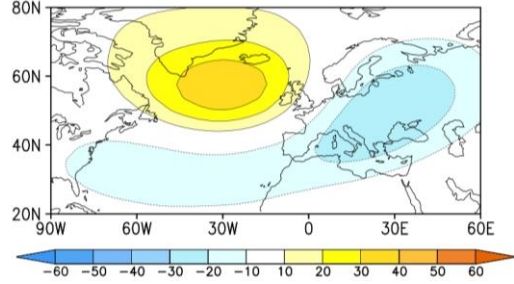
(h) Ensemble Mean EOF2 TroPac (ExpVar 19.2%)
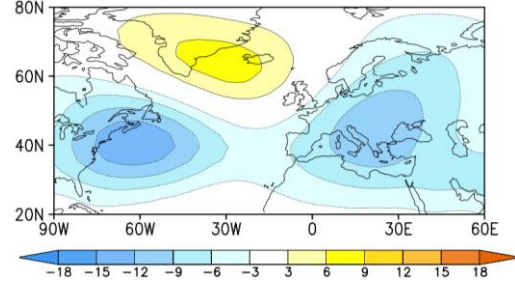
(i) All Members EOF2 TroInd (ExpVar 17.2%)
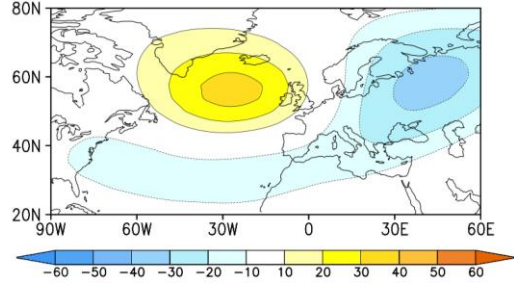
(j) Ensemble Mean EOF2 TroInd (ExpVar 16.0%)
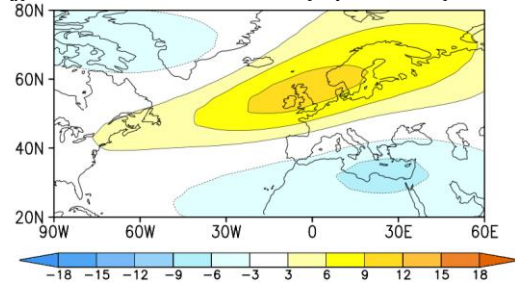
(k) All Members EOF2 Tropics (ExpVar 17.9%)
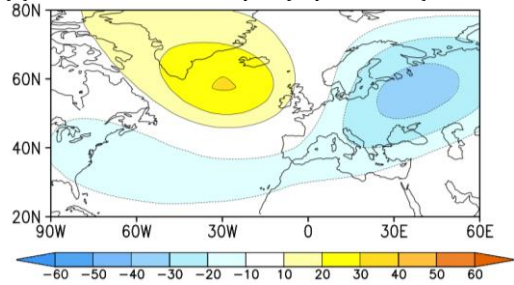
(l) Ensemble Mean EOF2 Tropics (ExpVar 14.1%)
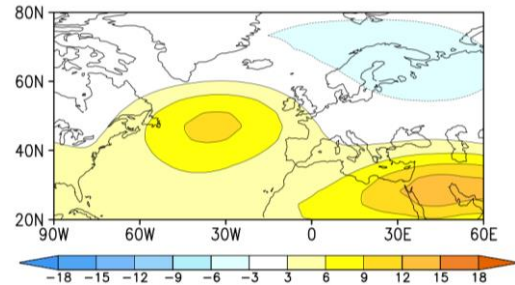
Figure 4.3 EOF2 pattern of JFM geopotential heights at 200 hPa (GH200) [m] based on all ensemble members (left column) and EOF2 pattern based on the ensemble mean (right column) in the period 1855-2010 in ICTP AGCM experiments: Clim, Ctrl, TroAtl, TroPac, TroInd, and Tropics. The percentage of explained variance (ExpVar) associated with each EOF pattern is indicated by the number in brackets.

(a) JFM GH200 signal Clim

(b) JFM GH200 signal Ctrl

(c) JFM GH200 signal TroAtl

(d) JFM GH200 signal TroPac

(e) JFM GH200 signal TroInd

(f) JFM GH200 signal Tropics

Figure 4.4 JFM signal variance of geopotential heights at 200 hPa [m^2] in ICTP AGCM experiments (a) Clim, (b) Ctrl, (c) TroAtl, (d) TroPac, (e) TroInd, and (f) Tropics for the 1855-2010 period.

Although having somewhat different amplitudes, the spatial distributions of the signal variance obtained in all AGCM experiments have similar characteristics. There are three most prominent areas containing the highest value of the signal – first in the northeast corner of the NAE region (60°-80° N, 90°-30° W), second over the North Atlantic (50° N, 60°-30° W), and third along the

south-western edge of the domain (20°N-30° N, 30°-60° E). However, the signal variance patterns in the Clim and TroAtl experiments (Fig. 4.4a and c) are missing the third centre, while the TroAtl signal has an additional maximum over northern Europe (50° N, 10°-50° E). Overall, the JFM GH200 signal (Fig. 4.4) is similar to the EOF1 patterns based on the ensemble mean (Fig. 4.2 right column) - the most prominent action centres of EOF1 patterns coincide with the areas containing the strongest signal.

The noise variance (Fig. 4.5) is defined by the deviations of individual ensemble members within each experiment from the ensemble mean (Eq. 2.2). The noise variance in all of the experiments has a dipolar structure, with the first centre in the upper left corner of the NAE domain, above western and south-western Greenland and the northern part of North America (60°-80° N, 90° W-20° E) and a second one above the North Atlantic (40°-55° N, 60° W-10° E). Here, the noise is generally reminiscent of the NAO.
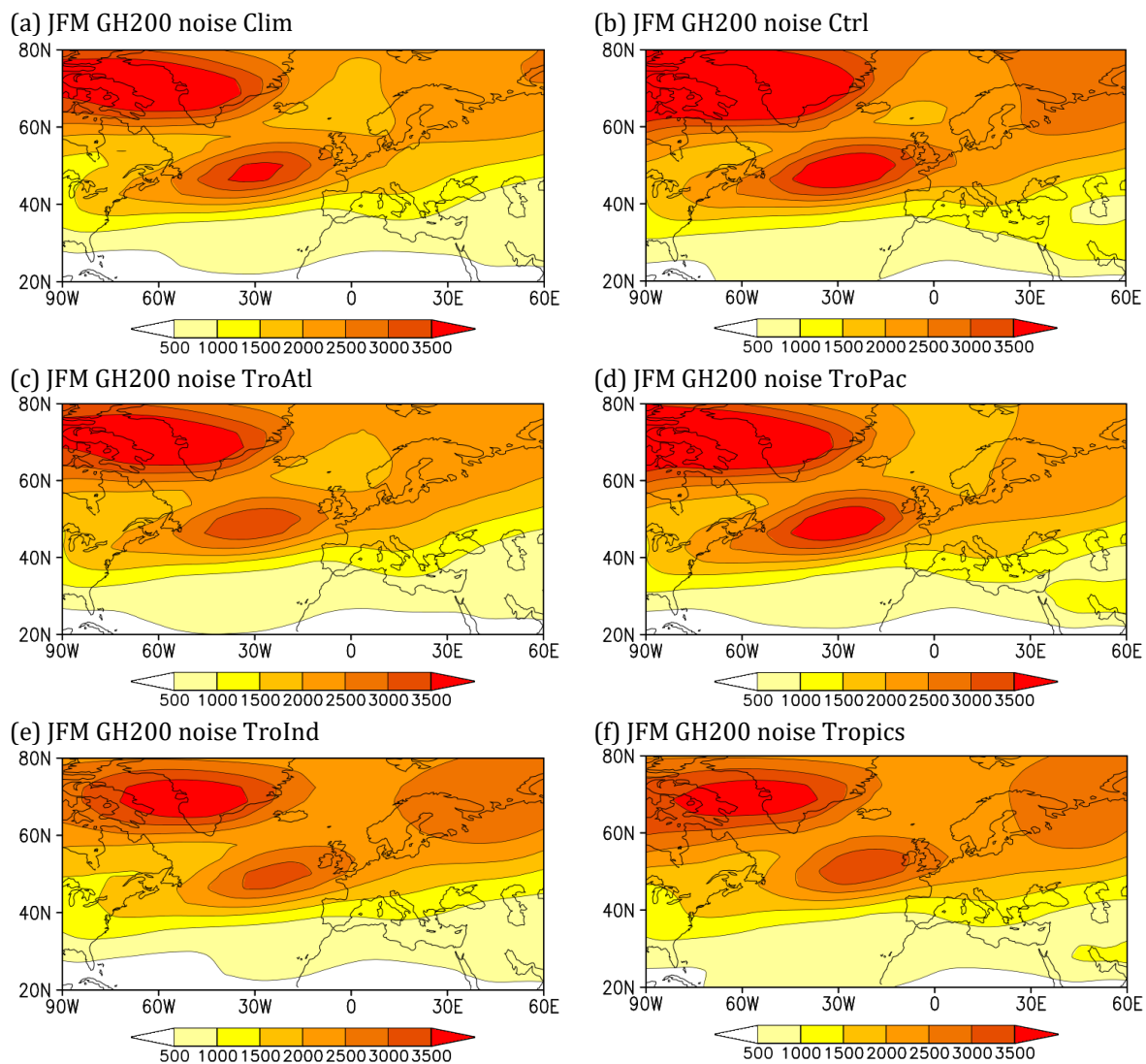
Figure 4.5 JFM noise variance of geopotential heights at 200 hPa [m^2] in ICTP AGCM experiments (a) Clim, (b) Ctrl, (c) TroAtl, (d) TroPac, (e) TroInd, and (f) Tropics for the 1855-2010 period.

The EOF1 pattern based on all ensemble members (Fig. 4.2 left column) also has a dipolar structure resembling the NAO. Since the ensemble members are initialised independently and have different realisations of internal variability, this NAO-like structure is not correlated between single model realisations. Consequently, the NAO manifests as noise in the model experiments when the noise is calculated as the deviation of a particular model realisation from the ensemble mean (Eq. 2.2). Moreover, the GH200 noise in late winter (Fig. 4.5) does not change its main spatial characteristics in different experiments, suggesting it is not impacted by the difference in SST boundary forcing imposed within the ICTP AGCM experiments.

The first spatial pattern from the signal-to-noise optimal pattern method (EOFOPT1) shows which pattern maximises the signal-to-noise ratio of GH200 in the JFM season. Here, EOFOPT1 patterns and the corresponding optimal signal-to-noise ratio are shown in Fig. 4.6. The EOFOPT1 patterns in the Ctrl, TroPac and Tropics experiments (Figs. 4.6b, d, f) bear the most resemblance. In these experiments, EOFOPT1 has two (Fig. 4.6b) or three maximums (Fig. 4.6d and f) extending from the North American coast over the North Atlantic and a separate one over the south-western edge of the domain, while the rest of the NAE region contains values of the opposite sign. The EOFOPT1 pattern in the Clim experiment (Fig. 4.6a) has centres of action with alternating signs forming a wave-like pattern throughout the NAE region. On the other hand, the TroAtl EOFOPT1 pattern (Fig. 4.6c) is divided into four sections with alternating signs of GH200 anomalies (first 20°-35° N, 90° W-0° E; second 40°-80° N, 90°-30° W; third 40°-80° N, 20° W-60° E; and fourth 20°-35° N, 0°-60° E). Meanwhile, the EOFOPT1 pattern has a dipolar structure in the TroInd experiment (Fig. 4.6e), with values of opposite signs in the northern and southern half of the domain.

To see if these patterns that optimise the signal-to-noise ratio display any temporal connections, we have calculated the correlations between the time series connected to each EOFOPT1 pattern in different AGM experiments (Fig. 4.7). The Ctrl, TroPac and Tropics experiments with the most similar optimal patterns also show the highest correlation between the PCAVG1 time series. On the other hand, the Clim optimal pattern does not have a significant temporal link to any optimal pattern in SST-forced experiments, as expected. The TroAtl PCAVG1 has a relatively high correlation with the corresponding Ctrl and Tropics time series (0.67). At the same time, the TroInd experiment shows a high correlation (around 0.7) with the Ctrl and Tropics experiments.

(a) JFM EOFOPT1 GH200 Clim

(b) JFM EOFOPT1 GH200 Ctrl

(c) JFM EOFOPT1 GH200 TroAtl

(d) JFM EOFOPT1 GH200 TroPac

(e) JFM EOFOPT1 GH200 TroInd

(f) JFM EOFOPT1 GH200 Tropics

(g) JFM EOFOPT1 GH200 SNR
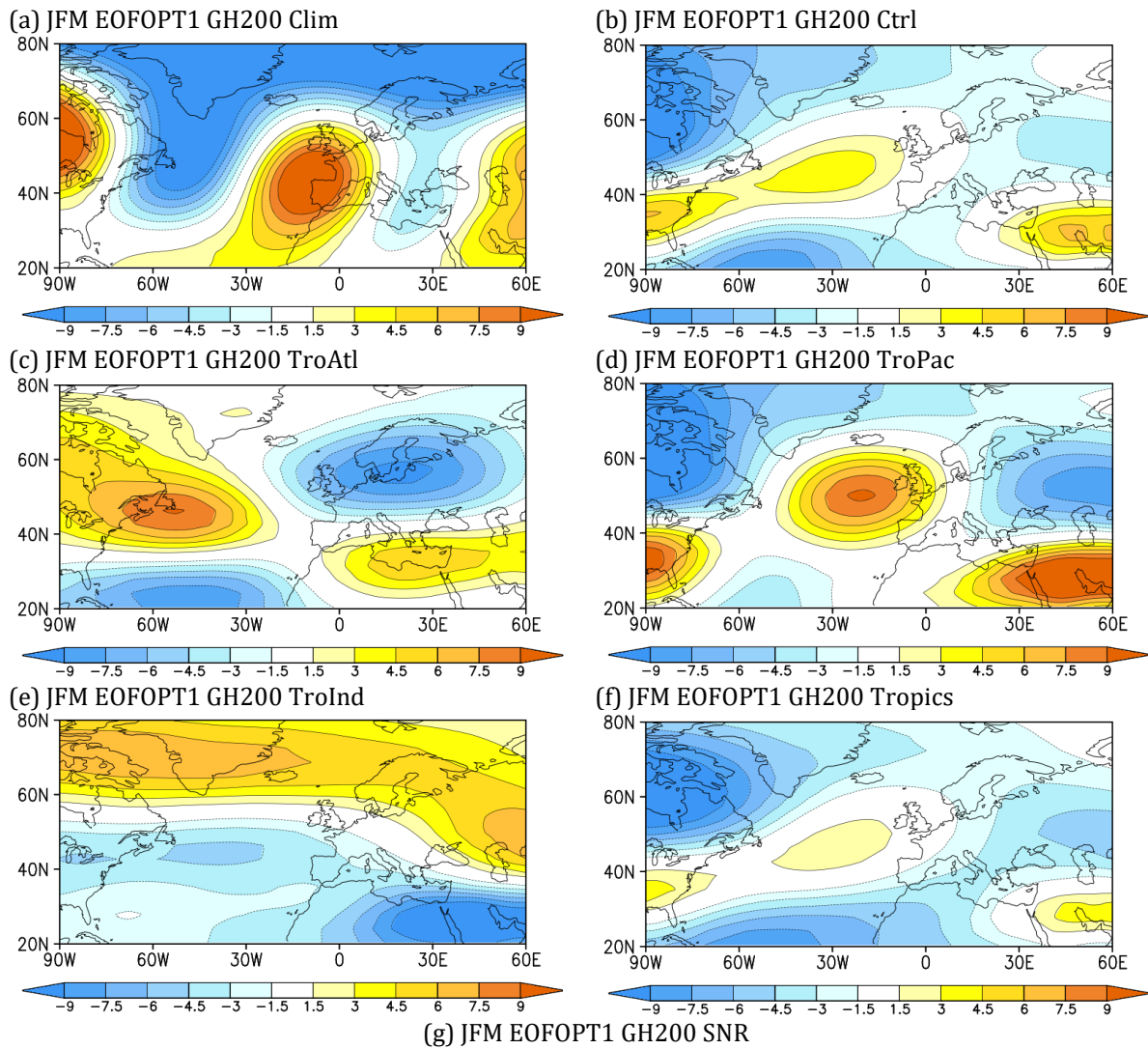
Figure 4.6 First optimal pattern (EOFOPT1) of JFM geopotential heights at 200 hPa (GH200) [m] in the period 1855-2010 in the ICTP AGCM experiments:(a) Clim, (b) Ctrl, (c) TroAtl, (d) TroInd, (e) TroPac, and (f) Tropics. Signal-to-noise ratio (SNR) of the EOFOPT1 mode (4.6g). All SNR values are considered statistically significant according to the F-test for the ratio of variances at the 95% confidence level.

Another variable connected to the JFM GH200 EOFOPT1 pattern is the corresponding signal-to-noise ratio (SNR) displayed in Fig. 4.6g. This SNR is estimated using the EOFOPT1 principal components (PCs) in each grid point. All SNR values shown in Fig. 4.6g are considered statistically significant according to the F-test for the ratio of variances on the 95% confidence level. By definition, SNR values larger than one are potentially predictable. The highest values of SNR for GH200 (Fig. 4.6g) are found for Ctrl, TroPac and Tropics experiments. Furthermore, the Ctrl, TroPac and Tropics experiments have similar EOFOPT1 patterns (Figs. 4.6b, d, f). The similarity between these patterns highlights the vital role of the tropical Pacific boundary forcing in enhancing the potential predictability of the NAE region. Furthermore, the joint contribution from all ocean basins in the tropical zone helps overcome the strong internal variability and establish potential predictability over the NAE region. At the same time, the SST boundary forcing outside the tropical zone does not contribute to a significant increase in the SNR (Fig. 4.6g). Once again, it is important to stress that the SNR obtained in the experiment without any imposed SST forcing (Clim; 0.05) is a numerical residual and has no physical basis. However, the Clim SNR can be used as an estimate of this numerical residual in the ensemble mean and a certain threshold of significance for the other SST-forced experiments.
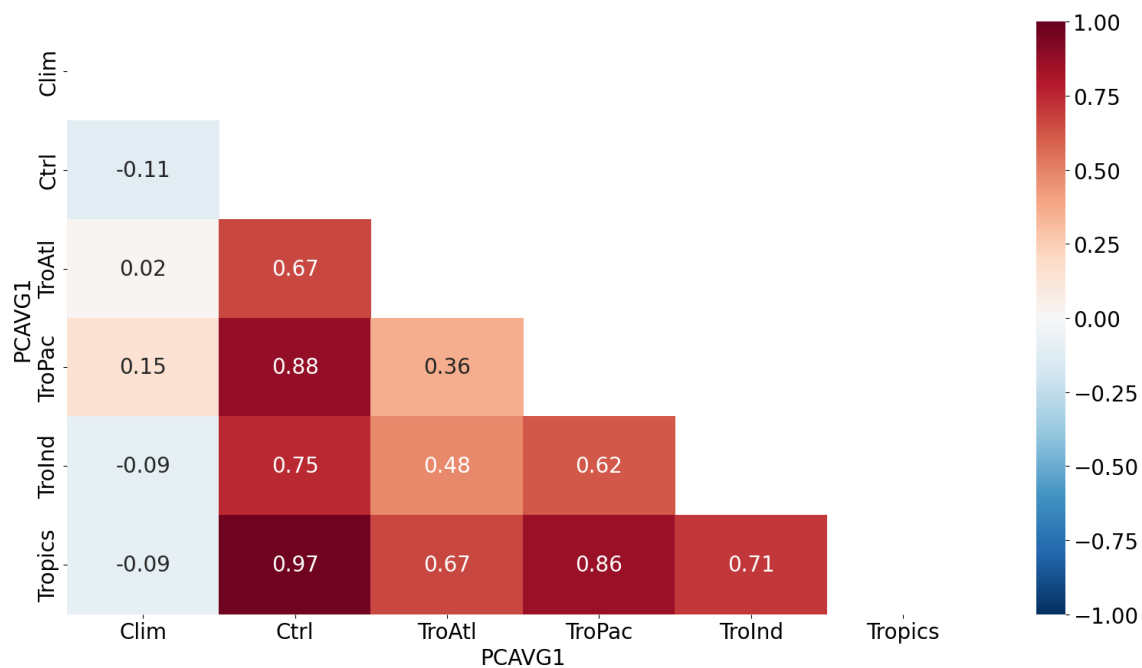
Figure 4.7 Correlation between the time series associated with the first optimal pattern (PCAVG1) of geopotential heights at 200 hPa (GH200) in JFM season in the 1855-2010 period for ICTP AGCM experiments: Clim, Ctrl, TroAtl, TroPac, TroInd and Tropics, respectively. All correlation coefficients besides the values for the Clim experiment (first column on the left) are considered statistically significant based on the two-tailed Student's t-test at the 95% confidence level.

Considering how similar the EOFOPT1 patterns (Fig. 4.6) are to the leading ensemble-mean EOF mode (Fig. 4.2 right column), the largest amount of explained variability of JFM GH200 apparently comes from the forced component. Meanwhile, the EOF1 mode based on all ensemble members (Fig. 4.2 left column) resembles the NAO more, suggesting it is connected to the internal variability of GH200 in late winter. To see if this spatial similarity of these patterns is reflected in the corresponding time series, the correlation between the first principal component (PC1) of the ensemble-mean GH200 and the time series associated with EOFOPT1 of GH200 (labelled PCAVG1) is given in Table 4.1. In the late winter season, the correlation between PC1 and PCAVG1 is the strongest in the TroPac experiment. The TroPac experiment shows similarities in the spatial characteristics of the JFM ensemble-mean EOF1 and EOFOPT1 patterns and their temporal variability. In the JFM season, the rest of the boundary-forced experiments (Ctrl, TroAtl, TroInd and Tropics) also have significant correlations, indicating the importance of the influence of tropical oceans outside the Pacific on the NAE sector. The AGCM experiment without SST boundary forcing (Clim) has the lowest correlation values, while the corresponding patterns are also dissimilar (cf. Figs. 4.2b and 4.6a).

Table 4.1 Correlation between the first principal component (PC1) of geopotential heights at 200 hPa (GH200) calculated for the ensemble mean (EnsMean) of each experiment and the time series associated with the first optimal pattern (PCAVG1) of GH200 in JFM season in the 1855-2010 period for ICTP AGCM experiments Clim, Ctrl, TroAtl, TroPac, and Tropics, respectively. Statistically significant values based on the two-tailed Student's t-test at the 95% confidence level are in boldface.

exp	Clim	Ctrl	TroAtl	TroPac	TroInd	Tropics
corr (PC1 EnsMean, PCAVG1)	0.06	**0.66**	**0.58**	**0.90**	**-0.70**	**0.81**

For completeness, we computed the correlations between the first principal components (PC1) of EOFs based on the ensemble mean (Fig. 4.8) between the ICTP AGCM experiments. Correlations shown in Fig. 4.8 agree with the previously described results displayed in Fig. 4.2 (right column) and Table 4.1. Firstly, the correlations for the Clim experiment are small and are not statistically significant. Also, the Ctrl, TroPac and Tropics ensemble-mean EOF1 patterns (Fig. 4.2d, h, l), which are the most similar, are simultaneously the most highly correlated. The rest of the SST-forced AGCM experiments yield smaller but significant correlations.
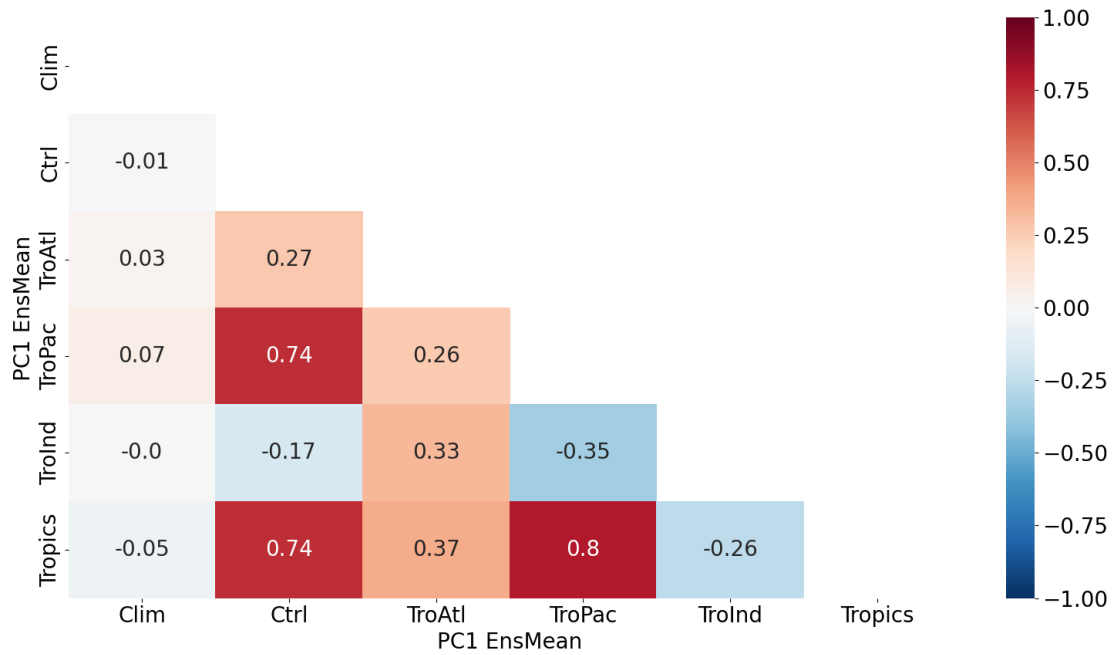
Figure 4.8 Correlation between the first principal components (PC1) of geopotential heights at 200 hPa (GH200) calculated for the ensemble mean (EnsMean) of each experiment in the JFM season in the 1855-2010 period for ICTP AGCM experiments Clim, Ctrl, TroAtl, TroPac, and Tropics, respectively. All correlations besides the values for the Clim experiment (first column on the left) are considered statistically significant based on the two-tailed Student's t-test at the 95% confidence level.

4.4. Correlation with lower-boundary forcing

The spatial distribution of the first optimal patterns differs among the experiments (Fig. 4.6), pointing toward the potential dependence of the EOFOPT1 patterns on the SST forcing prescribed in different ocean basins in the tropical zone. To verify the connection between the temporal variability of the SST forcing and optimal patterns, we calculated the correlation between the first principal component (PC1) of SST anomalies and the time series associated with the first optimal pattern (PCAVG1) of GH200, shown in Table 4.2. Here, the index based on SST anomalies describes the interannual variability in selected tropical ocean areas that coincide with the configuration of boundary forcing within the model simulations (Fig. 4.1). These correlation coefficients show the temporal link between the signal and boundary forcing. Overall, different ICTP AGCM experiments show the highest correlation to SST anomalies in oceans corresponding to the SST boundary forcing prescribed in those experiments. The Ctrl optimal pattern is highly correlated to SST anomalies in all selected ocean areas. In the case of the TroPac experiment, correlations reach the highest values for tropical Pacific and SST anomalies in the entire tropical zone (0.95). These are also the highest correlations shown in Table 4.2. The optimal pattern in the TroInd experiment has the most considerable correlation to the SST anomalies in the tropical Indian Ocean, while this is true for SST anomalies in the

entire tropical zone for the Tropics experiment. On the other hand, the TroAtl PCAVG1 shows a relatively small correlation to the PC1 of tropical Atlantic SST anomalies and the lowest values of correlation coefficients overall. Moreover, the TroAtl signal-to-noise ratio is the smallest among the SST-forced experiments (Fig. 4.6g).

Table 4.2 Correlation between the first principal component (PC1) of NOAA sea surface temperature anomalies (SSTA) and the time series associated with the first optimal pattern (PCAVG1) of geopotential heights at 200 hPa (GH200) in JFM season in the 1855-2010 period for ICTP AGCM experiments Ctrl, TroAtl, TroPac, TroInd, and Tropics, respectively. The EOF analysis was applied on SSTA in the same areas as the SST-boundary forcing within ICTP AGCM experiments, which are shown in Fig. 4.1: TroAtl (30° S-30° N, 100° W-20° E), TroPac (30° S-30° N, 120° E-60° W), TroInd (30° S-30° N, 30° E-120° E), and Tropics (30° S-30° N, 0° E-360° E). All values are considered statistically significant based on the two-tailed Student's t-test at the 95% confidence level.

	Ctrl GH200 PCAVG1	TroAtl GH200 PCAVG1	TroPac GH200 PCAVG1	TroInd GH200 PCAVG1	Tropics GH200 PCAVG1
TroAtl SSTA PC1	**0.81**	**0.42**	**0.77**	**0.47**	**0.81**
TroPac SSTA PC1	**0.88**	**0.34**	**0.95**	**0.60**	**0.87**
TroInd SSTA PC1	**0.81**	**0.51**	**0.71**	**0.86**	**0.78**
Tropics SSTA PC1	**0.91**	**0.41**	**0.95**	**0.66**	**0.90**

Generally, the conclusions drawn from Table 4.2 are affirmed by the correlations between PCAVG1 of GH200 and global NOAA SST anomalies shown in Fig. 4.9. For instance, in the climatological experiment (Fig. 4.9a), correlations are weak in all ocean basins. Even though the Clim experiment is not boundary-forced, the GH200, a purely atmospheric component, can exert a certain degree of influence on the ocean, as expressed in the Clim correlation map. Therefore, as was the case for the signal based on Eq. 2.1 (Fig. 4.4), the Clim experiment can be used as a base significance level for the other AGCM experiments.

(a) corr (Clim PCAVG1, SSTA)

(b) corr (Ctrl PCAVG1, SSTA)

(c) corr (TroAtl PCAVG1, SSTA)

(d) corr (TroPac PCAVG1, SSTA)

(e) corr (TroInd PCAVG1, SSTA)

(f) corr (Tropics PCAVG1, SSTA)
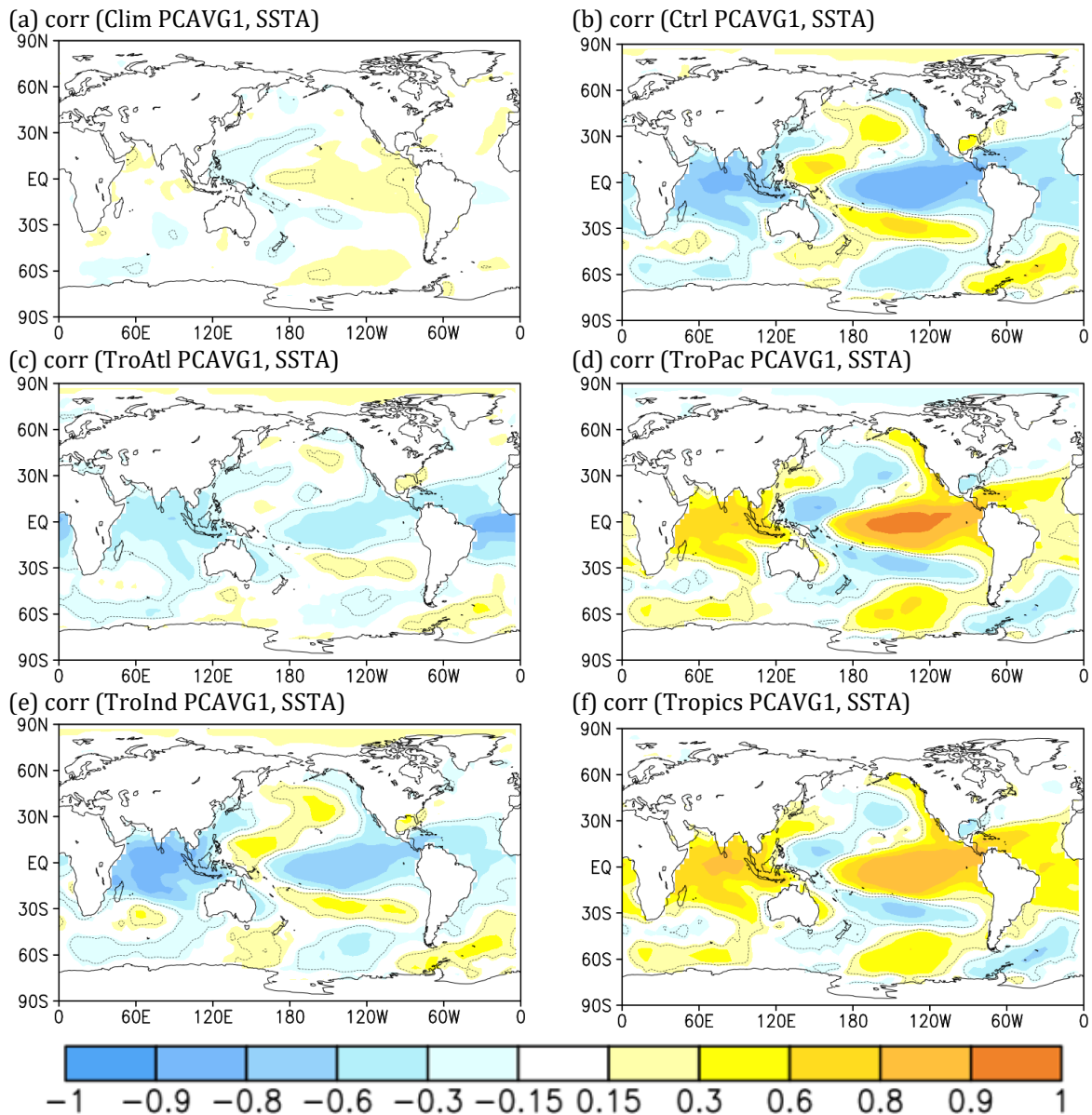
Figure 4.9 Correlation of global NOAA SST anomalies and the time series associated with the first optimal pattern (PCAVG1) of JFM geopotential heights at 200 hPa (GH200) in the period 1855-2010 for ICTP AGCM experiments: (a) Clim, (b) Ctrl, (c) TroAtl, (d) TroPac, (e) TroInd, and (f) Tropics. All statistically significant values based on the two-tailed Student's t-test on the 95% confidence level are encircled by dashed contours

On the other hand, correlation maps for the Ctrl and Tropics experiments (Figs. 4.9b and f) have similar spatial characteristics, with significant correlation coefficients found in the tropical zones of the Pacific and Indian Oceans and the Atlantic to a lesser degree. In the TroPac experiment (Fig. 4.9d), the most prominent area with significant correlations is found in the tropical Pacific, which resembles the "canonical" ENSO signature (Brönnimann 2007), where the correlations also reach the highest values overall (between 0.9 and 1.0). In the TroInd experiment (Fig. 4.9e), PCAVG1 is highly correlated with the SST anomalies in the tropical Indian Ocean (between -0.7 and -0.9), followed by SST anomalies in the tropical Pacific (between -0.5 to -0.7). In contrast to

the results shown in Table 4.2, the TroAtl experiment (Fig. 4.9c) displays the highest correlation between PCAVG1 and SST anomalies in the area of tropical Atlantic close to the Equator (between -0.7 and -0.9). Overall, the results from Fig. 4.9 further emphasise the significant role of the SST forcing in the tropical zone of the Atlantic, Pacific, and Indian Oceans in optimising the signal-to-noise ratio of GH200 in late winter.

Optimal patterns (Fig. 4.6) highlighted areas within the NAE domain with the highest signal-to-noise ratio values. Also, the significant correlation between PC1 of SST anomalies and the time series corresponding to the first optimal pattern (PCAVG1), presented in Table 4.2, implied a link between the signal and prescribed SST forcing. At the same time, the centres of action in the EOFOPT1 patterns (Fig. 4.6) coincide with those in the ensemble-mean EOF1 patterns (Fig. 4.2 right column). Therefore, we examine the correlation between the first principal component (PC1) of SST anomalies in the previously chosen ocean basins and the first principal component (PC1) of GH200 calculated for the ensemble mean of each experiment (Table 4.3). These correlations should reveal a possible connection between the SST boundary forcing and GH200 variability (i.e., EOF1) over the NAE region. Firstly, the correlation values in Table 4.3 are consistently smaller than those displayed in Table 4.2. Moreover, the correlations in Table 4.3 demonstrate the degree to which the boundary-forcing impacts this first EOF mode. In general, the TroPac and Tropics experiments are highly correlated to all selected SST indices, while the Ctrl correlations are consistently smaller but still significant.

Table 4.3 Correlation between the first principal component (PC1) of NOAA sea surface temperature anomalies (SSTA) and the first principal component (PC1) of geopotential heights at 200 hPa (GH200) in JFM season calculated for the ensemble mean (EnsMean) of each experiment in the 1855-2010 period for ICTP AGCM experiments Ctrl, TroAtl, TroPac, TroInd, and Tropics, respectively. The EOF analysis was applied on SSTA in the same areas as the SST-boundary forcing within ICTP AGCM experiments, which are shown in Fig. 4.1: TroAtl (30° S-30° N, 100° W-20° E), TroPac (30° S-30° N, 120° E-60° W), TroInd (30° S-30° N, 30° E-120° E), and Tropics (30° S-30° N, 0° E-360° E). All values are considered statistically significant based on the two-tailed Student's t-test at the 95% confidence level.

	Ctrl GH200 PC1 EnsMean	TroAtl GH200 PC1 EnsMean	TroPac GH200 PC1 EnsMean	TroInd GH200 PC1 EnsMean	Tropics GH200 PC1 EnsMean
TroAtl SSTA PC1	**0.55**	**0.33**	**0.69**	**-0.25**	**0.69**
TroPac SSTA PC1	**0.70**	**0.27**	**0.87**	**-0.33**	**0.81**
TroInd SSTA PC1	**0.47**	**0.37**	**0.64**	**-0.52**	**0.59**
Tropics SSTA PC1	**0.69**	**0.31**	**0.86**	**-0.37**	**0.81**

In the case of the TroInd experiment with the smallest area of applied SST forcing (Fig. 4.1d), correlations in Table 4.3 are relatively small for SST indices defined outside the tropical Indian ocean. Moreover, the first optimal pattern and ensemble-mean EOF1 pattern for the TroInd experiment are visibly different (cf. Figs. 4.2l and 4.6e). Simultaneously, the TroInd EOFOPT1 pattern differs from the rest of the SST-forced experiments (cf. Figs. 4.6e and 4.6b, c, d, f). Recent studies emphasised the effect of the Indian Ocean on the NAE atmosphere in early winter (Abid et al. 2020; Joshi et al. 2021). However, the analysis presented in this paper is focused on the late winter season. Therefore, this sub-seasonal shift could be one of the reasons behind the observed differences in the results for the TroInd experiment compared to the rest of the SST-forced AGCM experiments. Additionally, Dogar et al. (2017) raised concern about ICTP AGCM's ability to faithfully reproduce the ENSO-induced temperature pattern over the tropical Indian Ocean.

4.5. Dynamical mechanisms

Reviewing the existing literature, including observational and modelling studies, a dynamical perspective of the results previously described in this chapter is offered. Among the AGCM experiments with prescribed tropical SST forcing, the largest signal over the NAE area is found in the simulations within the TroPac and Tropics experiments (Fig. 4.4). Therefore, the results presented in this chapter highlight the role of the tropical Pacific, the starting point of ENSO events. During boreal winter, the atmospheric response to ENSO forcing in the tropical Pacific can impact other oceans via the atmospheric bridge. Analysis of the ENSO signal in basins other than the tropical Pacific points to a warming of the Indian Ocean and parts of the tropical Atlantic during the El Niño phase (Alexander et al. 2002 and references therein).

At the same time, between the experiments with SST forcing prescribed only within the tropical zone, the highest signal-to-noise ratio is found for the Tropics experiment (Fig. 4.6), pointing towards a synergistic effect of all the oceans in the tropical zone on the enhancement of the potential predictability of the atmospheric circulation in the NAE region. Tropical SST boundary forcing causes anomalous divergence in the upper atmospheric layers, which acts as a Rossby wave source (Sardeshmukh and Hoskins 1988). Rossby waves then propagate towards the NAE region through the troposphere (e.g., Jiménez-Esteve and Domeisen 2018) and stratosphere (Ineson and Scaife 2009; Domeisen et al. 2019). Thus, a part of atmospheric circulation in the NAE region develops as a response to this boundary forcing and consequently, the boundary forcing-induced predictable components arise.

It has been argued that the Indian Ocean SSTs have an impact on the NAE area, especially the NAO (Bader and Latif 2003, 2005; Hoerling et al. 2004; Kucharski et al. 2006a), which could even be used for the improvement of seasonal forecasts (Hardiman et al. 2020). However, in the previous subsections, a certain discrepancy between the results of the TroInd experiment and the other SST-forced experiments was already pointed out. Dogar et al. (2017) found that the ICTP AGCM was unsuccessful in simulating the ENSO-induced temperature pattern over the tropical Indian Ocean but simultaneously reported its ability to skilfully reproduce the ENSO impact on the atmospheric circulation over Africa, North and South America, and the Pacific. Also, the influence of the Indian Ocean on the NAE circulation seems to be more important in the early compared to the late-winter season (Abid et al. 2020; Joshi et al. 2021).

Consistently significant correlations between SST anomalies in the tropical Atlantic and EOF and optimal patterns of geopotential heights at 200 hPa level over the NAE region (Tables 4.2 and 4.3) demonstrate that the boundary forcing in this particular ocean area impacts variability and predictable components of GH200 in the NAE region. This tropical Atlantic response is often linked to ENSO. Proposed mechanisms connecting the tropical North Atlantic and ENSO are summarized in Figure 1. in the study by García-Serrano et al. (2017). Those mechanisms include a Kelvin wavefront, extratropical Rossby wave train, changes in the Pacific Walker cell and Atlantic Hadley cell, and a remote Gill-type response. Moreover, using a ray-tracing method, Toniazzo and Scaife (2006) found that, even in the absence of SST anomalies in the Atlantic itself, strong ENSO events may trigger an NAE response originating in the tropical Atlantic. On the other hand, there is evidence supporting the hypothesis that the tropical Atlantic can act as a source of predictability for the NAE region independently of ENSO. For example, Mezzina et al. (2020b) found a certain amount of skill in the subtropical North Atlantic unrelated to ENSO events. The Atlantic SST anomalies have also been linked to the winter precipitation over Europe and North Africa (Rodríguez-Fonseca et al. 2006), as well as the NAO (Okumura et al. 2001; Czaja and Frankignoul 2002).

5. Impact of tropical SSTs on the atmospheric signal variance in the NAE area

The monthly signal variance of geopotential heights at 200 hPa from ICTP AGCM experiments with differently prescribed boundary forcing was calculated to test the sub-seasonal modulation of teleconnections to the North Atlantic-European area and is presented in the following chapter.

5.1. ICTP AGCM simulations

The monthly signal variance (Eq. 2.1) is calculated for six ICTP AGCM experiments, which were described in the previous chapter (Ctrl, TroAtl, TroInd, TroPac, Tropics, and Clim; cf. Fig. 4.1). All simulations cover the period between 1855 and 2010. Since the signal variance in the late winter season has shown to be relatively high over North America and the Arabian Penninsula in certain ICTP AGCM experiments (Fig. 4.4). Therefore, the NAE area of analysis is condensed here compared to the previous chapter to have a clearer focus on the region of interest. The new, more focused NAE region under consideration here in this chapter extends from 30° to 60° N, and from 50° W to 30° E.

5.2. Late-winter signal variance

The late-winter (January-February-March) monthly GH200 signal over the North Atlantic-European region is shown in Fig. 5.1. In the control experiment, the signal has a dominantly monopolar structure, with a prominent maximum over the North Atlantic (40° N-60° N, 50° W-10° E), with the largest amplitude in January, and weakest in March (Fig. 5.1a-c). The signal variance has similar spatial characteristics in the TroAtl and Tropics experiments (Fig. 5.1j-o) but is less pronounced than the Ctrl signal, especially in January. Meanwhile, the TroInd and TroAtl signal (Fig. 5.1d-i) is weaker than in the other AGCM experiments containing SST boundary forcing. However, the signal shares its characteristic monopole shape in January in the

case of TroInd (Fig. 5.1g), and in January and February in the TroAtl experiment (Fig. 5.1d and e). On the other hand, in the experiment containing only climatological values of the SSTs, the signal has a maximum over the North Atlantic in January and February (Fig. 5.1p and r) and is comparable to their TroAtl and TroInd counterparts in amplitude.
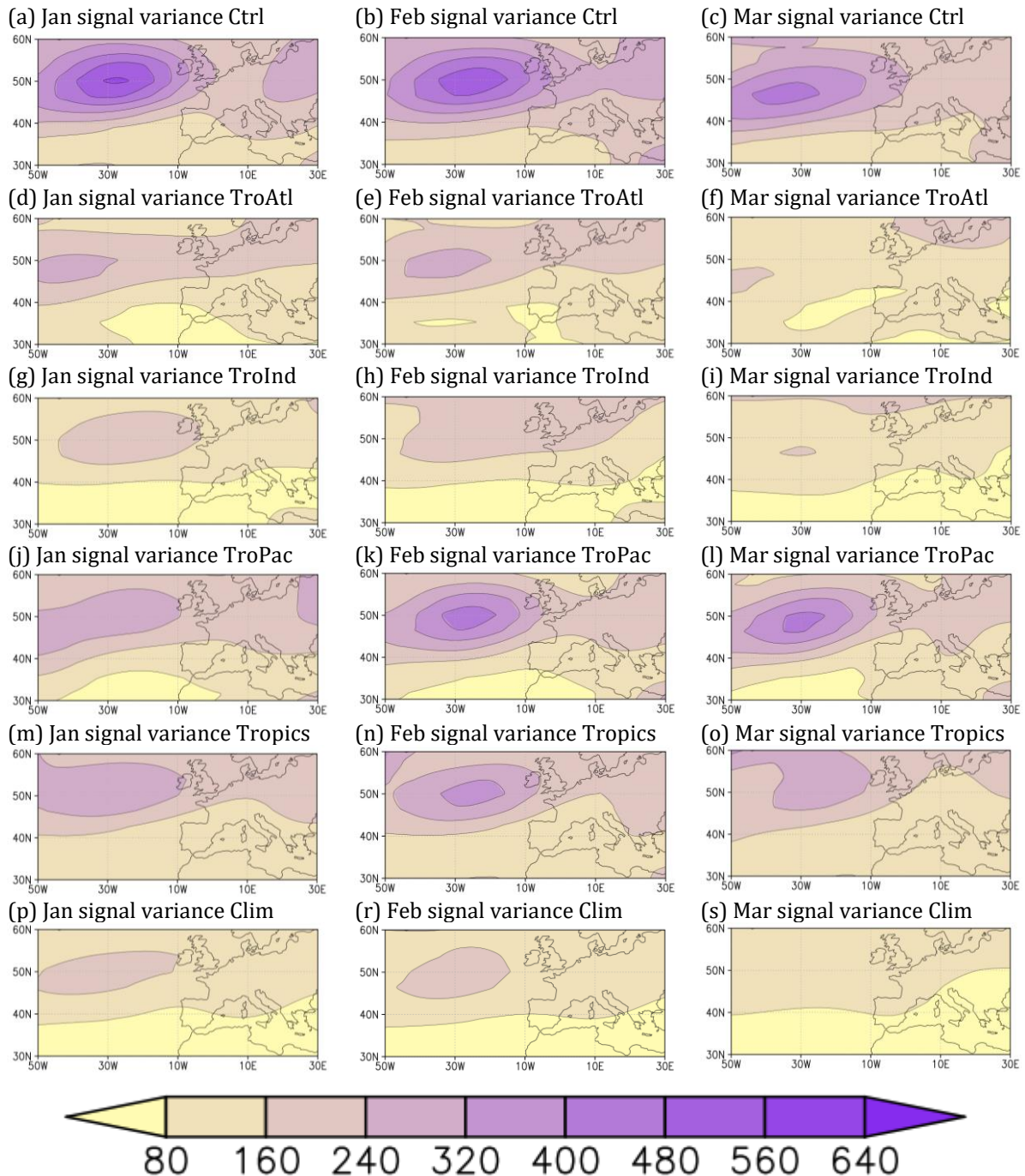
Figure 5.1 Signal variance of geopotential heights at 200 hPa [m^2] in January (left), February (middle), and March (right) in the North Atlantic-European region (30°-60° N, 50° W-30° E) for the whole 156-year period (1855-2010) in ICTP AGCM experiments: Ctrl, TroAtl, TroInd, TroPac, and Tropics, respectively.

The signal variance shape in the Clim experiment suggests that the monopole pattern of the signal over the NAE region is a product of the internal variability of the atmosphere. However, the forcing of the tropical oceans, especially the tropical Pacific, strengthens this already existing signal and increases its persistence. Therefore, we can use the Clim signal as a threshold for the significance of the forced component of the late-winter GH200 signal.

Here, the late-winter GH200 signal in the AGCM experiments containing SST forcing resembles the JFM ensemble-mean EOF1 spatial pattern and the first mode of the signal-to-noise optimal patterns method (Figs. 4.2 and 4.6).

Appendix C1 shows the late-winter signal in the Northern Hemisphere. Overall, the signal is the strongest over the Pacific North American region. The rest of the conclusions from the NAE signal (Fig. 5.1) also apply to the signal in the whole Northern Hemisphere.

5.3. ENSO and non-ENSO signal variance

To examine the influence of ENSO events, we calculated the signal variance based on the selected 53 ENSO years and 57 non-ENSO years, as described in the Methods section. Figure 5.2 shows the ENSO signal variance in January, February, and March. Same as in the Ctrl pattern in Fig. 5.1, the ENSO signal variance in the Ctrl experiment (Fig. 5.2a-c) has a predominantly monopolar pattern. The strongest signal for the selected ENSO years is found in February and March in the TroPac experiment (Fig. 5.2k and l). As we expand the area of the prescribed boundary forcing to the whole tropical zone, the signal weakens. The Tropics signal variance (Fig. 5.2m-o) is similar to its Ctrl and TroPac experiments but has a smaller amplitude. Compared to the rest AGCM experiments, the TroAtl, TroInd, and Clim ENSO values are weaker (Fig. 5.2d-i and p-s). Also, the TroPac ENSO signal variance (Figs. 5.2g, h and i) is stronger than their counterparts calculated for all years (Figs. 5.1g, h and i) over the NAE region.

The Northern Hemisphere ENSO signal can be found in Appendix C2. The two centres in the Pacific North American region are the most prominent spatial patterns of the signal variance in the Ctrl, TroPac and Tropics experiments, while the amplitude is less pronounced in the TroInd experiment. Meanwhile, the experiment with SST anomalies prescribed only in the tropical Atlantic and the climatological experiment are mutually comparable but have the weakest amplitude compared to the other AGCM experiments.
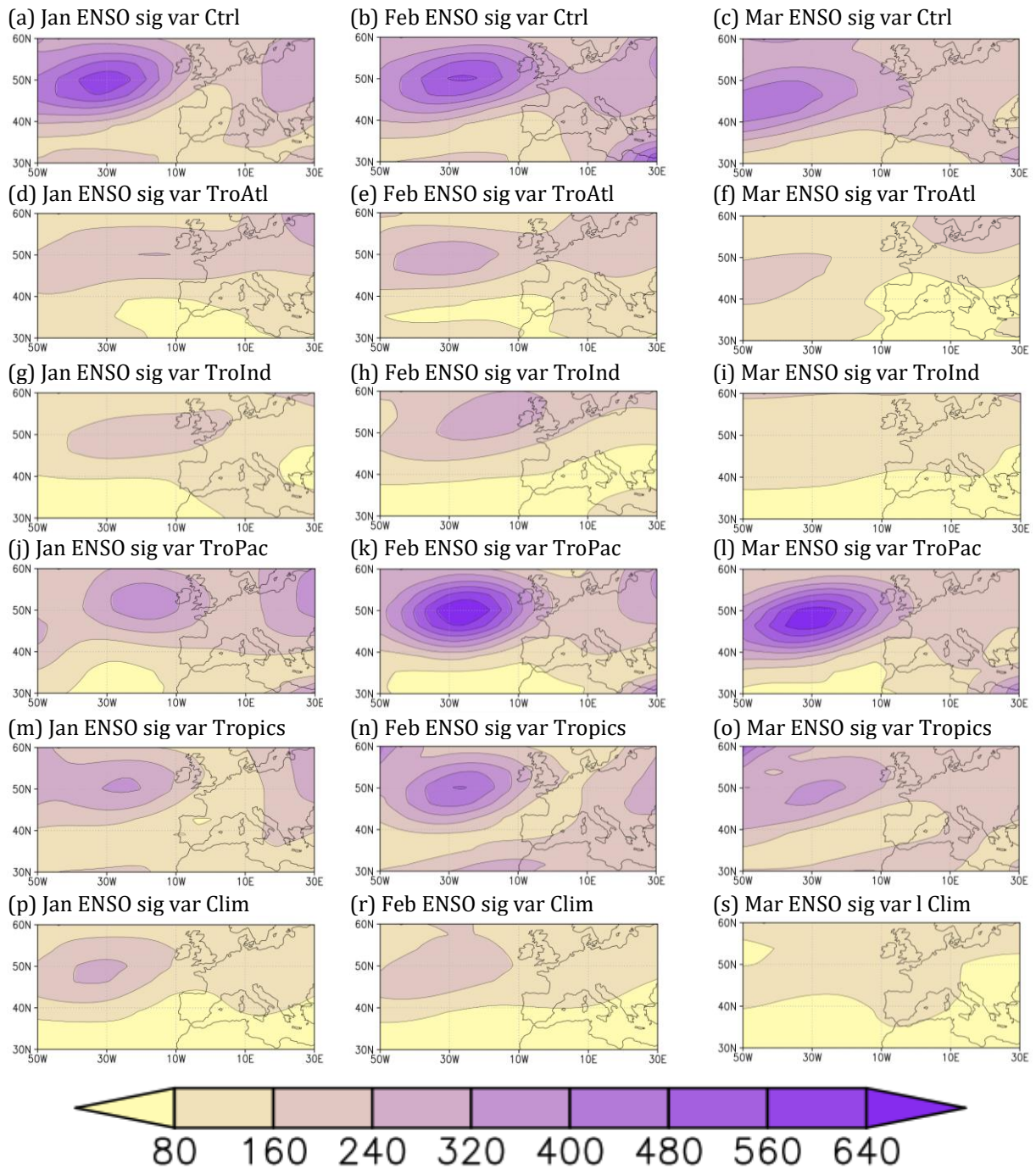
Figure 5.2 Signal variance (sig var) of geopotential heights at 200 hPa [m^2] in the 53 ENSO years in January (left), February (middle), and March (right) in the North Atlantic-European region (30°-60° N, 50° W-30° E) in ICTP AGCM experiments: Ctrl, TroAtl, TroInd, TroPac, Tropics and Clim, respectively. The ENSO years were selected from the 156 years (1855-2010) according to the strength of the Niño3.4 index in the JFM season.

The late-winter signal variance is also calculated for non-ENSO years (Fig. 5.3). In the Ctrl (Fig. 5.3 a-c) and Tropics (Fig. 5.3 j-f) experiment, the non-ENSO signal variance retains the monopolar shape similar to the signal calculated for all years (Fig. 5.1) and ENSO years (Fig. 5.2). Simultaneously, the TroAtl (Fig. 5.3d-f) and TroPac experiments (Fig. 5.3 j-l) have a predominantly zonal shape with a smaller amplitude. The TroInd experiment has a weak centre

in January (Fig. 5.3g), while the February and March signals (Fig. 5.3 h and i) are more zonally extended across the NAE region. The Clim signal variance in February and March (Fig. 5.3 r and s) is the weakest among all experiments.
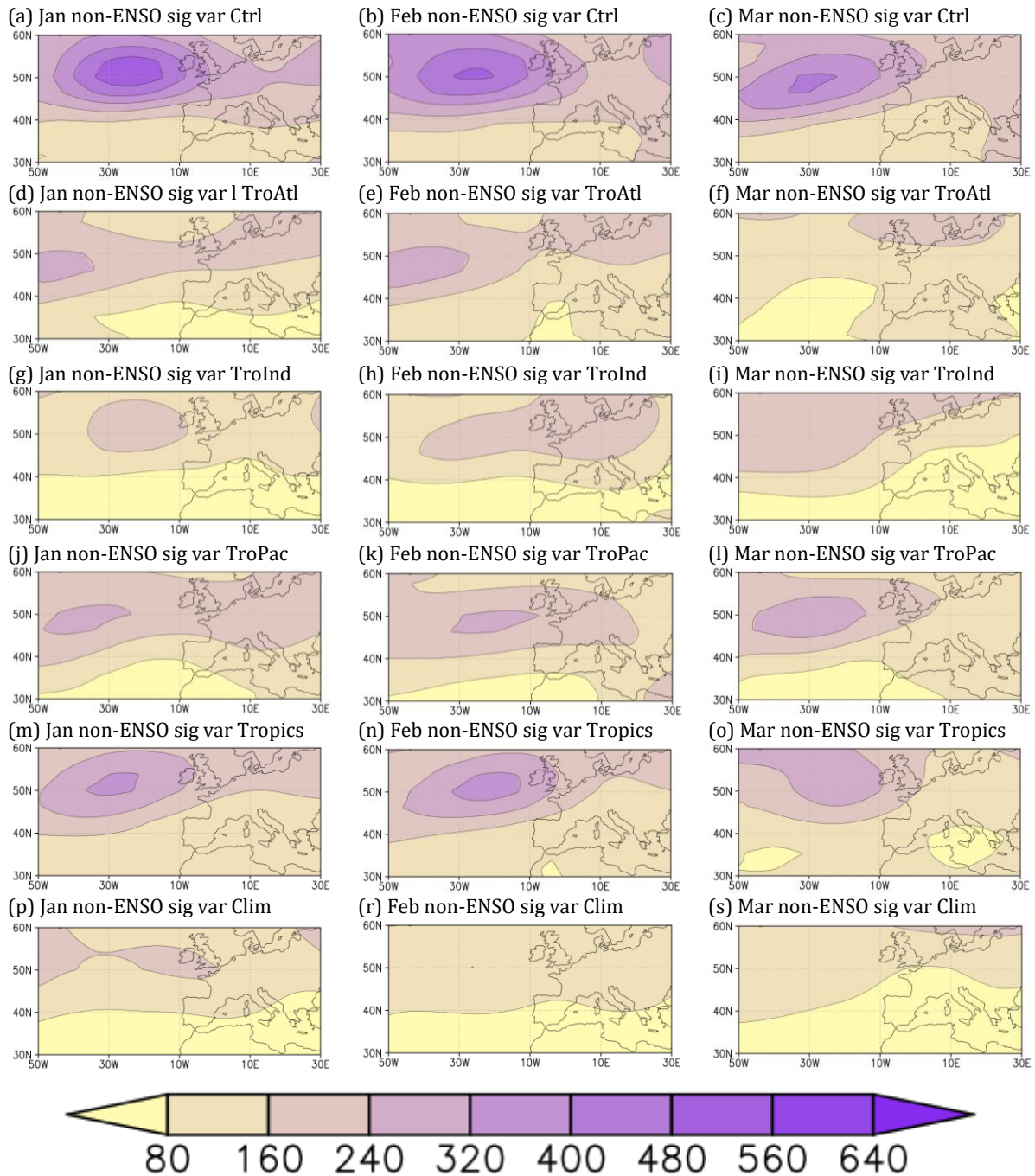
Figure 5.3 Signal variance (sig var) of geopotential heights at 200 hPa [m^2] in the 57 non-ENSO years in January (left), February (middle), and March (right) in the North Atlantic-European region (30°-60° N, 50° W-30° E) in ICTP AGCM experiments: Ctrl, TroAtl, TroInd, TroPac, Tropics and Clim, respectively. The non-ENSO years were selected from 156 years (1855-2010) according to the strength of the Niño3.4 index in the JFM season.

Comparing the ENSO and non-ENSO signal variance in the Ctrl experiment (cf. Figs. 5.2 a-c and Figs. 5.3 a-c), it is visible that the non-ENSO signal variance in the NAE region is almost as large

as the ENSO signal variance. However, that is not the case for the TroPac experiment, which has the most pronounced difference between the ENSO and non-ENSO signal variance (cf. Figs. 5.2 j-l and Figs. 5.3 j-l).

Where is this relatively strong non-ENSO signal coming from? Considering how the largest amplitude of the non-ENSO signal variance, besides the Ctrl experiment, can be found in the experiment with SST anomalies prescribed in the entire tropical zone (Figs. 5.3 m-o), closely followed by the TroPac experiment (Figs. 5.3 j-l), this suggests that the prevailing non-ENSO signal is still connected to the tropical Pacific, but is not connected to ENSO events as they were defined for the composite analysis. Therefore, this non-ENSO signal variance could be a result of the residual from ENSO events below the compositing threshold ($0.5\sigma < I < 1\sigma$ or $-1\sigma < I < -0.5\sigma$), which were not considered by the current ENSO composite.

Appendix C3 shows the Northern Hemisphere signal variance in January, February and March. Overall, the non-ENSO signal variance is weaker than both ENSO and signal for all years. The non-ENSO signal variance is the strongest in the Ctrl experiment. This non-ENSO composite is mostly weak ($\geq 200 \; m^2$) outside of the Pacific North American region in the rest of the ICTP AGCM experiments.

The North Atlantic maximum is the main spatial characteristic of the signal variance, and it is found in all composites. The monopole is found even in the climatological ICTP AGCM experiment, which is considered to be a numerical residual, as discussed in the previous chapter. Therefore, this monopole shape of the signal variance seems to be a preferred mode of climate variability over the NAE region. The introduction of SST boundary forcing (e.g., ENSO) seems to strengthen this North Atlantic monopole (cf. Fig. 5.2 and 5.3). Therefore, we examine the monthly signal variance averaged over the North Atlantic maximum. Also, some authors argue that a similar case occurs in the PNA region (e.g., Bladé 1999; Molteni et al. 1993), where the remote SST forcing strengthens a natural mode of atmospheric variability. Thus, the NAE average of the signal variance will be compared to the average over the PNA region in the following subsection.

5.4. Spatial average of the signal variance

Here, the GH200 signal variance is averaged over the North Atlantic maximum (NAE max; 40°-60° N, 50°-10° W), which is the most prominent feature of the NAE signal (Figs. 5.1-3), and is simultaneously averaged over the whole available period, ENSO and non-ENSO years (Fig. 5.4). The amplitude of the signal for all years (Fig. 5.4a) is the highest in the late winter months

(January-March). The amplitude starts decreasing until June, when we have a local signal variance maximum, and immediately after the minimum in July. The amplitude increases from August until December when the signal variance reaches values comparable to the late-winter months. The spatially averaged signal variance in ENSO years (Fig. 5.4b) has higher values for all experiments in February, which is indicated by the ratio of the ENSO and the signal variance for all years shown above each column. The largest increase in the ENSO signal variance compared to the signal variance for the whole period is found in March for the TroPac experiment. A significant increase in the TroPac signal variance was also recorded in June, indicating the presence of the delayed influence of ENSO events on the NAE region (Herceg-Bulić et al. 2017). Meanwhile, the non-ENSO signal variance (Fig. 5.4c) is comparable in amplitude to the signal variance for all years (Fig. 5.4a), indicated by the ratio of the non-ENSO signal variance and the signal variance for all years displayed above each column.

Examining the Northern Hemisphere maps (Appendix C1-C3) singled out the Pacific-North American region (PNA) as an area with the highest values of signal variance. Following Chapman et al. (2021), the GH200 signal variance is averaged over the maximum in the PNA region (30°-60° N, 165° E-130° W) and shown in Fig. 5.5. This PNA maximum signal variance has a clear seasonal behaviour, with the highest values in winter, which decrease in amplitude through spring and summer. Overall, the signal variance for all years (Fig. 5.5a) is the strongest in the experiment with globally prescribed SST anomalies. On the other hand, the TroAtl experiment is consistently weakest across all months compared to the rest of the AGCM experiments. The amplitude of the signal variance in TroPac and Tropics experiments is smaller than the Ctrl amplitude but mutually comparable. The ENSO signal variance averaged over the PNA region has similar characteristics – winter maximum and minimum from July through October (Fig. 5.5b). However, the difference between the high winter and lower late summer/early autumn values of the signal is more pronounced in ENSO years than for all years (cf. Fig. 5.5 a and b). Simultaneously, the non-ENSO signal variance (Fig. 5.5c) is generally smaller than the signal variance in all years and ENSO years, and the differences between their amplitude in summer and winter are not as pronounced.

Generally, averaging the signal variance over the NAE maximum yields smaller values than averaging over the PNA maximum. However, even though the NAE signal variance is noticeably weaker than the PNA signal variance. In both regions, the increase of the ENSO signal variance compared to the signal variance for all years is the most pronounced in the TroPac experiment in January-March.

(a) NAE max signal for all years
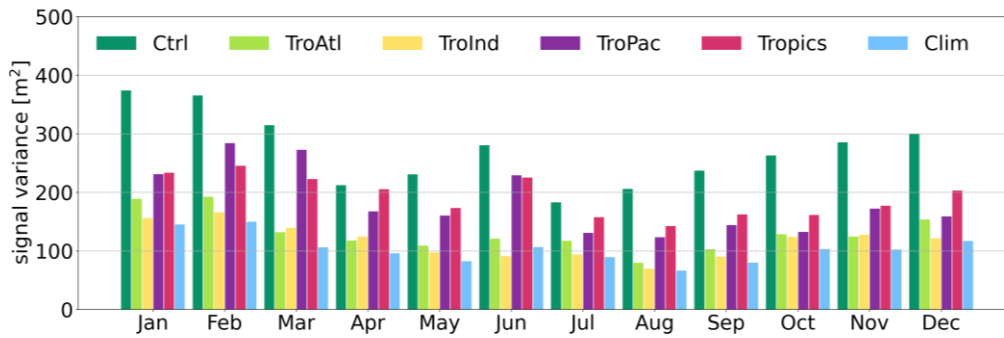
(b) NAE max signal for ENSO years
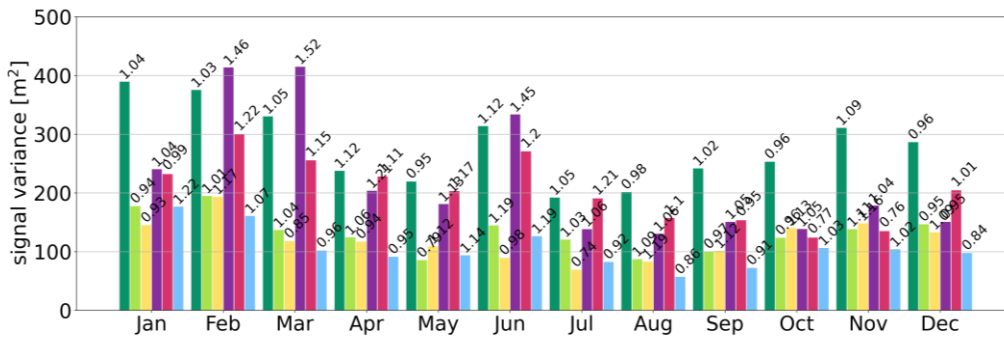
(c) NAE max signal for non-ENSO years
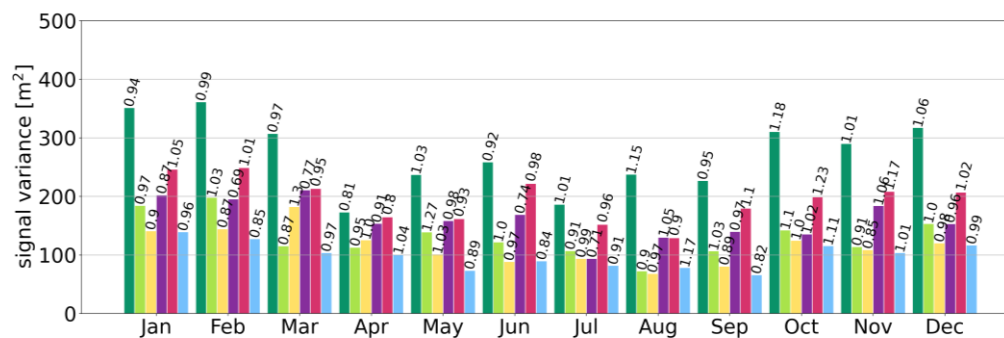
Figure 5.4 Monthly signal variance of geopotential heights at 200 hPa [m^2] averaged over the maximum in the North Atlantic (NAE max; 40°-60° N, 50°-10° W) and over (a) all years (156; 1855-2010), (b) ENSO-years (53), and (c) non-ENSO years (57) in the ICTP AGCM experiments: Ctrl (green), TroAtl (light green), TroInd (yellow), TroPac (purple), Tropics (magenta), and Clim (light blue), respectively. The number above each column is the ratio of the (non) ENSO signal variance and signal variance for all years.

(a) PNA max signal for all years
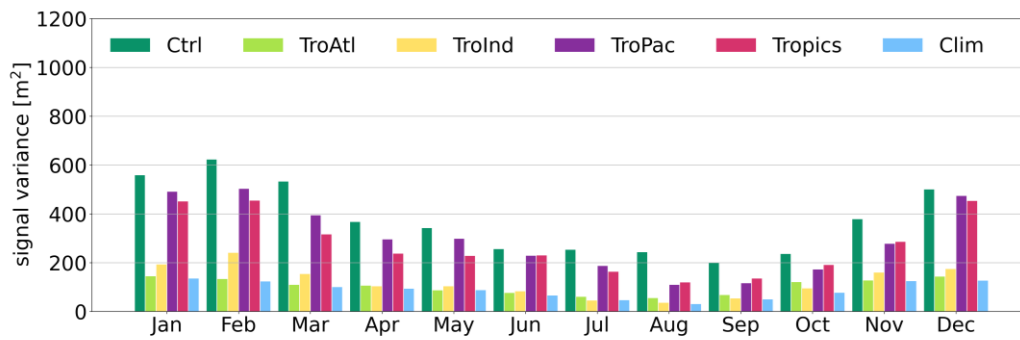
(b) PNA max signal for ENSO years
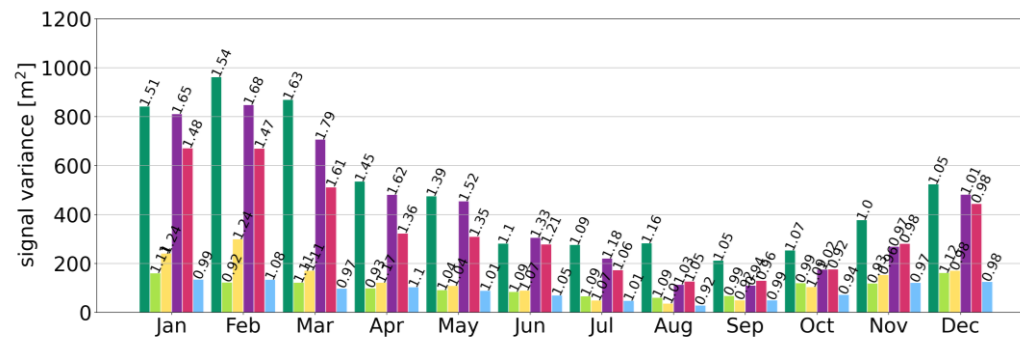
(c) PNA max signal for non-ENSO years
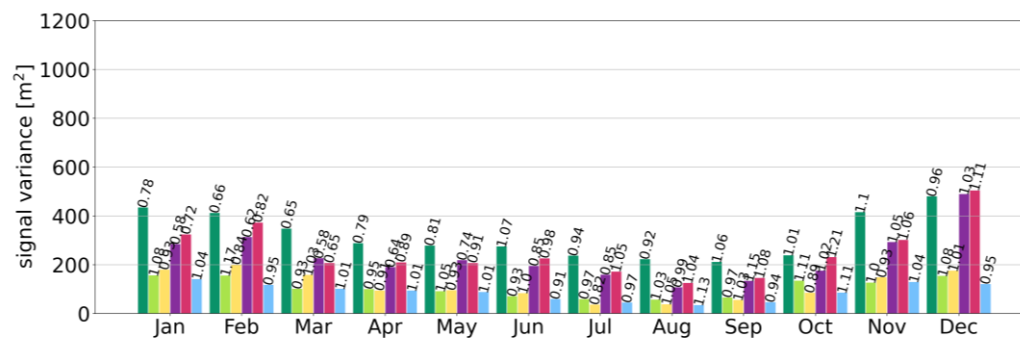
Figure 5.5 Monthly signal variance of geopotential heights at 200 hPa [m^2] averaged over the maximum in the Pacific North American region (30°-60° N, 165° E-130° W) and over (a) all years (156; 1855-2010), (b) ENSO-years (53), and (c) non-ENSO years (57) in the ICTP AGCM experiments: Ctrl (green), TroAtl (light green), TroInd (yellow), TroPac (purple), Tropics (magenta), and Clim (light blue), respectively. The number above each column is the ratio of the (non) ENSO signal variance and signal variance for all years.

6. Impact of warmer climate conditions on the atmospheric variability of the NAE area

The previous two chapters explored the impact of differently set up boundary forcing in the ICTP AGCM experiments on the predictable components and variability of the seasonal atmospheric circulation over the North Atlantic-European area. In this chapter, results from an ICTP AGCM experiment with a double concentration of carbon dioxide and globally prescribed lower-boundary forcing in the form of monthly varying sea surface temperature anomalies are presented to test the impact of warmer climate conditions on the predictable components and variability of the late-winter atmospheric circulation in the NAE area. All results are compared with the control ICTP AGCM experiment.

6.1. Experimental setup

The ICTP AGCM experiment with double carbon dioxide concentration compared to the average CO_2 concentration for 1961-1990 (hereafter 2xCO2) has the same setup as the experiment from Herceg-Bulić et al. (2012). In this experiment, the direct effect of the CO_2 concentration increase on the warming of the atmosphere was simulated by doubling the absorption coefficient in the CO_2 band within the model's radiation parametrisation scheme (ABLCO2). On the other hand, the indirect effect in which the increase of CO_2 affects the atmosphere is through changes in the lower boundary conditions. Therefore, the 2xCO2 contains modified SST climatology and sea-ice concentration input files, which reflect the warmer climate conditions (i.e., the sea-ice concentration is reduced, and the SST climatological values are increased compared to the Ctrl experiment). Also, the 2xCO2 experiment has globally prescribed SST anomalies, with the same interannual variability as the SST anomalies in the Ctrl experiment.

The ICTP AGCM output was linearly detrended and treated with a high-pass filter with a cut-off period of 11 years to remove the possible influence of long-term trends.

6.2. EOF and optimal signal-to-noise patterns

To test the role of the higher radiation forcing in the numerical model on the GH200 variability in the late-winter season, the EOFs are presented first. Figures 6.1 a and b show the first EOF pattern calculated for all simulations within the Ctrl and 2xCO2 ICTP AGCM experiments. Both EOF1 patterns are dominantly dipolar, with two centres between the northeastern part of North America and Greenland and over the North Atlantic. The first centre has a greater amplitude in the 2xCO2 but a noticeably larger percentage of the explained variance in the Ctrl experiment (33% vs 24.5%). The EOF1 mode based on the ensemble means (Fig. 6.1 c and d) have a different spatial structure, with a pronounced centre over the North Atlantic (50° N, 30° W) and a smaller centre of the same sign in the south-eastern part of the NAE domain. The rest of the NAE region contains values of the opposite sign, which are connected in both experiments. Both EOF1 modes explain between 26% and 27.4% of GH200 variability in the JFM season.

(a) All Members EOF1 Ctrl (ExpVar 33.3%) (b) All Members EOF1 2xCO2 (ExpVar 24.5%)

(c) Ensemble Mean EOF1 Ctrl (ExpVar 27.4%) (d) Ensemble Mean EOF1 2xCO2 (ExpVar 26.0%)
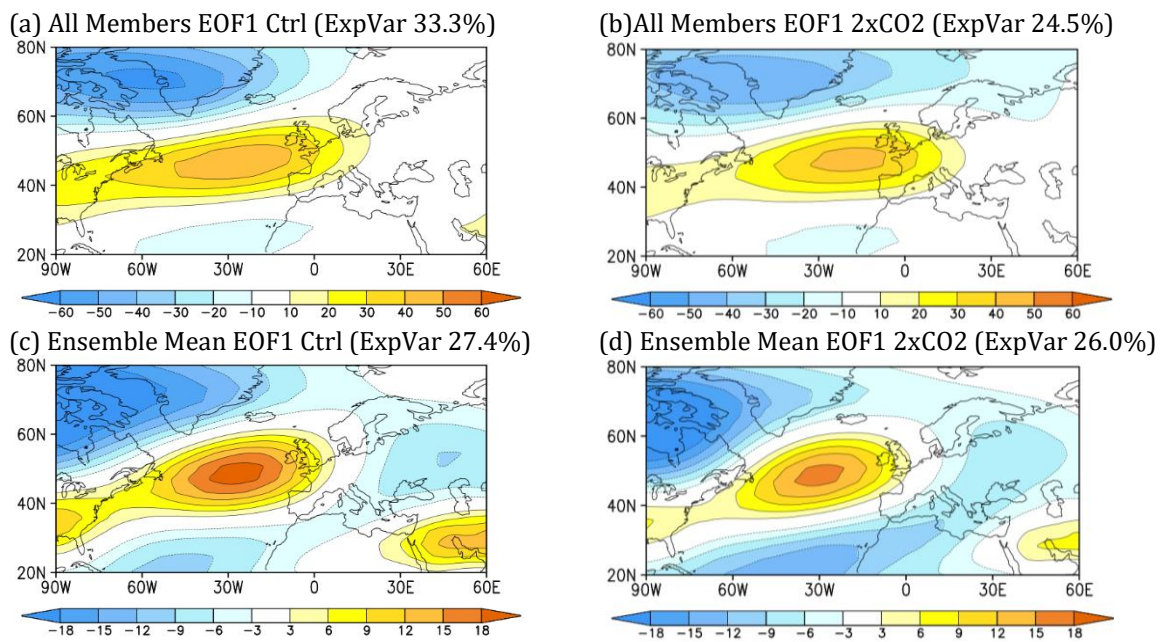
Figure 6.1 EOF1 pattern of JFM geopotential heights at 200 hPa (GH200) [m] based on all ensemble members (a-b) and based on the ensemble mean (c-d) in the period 1855-2010 in the ICTP AGCM experiments Ctrl and 2xCO2. The percentage of explained variance (ExpVar) associated with each EOF pattern is indicated by the number in brackets.

The second EOF mode is shown in Fig. 6.2. The EOF2 pattern based on all ensemble members resembles the East Atlantic pattern, and its spatial characteristics are not affected by the change in CO_2 parametrisation. The amount of explained variance is slightly higher in the 2xCO2 experiment. The ensemble-mean EOF2 mode has an additional centre east of North America, which has higher values and percentage of explained GH200 variance in the 2xCO2 experiment.

(a) All Members EOF2 Ctrl (ExpVar 16.1%)   (b) All Members EOF2 2xCO2 (ExpVar 18.5%)

(c) Ensemble Mean EOF2 Ctrl (ExpVar 16.1%)   (d) Ensemble Mean EOF2 2xCO2 (ExpVar 18.6%)
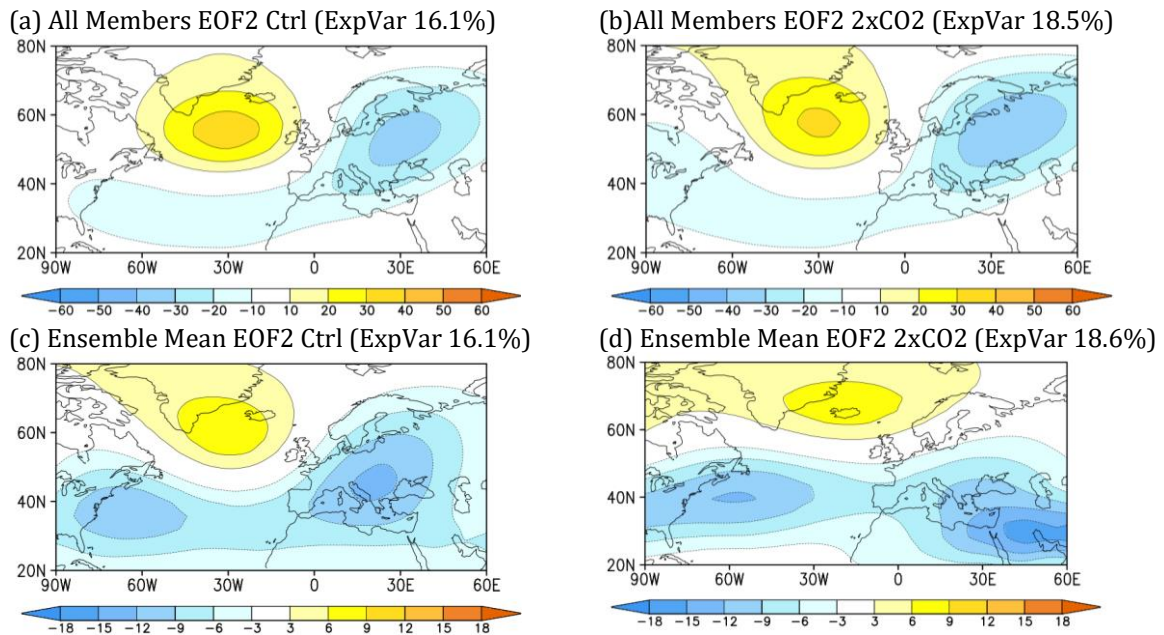
Figure 6.2 EOF2 pattern of JFM geopotential heights at 200 hPa (GH200) [m] based on all ensemble members (a-b) and based on the ensemble mean (c-d) in the period 1855-2010 in the ICTP AGCM experiments Ctrl and 2xCO2. The percentage of explained variance (ExpVar) associated with each EOF pattern is indicated by the number in brackets.

The impact of the warmer climate conditions on the predictable components of the JFM GH200 is tested by employing the signal-to-noise optimal patterns method. This method seeks to find a hierarchy of modes ordered by their signal-to-noise ratio (Fig. 6.3). At first glance, the 2xCO2 EOFOPT1 pattern has a more pronounced and amplified centre over the North Atlantic and the area of the opposite sign directly below the North Atlantic maximum. However, the signal-to-noise ratio of the first optimal pattern is not significantly different in the two ICTP AGCM experiments indicating that the excess radiation forcing does not impact the modelled potential predictability. Also, there is only a slight increase in the optimized signal-to-noise ratio (SNR) in the 2xCO2 compared to the Ctrl experiment. Therefore, based on the presented results, we do not expect a significantly increased potential predictability of the late-winter GH200 for warmer climate conditions in the ICTP AGCM simulations.

(a) JFM EOFOPT1 GH200 Ctrl (SNR 1.95)   (b) JFM EOFOPT1 GH200 2xCO2 (SNR 2.07)
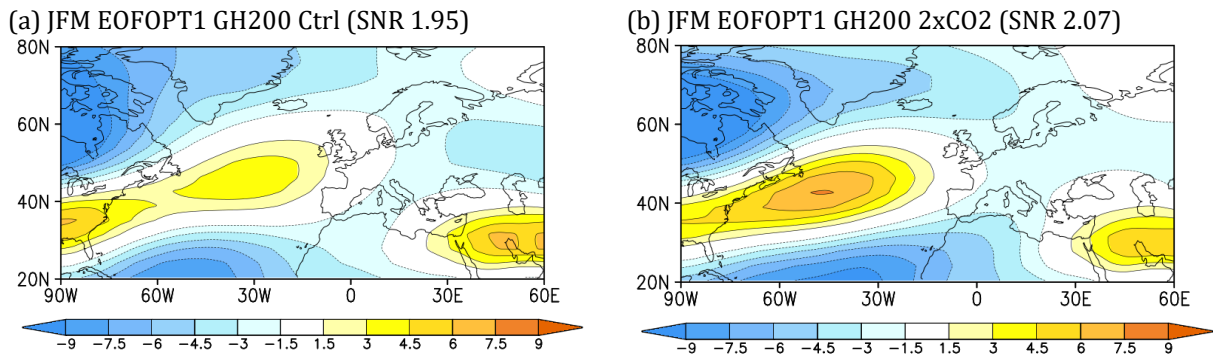
Figure 6.3 First spatial pattern (EOFOPT1) of JFM geopotential heights at 200 hPa [m] in the signal-to-noise optimal patterns method in the period 1855-2010 for the ICTP AGCM experiments (a) Ctrl and (b) 2xCO2. The number in brackets indicates the corresponding signal-to-noise ratio (SNR). Both SNR values are considered statistically significant according to the F test for the ratio of variances on the 95% confidence level.

First optimal patterns for the Ctrl and 2xCO2 experiments are spatially similar (Fig. 6.3). Simultaneously, the correlation between their associated time series (PCAVG1) is very high (0.97). Since the ensemble-mean EOF1 modes in both experiments resemble the first optimal pattern, the correlation between their principal components (PC1) was also calculated. The correlation between the PC1 based on the ensemble mean is equal to 0.71, which is smaller than the correlation between the first optimal pattern time series, but it is still statistically significant based on the two-tailed Student's t-test on the 95% confidence level. For comparison of the ensemble-mean PC1 and PCAVG1 in the Ctrl and 2xCO2 experiments, their correlation is presented in Table 6.1. The correlation coefficients for both experiments are statistically significant, but the correlation is 19.7% higher for the 2xCO2 experiment. The stronger 2xCO2 correlation suggests that warmer climate conditions improve the temporal connection between the patterns that explain the largest part of GH200 variability and the pattern with the optimized signal-to-noise ratio.

Table 6.1 Correlation between the first principal component (PC1) of geopotential heights at 200 hPa (GH200) calculated for the ensemble mean (EnsMean) of each experiment and the time series associated with the first optimal pattern (PCAVG1) of GH200 in JFM season in the 1855-2010 period for Ctrl and 2xCO2 experiments. All values are statistically significant based on the two-tailed Student's t-test at the 95% confidence level.

exp	Ctrl	2xCO2
corr (PC1 EnsMean, PCAVG1)	**0.66**	**0.79**

6.3. Signal variance

The late-winter GH200 signal variance is presented in Fig. 6.4. In the fourth chapter, the signal variance over the NAE region had a spatial pattern similar to the EOF1 mode based on the ensemble mean and the first optimal pattern. The similarity also exists in the Ctrl and 2xCO2 experiments (cf. Figs. 6.4, 6.1 c-d, and 6.3). The centre over the North Atlantic has a more pronounced shape and amplitude in the Ctrl experiment in January and March, but the general spatial characteristics of both patterns are similar. The 2xCO2 signal variance in March (Fig. 6.3f) no longer has the characteristic monopolar shape. The maximum values of the signal variance are not centred but form a zone between 40°-50° N and 50° W-10° E. Note that the signal variance has been plotted over a smaller area than the EOFs and optimal patterns in this chapter (30°-60° N, 50° W-30° E vs 20°-80° N, 90° W-60° E) to enable the comparison with the results from the fifth chapter.

Following the methodology from the previous chapter, the signal variance was calculated for ENSO and non-ENSO composites where the (non)ENSO years were selected according to the value of the standardized JFM Niño3.4 index based on the NOAA ERSST V3 SST anomalies. The ENSO signal variance (Fig. 6.5) is stronger in the 2xCO2 experiment in February and March, pointing towards the increase of the signal connected to ENSO events in warmer climate conditions. Spatial characteristics are similar to the signal variance for all years (Fig. 6.4). In March (Fig. 6.5 c and f), the North Atlantic maximum is shifted in the southwest direction compared to January and February.

(a) Jan signal variance Ctrl   (b) Feb signal variance Ctrl   (c) Mar signal variance Ctrl

(d) Jan signal variance 2xCO2   (e) Feb signal variance 2xCO2   (f) Mar signal variance 2xCO2
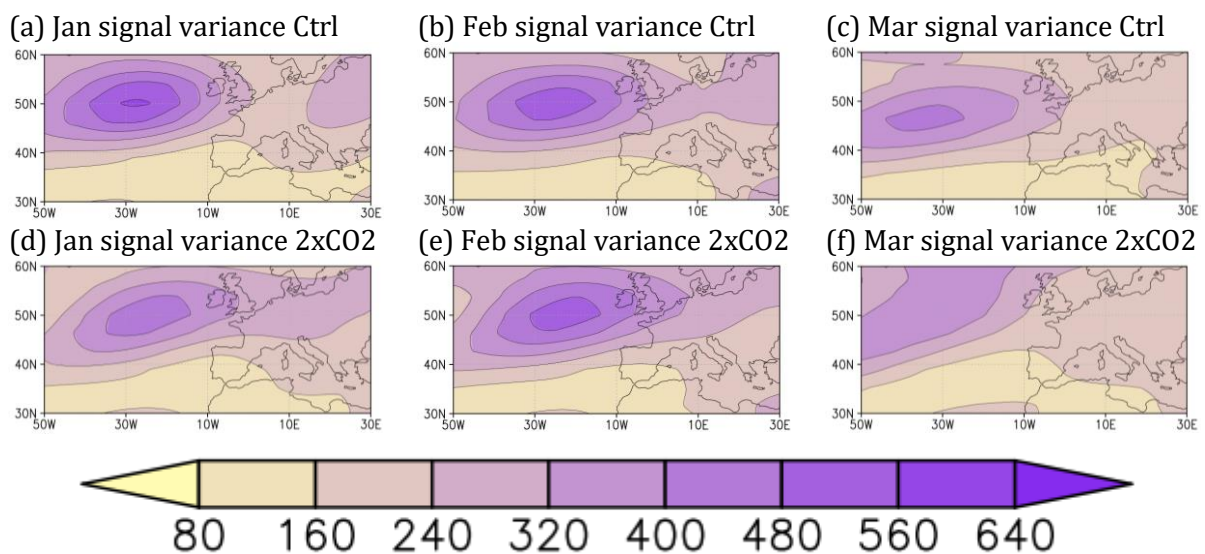
Figure 6.4 Signal variance of geopotential heights at 200 hPa (GH200) [m^2] in January (left), February (middle), and March (right) in the North Atlantic-European region (30°-60° N, 50° W-30° E) for the whole 156-year period (1855-2010) in the Ctrl and 2xCO2 ICTP AGCM experiments.
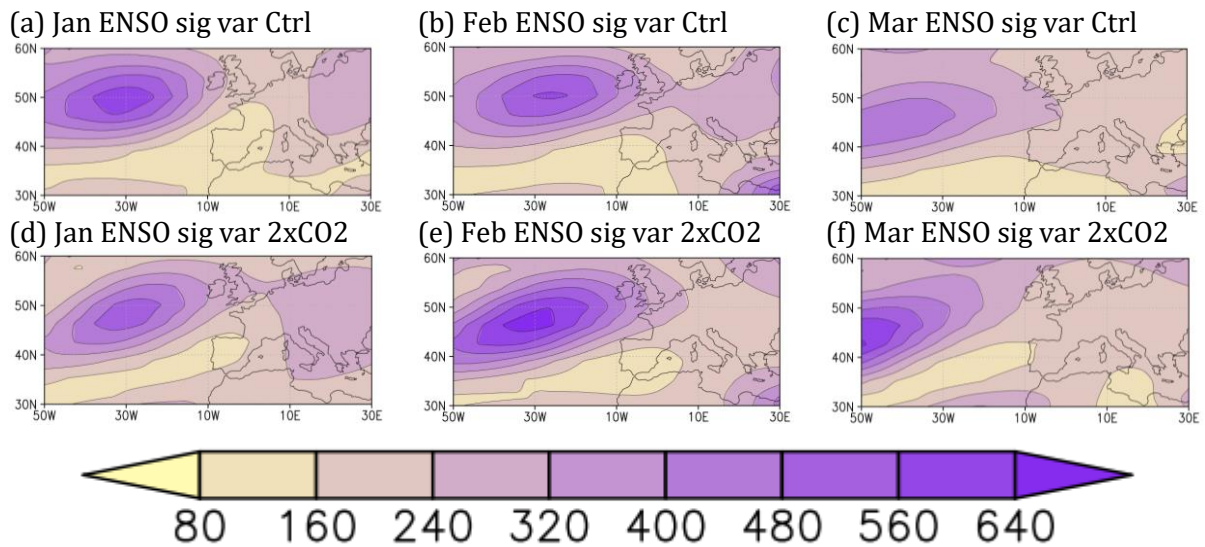
Figure 6.5 Signal variance (sig var) of geopotential heights at 200 hPa (GH200) [m^2] in the 53 ENSO years in January (left), February (middle), and March (right) in the North Atlantic-European region (30°-60° N, 50° W-30° E) in the Ctrl and 2xCO2 ICTP AGCM experiments. The ENSO years were selected from the 156 years according to the strength of the Niño3.4 index in the JFM season.
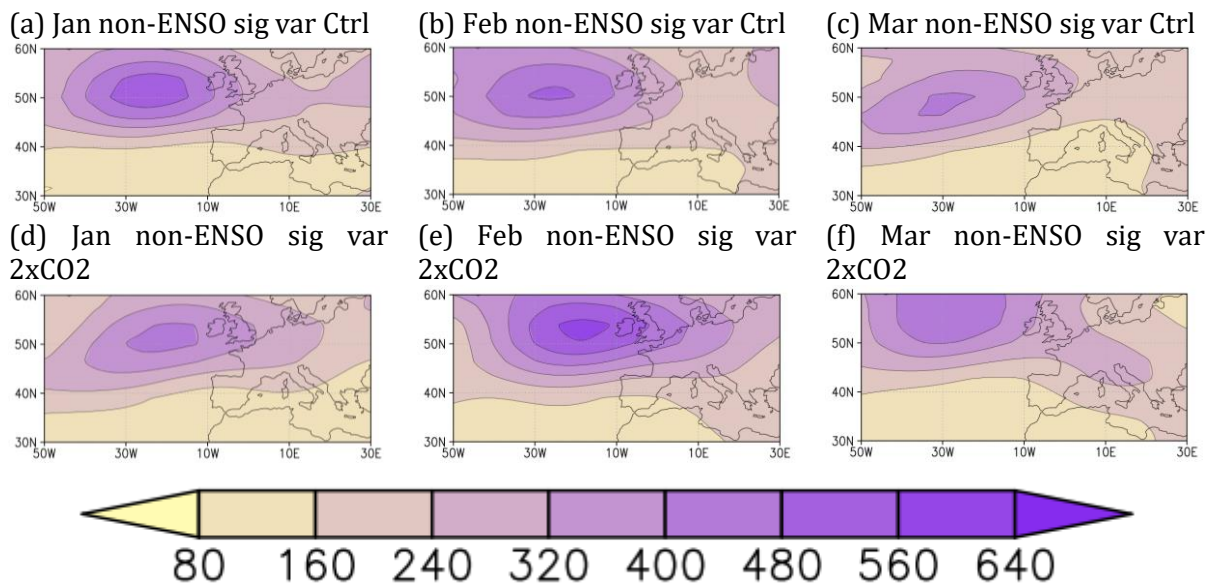
Figure 6.6 Signal variance (sig var) of geopotential heights at 200 hPa (GH200) [m^2] in the 57 non-ENSO years in January (left), February (middle), and March (right) in the North Atlantic-European region (30°-60° N, 50° W-30° E) in the Ctrl and 2xCO2 ICTP AGCM experiments. The non-ENSO years were selected from the 156 years according to the strength of the Niño3.4 index in the JFM season.

The non-ENSO composite is shown in Fig. 6.6. In agreement with the results from the fifth chapter, the non-ENSO signal variance retains the monopole pattern, suggesting it is a mode of GH200 variability which exists unrelated to the presence of the SST boundary forcing. The maximum non-ENSO signal variance is also more pronounced in February and expanded in March in the 2xCO2 experiment (cf. Figs. 6.6 b and e; c and f), which was found in the ENSO

composite as well (cf. Figs. 6.5 b and e; c and f). For completeness, the Northern Hemisphere signal variance for all three composites can be found in Appendix D.

6.4. Correlation between GH200 and lower-boundary forcing

The correlation of the time series connected to the first optimal pattern with the global SST anomalies (Fig. 6.7) is almost identical in the Ctrl and 2xCO2 experiments. The correlation has the highest values in the tropical Pacific, followed by the tropical Indian Ocean and then the tropical Atlantic. The result suggests that the doubling of the CO_2 absorptivity coefficient in the radiation parametrization does not affect the correlation of the pattern with the optimal signal-to-noise ratio with the observed SST anomalies. The correlation maps show a link between the global SST anomalies and temporal variability of the first optimal pattern, which does not take into account any information about the SST boundary forcing or radiation forcing with its calculation.

(a) corr (Ctrl PCAVG1, SSTA) (b) corr (2xCO2 PCAVG1, SSTA)
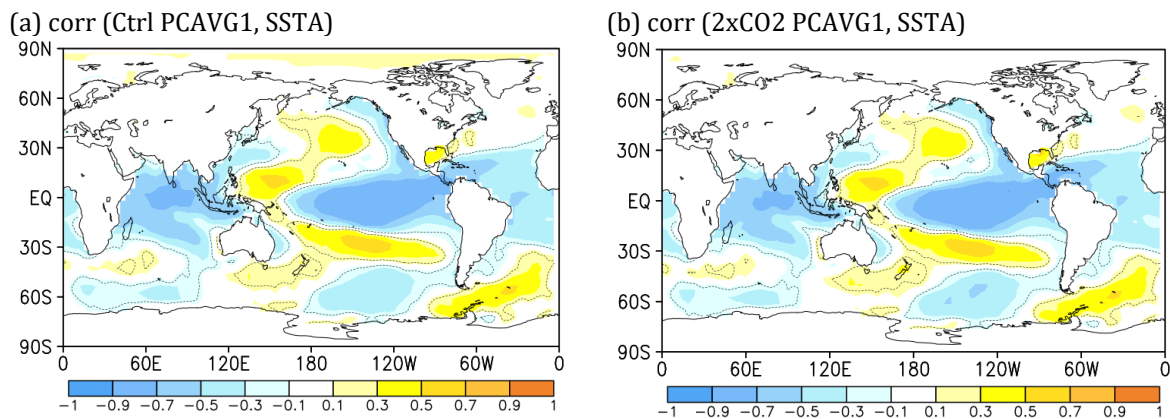
Figure 6.7 Correlation of global NOAA SST anomalies (SSTA) and the time series associated with the first optimal pattern (PCAVG1) of JFM geopotential heights at 200 hPa (GH200) in the period 1855-2010 for ICTP AGCM experiments (a) Ctrl and (b) 2xCO2. All statistically significant values based on the two-tailed Student's *t*-test at the 95% confidence level are encircled by dashed contours.

The connection between the variability of the observed SST anomalies and the time series of the first optimal pattern is presented in Table 6.2. The EOF analysis was applied to the observed SST anomalies in the following areas: TroAtl (30° S-30° N, 100° W-20° E), TroPac (30° S-30° N, 120° E-60° W), TroInd (30° S-30° N, 30° E-120° E), and Tropics (30° S-30° N, 0° E-360° E). The EOF analysis is set up identically for Tables 6.2 and 6.3. The correlation coefficients in the Ctrl and 2xCO2 ICTP AGCM experiments are similar for all SST anomalies, while the biggest difference is found for the PC1 of SST anomalies from the tropical Indian Ocean.

Since the first optimal pattern is similar to the ensemble mean EOF1, the same approach was applied to the PC1 of geopotential heights at 200 hPa from the two ICTP AGCM experiments

(Table 6.3). The correlation coefficients between the PC1 of the observed SST anomalies and PC1 of the modelled GH200 are consistently smaller than those presented in Table 6.2. The biggest difference in correlation is also found in the case of the SST anomalies from the tropical Pacific, where the 2xCO2 has a higher correlation to TroInd SST anomalies than the Ctrl experiment. Furthermore, Table 6.3 shows that all correlations are higher in the case of the 2xCO2 experiment, pointing towards the strengthening of the link between the variability of the SST anomalies and GH200 in warmer climate conditions in the JFM season. In Tables 6.2 and 6.3, the most noticeable difference between the Ctrl and 2xCO2 is connected to the tropical Indian Ocean, which seems to significantly influence the NAE region, especially in the early winter season. The discrepancy tied to the results for the tropical Indian Ocean was already discussed in chapter five and could be a possible reason behind these differences in the correlations between the two ensembles of numerical simulations.

Table 6.2 Correlation between the first principal component (PC1) of NOAA sea surface temperature anomalies (SSTA) and the time series associated with the first optimal pattern (PCAVG1) of geopotential heights at 200 hPa (GH200) in the JFM season in the 1855-2010 period for Ctrl and 2xCO2 ICTP AGCM experiments. All values are statistically significant based on the two-tailed Student's t-test at the 95% confidence level.

	TroAtl SSTA PC1	TroPac SSTA PC1	TroInd SSTA PC1	Tropics SSTA PC1
Ctrl GH200 PCAVG1	**0.81**	**0.88**	**0.81**	**0.91**
2xCO2 GH200 PCAVG1	**0.80**	**0.89**	**0.77**	**0.92**

Table 6.3 Correlation between the first principal component (PC1) of NOAA sea surface temperature anomalies (SSTA) and the first principal component (PC1) of geopotential heights at 200 hPa (GH200) in JFM season in the 1855-2010 period calculated for the ensemble mean (EnsMean) of each experiment for Ctrl and 2xCO2 ICTP AGCM experiments. All values are statistically significant based on the two-tailed Student's t-test at the 95% confidence level.

	TroAtl SSTA PC1	TroPac SSTA PC1	TroInd SSTA PC1	Tropics SSTA PC1
Ctrl GH200 PC1 EnsMean	**0.55**	**0.70**	**0.47**	**0.69**
2xCO2 GH200 PC1 EnsMean	**0.64**	**0.78**	**0.62**	**0.79**

7. Conclusions

The research presented in this thesis was motivated by a number of open questions concerning the effects of teleconnections on the climate variability of the North Atlantic-European area. One of the main objectives was to test the impact of remote influences, such as the El Niño-Southern Oscillation, on the predictable components of the NAE seasonal atmospheric circulation. Besides the influence of lower-boundary forcing on the sub-seasonal to seasonal characteristics of the atmospheric circulation over the NAE region, the impact of warmer climate conditions on the variability and predictable components was examined as well.

7.1. Modulation of the ENSO-NAE teleconnection

The state of the ENSO teleconnection to the North Atlantic-European region (Chapter 3) was investigated using different approaches (probability distribution of the NAO phases during a particular ENSO phase, running correlation, regression maps) and different datasets (HadSLP and NOAA-CIRES-DOE 20th Century Reanalysis). A weakening in the ENSO-NAE teleconnection during the late-winter season was demonstrated. The additional composite analysis confirmed the spatial pattern and the observed changes of the HadSLP regressions on the HadISST Niño3.4 index. Also, the investigation of the HadSLP composites for El Niño and La Niña phases suggested that the observed weakening of the ENSO-NAE teleconnection is mainly tied to the weakening of the El Niño-negative NAO connection. This decrease in the SLP response is also visible in the composites for La Niña. However, because of the generally weaker response to the La Niña phase in the NAE area in the considered period, the observed weakening of the ENSO-NAE teleconnection can be primarily ascribed to the El Niño phase.

The ENSO response in the NAE area has turned from a surface pressure spatial distribution resembling the negative NAO to statistically non-significant values. The weakening of the signal is found at the surface (SLP) and at higher levels (e.g., geopotential height, temperature, zonal wind). The correlation between the Niño3.4 and NAO index and the regression maps indicate that the change began to develop around the 1970s, coinciding with the Northern Hemisphere climate shift.

To offer a possible reason behind the described change, we have further investigated the potential role of sea-ice concentration and SST climatology in modulating the ENSO-NAE teleconnection. ICTP AGCM has been forced with El Niño SSTs in the tropical Pacific for that purpose. Sensitivity experiments with different combinations of sea-ice concentration and SST climatology of 'low' (or 'high') sea-ice concentration and 'early' (or 'late') SST conditions enabled the investigation of their roles. The results indicate that both the sea-ice concentration and SST climatology modulate the ENSO teleconnection over the NAE region. However, their contributions have opposite effects: the Arctic sea-ice loss tends to strengthen the teleconnection, with anomalies resembling an NAO pattern, while it is weakened under the more recent SST climatology. According to the targeted simulations, the recent change in the SST climatology in the Atlantic and Arctic is of great importance for the weakening of the ENSO-NAE teleconnection.

7.2. Late-winter atmospheric variability and predictable components

Numerical simulations made with an intermediately complex AGCM (ICTP AGCM) were designed to detect and examine the potential impact of tropical SSTs on the variability and predictable components of 200-hPa geopotential height over the North Atlantic-European area in the late-winter season (Chapter 4). In total, six model experiments containing observed SST anomalies in different areas of the ocean acting as a form of lower-boundary forcing were conducted.

Results of the EOF analysis showed that the EOF modes based on the ensemble mean, which express the externally forced response, have different spatial characteristics than their counterparts calculated using all individual ensemble members, which are strongly influenced by the internal climate variability. The ensemble-mean EOF1 patterns in the SST-forced experiments resemble the spatial pattern of the signal variance and project onto the pattern with the largest signal-to-noise ratio and project onto the pattern. The similarity between these patterns confirms that the ensemble mean reflects the forced signal (Frankcombe et al. 2018). On the other hand, when all individual ensemble members are considered in the EOF calculation, SST forcing does not change the spatial distributions of the first two EOF modes.

The leading ensemble-mean EOF mode is connected to the signal. This link was expected since the averaging over the ensemble members brings out the forced component of the signal. Simultaneously, temporal variability of the first optimal pattern of GH200 in the JFM season is significantly correlated to the SST anomalies in the tropical Atlantic, tropical Pacific, and tropical Indian Ocean in all of the boundary-forced ICTP AGCM experiments. This correlation shows the

importance of SST forcing in the tropical zone of the Atlantic, Pacific and Indian Oceans for optimizing the signal-to-noise ratio of GH200 in late winter.

Relatively high correlations between the first principal component of NOAA SST anomalies in different ocean basins (representing temporal variability of the dominant mode of SST forcing) and principal components of GH200 (representing temporal variability of the EOF modes), as well as the time series of the first optimal pattern (representing the temporal variability of the pattern with the maximum signal-to-noise ratio), further confirm the connection between remote SSTs and the potential predictability of the GH200 over the NAE region in late winter. Additionally, correlation maps showed that if the SST forcing were applied only in one basin, the influence of the boundary forcing on the predictable components would be relatively straightforward.

In conclusion, the tropical Pacific SST forcing, in particular, is shown to be an essential factor of GH200 variability over the NAE region. Furthermore, the forced signal can be recognized in the ensemble-mean EOF1 pattern projecting onto the first optimal pattern (pattern with the maximal signal-to-noise ratio), indicating its potential predictability.

7.3. Monthly signal variance

The investigation of the monthly signal variance of geopotential heights at 200 hPa over the North Atlantic-European region was based on the results from six idealized ICTP AGCM experiments with differently prescribed SST anomalies, acting as a source of lower boundary forcing (Chapter 5). Results of the control experiment forced with global SST anomalies have shown that the NAE signal has a distinctive centre of action above the North Atlantic. The North Atlantic maximum expands if only ENSO years are considered. However, this spatial pattern of the signal variance also persists in the non-ENSO years but is less pronounced. The greatest difference between the ENSO and non-ENSO signals is found in the experiment with the lower boundary forcing in the tropical Pacific. The signal variance in all three considered composites differs from the classical dipolar pattern of the North Atlantic Oscillation, which dominates the late-winter variability over the NAE region. Since the characteristic monopolar spatial pattern of the signal variance over the NAE area also appears in the climatological experiment, i.e., the ensemble of simulations without any prescribed boundary forcing, it can be considered as an internal mode of the JFM GH200 variability. This mode of variability is strengthened in the presence of the SST boundary forcing from the tropical Pacific in years when ENSO is active.

Comparing the signal variance averaged over the North Atlantic maximum, and the maximum in the Pacific-North American region gives an overview of the month-to-month behaviour of signal variance in the two pronounced centres of action in the Northern Hemisphere. Overall, the PNA maximum amplitude is greater and has a more pronounced difference between the values of signal variance in the ENSO and non-ENSO composites. In the NAE maximum average, there is a delayed ENSO influence with a peak in June. However, the signal variance is generally the largest in the late-winter months, the same as for the PNA maximum average.

7.4. Warmer climate conditions

A comparison between the ICTP AGCM experiment with double carbon dioxide concentration to the control ensemble of simulations was made to test the impact of the warmer climate conditions on the variability and predictable components of the late-winter geopotential heights at 200 hPa over the North Atlantic-European region (Chapter 6). The comparison was made between the 2xCO2 and Ctrl experiments, which both have global SST anomalies imposed as the lower boundary forcing of the atmospheric component of the numerical model.

Results have shown that the first EOF patterns, calculated both for the ensemble mean and all ensemble members, are not significantly impacted by the warmer climate conditions imposed in the 2xCO2 experiment. However, the 2xCO2 percentage of the explained variance of the EOF1 is smaller than in the Ctrl experiment. The same is true for the shape of the EOF2 patterns, except the percentage of the explained variance is higher for the 2xCO2 experiment. In the case of the first optimal signal-to-noise pattern, the 2xCO2 simulations have a stronger North Atlantic maximum and display a higher degree of agreement between the ensemble mean PC1 and the time series of the optimal pattern. The signal-to-noise ratio is not significantly changed in warmer climate conditions.

The late-winter GH200 signal variance has a similar monopolar shape when calculated for all years, and both the ENSO and non-ENSO composite agree with the results from the fourth chapter. When only ENSO years are considered, the February and March signal variance is stronger in the 2xCO2 experiment, suggesting an increasing role of the ENSO on potential predictability in warmer climate conditions. Nevertheless, considering the intermediate complexity and relatively coarse horizontal resolution of the ICTP AGCM, this result should be further critically examined.

Examining the connection with the observed SST anomalies, the correlations between the PC1 of SST anomalies in various tropical ocean areas and the time series of the first optimal pattern for

GH200 are consistently high and significant. The correlations between the PC1 of SST anomalies and the PC1 of the ensemble mean GH200 are somewhat smaller but statistically significant. In both cases, the biggest difference in the correlation for the 2xCO2 and Ctrl experiments is obtained for SST anomalies from the tropical Indian Ocean.

7.5. Future outlooks

Based on the results presented in this thesis, certain new research avenues present themselves. Besides the impact of sea-ice concentration and SST climatology on the observed change in the late-winter ENSO-NAE teleconnection (Chapter 3), there are other possible influences on this teleconnection. For example, taking into consideration the delayed ENSO influence on the NAE region via the stratosphere (e.g., Herceg-Bulić et al. 2017) and the difference between the late-fall, early, and late-winter atmospheric response to ENSO (Ayarzagüena et al. 2018; King et al. 2018; Abid et al. 2020) provide the base for future studies of the ENSO-NAE teleconnection. Also, a multi-model study of the impact of the two previously selected mechanisms on the modulation of the ENSO-NAE teleconnection could be beneficial for understanding model biases in this particular area.

The effect of tropical oceans on the variability of atmospheric circulation over the North Atlantic-European area was stressed (Chapters 4 and 5). The contribution of the tropical oceans to the externally forced signals over the NAE region should also be investigated in other (sub)seasons, possibly employing high-resolution GCMs and other analysis methods (e.g., machine learning algorithms such as self-organizing maps).

The effect of warmer climate conditions on the NAE atmospheric circulation and its potential predictability in the late-winter season was investigated (Chapter 6). In continuation of this research, the impact of the increasing greenhouse gas concentration in various socio-economic scenarios on, for example, the duration and intensity of heat waves could be investigated by designing new ICTP AGCM simulations.

Bibliography

Abid MA, Kucharski F, Molteni F, et al (2020) Separating the Indian and Pacific Ocean impacts on the Euro-Atlantic response to ENSO and its transition from early to late winter. J Clim 1–57. https://doi.org/10.1175/jcli-d-20-0075.1

Alexander MA, Bladé I, Newman M, et al (2002) The Atmospheric Bridge: The Influence of ENSO Teleconnections on Air–Sea Interaction over the Global Oceans. J Clim 15:2205–2231. https://doi.org/10.1175/1520-0442(2002)015<2205:TABTIO>2.0.CO;2

Allan R, Ansell T (2006) A New Globally Complete Monthly Historical Gridded Mean Sea Level Pressure Dataset (HadSLP2): 1850–2004. J Clim 19:5816–5842. https://doi.org/10.1175/JCLI3937.1

Ayarzagüena B, Ineson S, Dunstone NJ, et al (2018) Intraseasonal effects of El Niño-Southern Oscillation on North Atlantic climate. J Clim 31:8861–8873. https://doi.org/10.1175/JCLI-D-18-0097.1

Bader J, Latif M (2003) The impact of decadal-scale Indian Ocean sea surface temperature anomalies on Sahelian rainfall and the North Atlantic Oscillation. Geophys Res Lett 30:. https://doi.org/10.1029/2003GL018426

Bader J, Latif M (2005) North Atlantic oscillation response to anomalous Indian ocean SST in a coupled GCM. J Clim 18:. https://doi.org/10.1175/JCLI3577.1

Barnett TP, Latif M, Kirk E, Roeckner E (1991) On ENSO Physics. J Clim 4:487–515. https://doi.org/10.1175/1520-0442(1991)004<0487:oep>2.0.co;2

Barnston AG, Livezey RE (1987) Classification, seasonality and persistence of low-frequency atmospheric circulation patterns. Mon Weather Rev 115:1083–1126. https://doi.org/10.1175/1520-0493(1987)115<1083:CSAPOL>2.0.CO;2

Behera SK (2020) Tropical and Extratropical Air-Sea Interactions: Modes of Climate Variations

Bell CJ, Gray LJ, Charlton-Perez AJ, et al (2009) Stratospheric communication of El Niño teleconnections to European winter. J Clim 22:4083–4096. https://doi.org/10.1175/2009JCLI2717.1

Bjerknes J (1969) Atmospheric Teleconnections from the Equatorial Pacific. Mon Weather Rev 97:163–172. https://doi.org/10.1175/1520-0493(1969)097<0163:atftep>2.3.co;2

Bladé I (1999) The influence of midlatitude ocean-atmosphere coupling on the low-frequency variability of a GCM. Part II: Interannual variability induced by tropical SST forcing. J Clim 12:. https://doi.org/10.1175/1520-0442-12.1.21

Bourke W (1974) A Multi-Level Spectral Model. I. Formulation and Hemispheric Integrations. Mon Weather Rev. https://doi.org/10.1175/1520-0493(1974)102<0687:amlsmi>2.0.co;2

Branković Č, Molteni F (2004) Seasonal climate and variability of the ECMWF ERA-40 model. Clim Dyn 22:139–156. https://doi.org/10.1007/s00382-003-0370-0

Branstator G (2002) Circumglobal teleconnections, the jet stream waveguide, and the North Atlantic Oscillation. J Clim 15:1893–1910. https://doi.org/10.1175/1520-0442(2002)015<1893:CTTJSW>2.0.CO;2

Brönnimann S (2007) Impact of El Niño-Southern Oscillation on European climate. Rev Geophys 45:. https://doi.org/10.1029/2006RG000199

Cai W, Santoso A, Collins M, et al (2021) Changing El Niño–Southern Oscillation in a warming climate. Nat Rev Earth Environ 2:628–644. https://doi.org/10.1038/s43017-021-00199-z

Cai W, Santoso A, Wang G, et al (2020) ENSO Response to Greenhouse Forcing. In El Niño Southern Oscillation in a Changing Climate (eds M.J. McPhaden, A. Santoso and W. Cai). In: Geophysical Monograph Series, American Geophysical Union

Cai W, Wu L, Lengaigne M, et al (2019) Pantropical climate interactions. Science (80-) 363:. https://doi.org/10.1126/science.aav4236

Calvo N, Iza M, Hurwitz MM, et al (2017) Northern hemisphere stratospheric pathway of different El Niño flavors in stratosphere-resolving CMIP5 models. J Clim 30:4351–4371. https://doi.org/10.1175/JCLI-D-16-0132.1

Cattiaux J, Peings Y, Saint-Martin D, et al (2016) Sinuosity of midlatitude atmospheric flow in a warming world. Geophys Res Lett. https://doi.org/10.1002/2016GL070309

Chapman WE, Subramanian AC, Xie SP, et al (2021) Monthly modulations of ENSO teleconnections: Implications for potential predictability in North America. J Clim 34:5899–5921. https://doi.org/10.1175/JCLI-D-20-0391.1

Cohen J, Screen JA, Furtado JC, et al (2014) Recent Arctic amplification and extreme mid-latitude

weather. Nat Geosci 7:627–637. https://doi.org/10.1038/ngeo2234

Colfescu I, Schneider EK (2017) Internal atmospheric noise characteristics in twentieth century coupled atmosphere–ocean model simulations. Clim Dyn 49:2205–2217. https://doi.org/10.1007/s00382-016-3440-9

Czaja A, Frankignoul C (2002) Observed impact of Atlantic SST anomalies on the North Atlantic oscillation. J Clim 15:. https://doi.org/10.1175/1520-0442(2002)015<0606:OIOASA>2.0.CO;2

Czaja A, Frankignoul C, Minobe S, Vannière B (2019) Simulating the Midlatitude Atmospheric Circulation: What Might We Gain From High-Resolution Modeling of Air-Sea Interactions? Curr. Clim. Chang. Reports

Di Carlo E, Ruggieri P, Davini P, et al (2022) ENSO teleconnections and atmospheric mean state in idealised simulations. Clim Dyn 1–18

Dogar MM, Kucharski F, Azharuddin S (2017) Study of the global and regional climatic impacts of ENSO magnitude using SPEEDY AGCM. J Earth Syst Sci 126:30. https://doi.org/10.1007/s12040-017-0804-4

Domeisen DIV, Badin G, Koszalka IM (2018) How predictable are the Arctic and North Atlantic Oscillations? Exploring the variability and predictability of the Northern Hemisphere. J Clim 31:997–1014. https://doi.org/10.1175/JCLI-D-17-0226.1

Domeisen DIV, Butler AH, Fröhlich K, et al (2015) Seasonal predictability over Europe arising from El Niño and stratospheric variability in the MPI-ESM seasonal prediction system. J Clim 28:256–271. https://doi.org/10.1175/JCLI-D-14-00207.1

Domeisen DIV, Garfinkel CI, Butler AH (2019) The Teleconnection of El Niño Southern Oscillation to the Stratosphere. Rev Geophys 57:5–47. https://doi.org/10.1029/2018RG000596

Francis JA, Vavrus SJ (2015) Evidence for a wavier jet stream in response to rapid Arctic warming. Environ Res Lett 10:14005. https://doi.org/10.1088/1748-9326/10/1/014005

Frankcombe LM, England MH, Kajtar JB, et al (2018) On the choice of ensemble mean for estimating the forced signal in the presence of internal variability. J Clim 31:5681–5693. https://doi.org/10.1175/JCLI-D-17-0662.1

García-Serrano J, Cassou C, Douville H, et al (2017) Revisiting the ENSO Teleconnection to the

Tropical North Atlantic. J Clim 30:6945–6957. https://doi.org/10.1175/JCLI-D-16-0641.1

Gastineau G, Frankignoul C (2015) Influence of the North Atlantic SST variability on the atmospheric circulation during the twentieth century. J Clim. https://doi.org/10.1175/JCLI-D-14-00424.1

Hardiman SC, Dunstone NJ, Scaife AA, et al (2019) The Impact of Strong El Niño and La Niña Events on the North Atlantic. Geophys Res Lett 46:2874–2883. https://doi.org/10.1029/2018GL081776

Hardiman SC, Dunstone NJ, Scaife AA, et al (2020) Predictability of European winter 2019/20: Indian Ocean dipole impacts on the NAO. Atmos Sci Lett 21:. https://doi.org/10.1002/asl.1005

Held IM, Suarez MJ (1994) A proposal for the intercomparison of the dynamical cores of atmospheric general circulation models. Bull - Am Meteorol Soc 75:1825–1830. https://doi.org/10.1175/1520-0477(1994)075<1825:APFTIO>2.0.CO;2

Herceg-Bulić I, Branković Č (2007) ENSO forcing of the Northern Hemisphere climate in a large ensemble of model simulations based on a very long SST record. Clim Dyn 28:231–254. https://doi.org/10.1007/s00382-006-0181-1

Herceg-Bulić I, Branković Č, Kucharski F (2012) Winter ENSO teleconnections in a warmer climate. Clim Dyn 38:1593–1613. https://doi.org/10.1007/s00382-010-0987-8

Herceg-Bulić I, Kucharski F (2012) Delayed ENSO impact on spring precipitation over North/Atlantic European region. Clim Dyn 38:2593–2612. https://doi.org/10.1007/s00382-011-1151-9

Herceg-Bulić I, Mezzina B, Kucharski F, et al (2017) Wintertime ENSO influence on late spring European climate: the stratospheric response and the role of North Atlantic SST. Int J Climatol 37:87–108. https://doi.org/10.1002/joc.4980

Hoerling MP, Hurrell JW, Xu T (2001) Tropical origins for recent North Atlantic climate change. Science (80-) 292:90–92. https://doi.org/10.1126/science.1058582

Hoerling MP, Hurrell JW, Xu T, et al (2004) Twentieth century North Atlantic climate change. Part II: Understanding the effect of Indian Ocean warming. Clim Dyn 23:391–405. https://doi.org/10.1007/s00382-004-0433-x

Horel JD, Wallace JM (1981) Planetary-scale atmospheric phenomena associated with the

Southern Oscillation. Mon Weather Rev 109:813–829. https://doi.org/10.1175/1520-0493(1981)109<0813:PSAPAW>2.0.CO;2

Hoskins BJ, Ambrizzi T (1993) Rossby wave propagation on a realistic longitudinally varying flow. J Atmos Sci 50:1661–1671. https://doi.org/10.1175/1520-0469(1993)050<1661:RWPOAR>2.0.CO;2

Hoskins BJ, Karoly DJ (1981) The steady linear response of a spherical atmosphere to thermal and orographic forcing. J Atmos Sci 38:1179–1196. https://doi.org/10.1175/1520-0469(1981)038<1179:TSLROA>2.0.CO;2

Hurrell JW (1995) Decadal trends in the North Atlantic oscillation: Regional temperatures and precipitation. Science (80-) 269:. https://doi.org/10.1126/science.269.5224.676

Hurrell JW (1996) Influence of variations in extratropical wintertime teleconnections on Northern Hemisphere temperature. Geophys Res Lett 23:. https://doi.org/10.1029/96GL00459

Hurrell JW, Kushnir Y, Ottersen G, Visbeck M (2003) An overview of the North Atlantic Oscillation. Geophys Monogr Ser 134:1–35. https://doi.org/10.1029/134GM01

Ineson S, Scaife AA (2009) The role of the stratosphere in the European climate response to El Niño. Nat Geosci 2:32–36. https://doi.org/10.1038/ngeo381

Iza M, Calvo N (2015) Role of Stratospheric Sudden Warmings on the response to Central Pacific El Niño. Geophys Res Lett 42:2482–2489. https://doi.org/10.1002/2014GL062935

Jiménez-Esteve B, Domeisen DI V. (2018) The Tropospheric Pathway of the ENSO–North Atlantic Teleconnection. J Clim 31:4563–4584. https://doi.org/10.1175/JCLI-D-17-0716.1

Jin FF (1997) An equatorial ocean recharge paradigm for ENSO. Part I: Conceptual model. J Atmos Sci 54:. https://doi.org/10.1175/1520-0469(1997)054<0811:AEORPF>2.0.CO;2

Joshi MK, Abid MA, Kucharski F (2021) The Role of an Indian Ocean Heating Dipole in the ENSO Teleconnection to the North Atlantic European Region in Early Winter during the Twentieth Century in Reanalysis and CMIP5 Simulations. J Clim 34:1047–1060. https://doi.org/10.1175/JCLI-D-20-0269.1

Jung T, Hilmer M, Ruprecht E, et al (2003) Characteristics of the recent eastward shift of interannual NAO variability. J Clim 16:3371–3382. https://doi.org/10.1175/1520-0442(2003)016<3371:COTRES>2.0.CO;2

King MP, Herceg-Bulić I, Bladé I, et al (2018) Importance of Late Fall ENSO Teleconnection in the Euro-Atlantic Sector. Bull Am Meteorol Soc 99:1337–1343. https://doi.org/10.1175/BAMS-D-17-0020.1

King MP, Li C, Sobolowski S (2021) Resampling of ENSO teleconnections: accounting for cold-season evolution reduces uncertainty in the North Atlantic. Weather Clim Dyn 2:. https://doi.org/10.5194/wcd-2-759-2021

Kingtse CM, Livezey RE (1986) Tropical-extratropical geopotential height teleconnections during the Northern Hemisphere winter. Mon Weather Rev 114:2488–2515. https://doi.org/10.1175/1520-0493(1986)114<2488:teghtd>2.0.co;2

Kodera K, Koide H, Yoshimura H (1999) Northern Hemisphere winter circulation associated with the North Atlantic oscillation and stratospheric polar-night jet. Geophys Res Lett 26:. https://doi.org/10.1029/1999GL900016

Kucharski F, Molteni F, Bracco A (2006a) Decadal interactions between the western tropical Pacific and the North Atlantic Oscillation. Clim Dyn 26:79–91. https://doi.org/10.1007/s00382-005-0085-5

Kucharski F, Molteni F, King MP, et al (2013) On the need of intermediate complexity general circulation models: A "sPEEDY'" example." Bull Am Meteorol Soc 94:25–30. https://doi.org/10.1175/BAMS-D-11-00238.1

Kucharski F, Molteni F, Yoo JH (2006b) SST forcing of decadal Indian Monsoon rainfall variability. Geophys Res Lett 33:. https://doi.org/10.1029/2005GL025371

Kutzbach JE (1967) Empirical Eigenvectors of Sea-Level Pressure, Surface Temperature and Precipitation Complexes over North America. J Appl Meteorol 6:. https://doi.org/10.1175/1520-0450(1967)006<0791:eeoslp>2.0.co;2

Lau NC (1981) A diagnostic study of recurrent meteorological anomalies in a 15 yr simulation with a GFDL general circulation model. Mon Weather Rev 109:2287–2311. https://doi.org/10.1175/1520-0493(1981)109<2287:ADSORM>2.0.CO;2

Li RKK, Woollings T, O'Reilly C, Scaife AA (2020) Effect of the North Pacific Tropospheric Waveguide on the Fidelity of Model El Niño Teleconnections. J Clim 33:5223–5237. https://doi.org/10.1175/jcli-d-19-0156.1

Li Y, Lau NC (2012) Impact of ENSO on the atmospheric variability over the North Atlantic in late Winter-Role of transient eddies. J Clim 25:320–342. https://doi.org/10.1175/JCLI-D-11-

00037.1

Limpasuvan V, Hartmann DL (1999) Eddies and the annular modes of climate variability. Geophys Res Lett 26:3133–3136. https://doi.org/10.1029/1999GL010478

Lin J, Qian T (2019) A New Picture of the Global Impacts of El Nino-Southern Oscillation. Sci Rep. https://doi.org/10.1038/s41598-019-54090-5

Lopez H, Kirtman BP (2019) ENSO influence over the Pacific North American sector: uncertainty due to atmospheric internal variability. Clim Dyn 52:. https://doi.org/10.1007/s00382-018-4500-0

McPhaden MJ, Santoso A, Cai W (2020) Introduction to El Niño Southern Oscillation in a Changing Climate. In: Geophysical Monograph Series

Mezzina B, García-Serrano J, Bladé I, Kucharski F (2020) Dynamics of the ENSO teleconnection and NAO variability in the North Atlantic-European late winter. J Clim 33:907–923. https://doi.org/10.1175/JCLI-D-19-0192.1

Molteni F (2003) Atmospheric simulations using a GCM with simplified physical parametrizations. I: Model climatology and variability in multi-decadal experiments. Clim Dyn 20:175–191. https://doi.org/10.1007/s00382-002-0268-2

Molteni F, Ferranti L, Palmer TN, Viterbo P (1993) A dynamical interpretation of the global response to equatorial Pacific SST anomalies. J Clim 6:. https://doi.org/10.1175/1520-0442(1993)006<0777:ADIOTG>2.0.CO;2

Okumura Y, Xie SP, Numaguti A, Tanimoto Y (2001) Tropical Atlantic air-sea interaction and its influence on the NAO. Geophys Res Lett 28:. https://doi.org/10.1029/2000GL012565

Pinto JG, Raible CC (2012) Past and recent changes in the North Atlantic oscillation. Wiley Interdiscip Rev Clim Chang 3:79–90. https://doi.org/10.1002/wcc.150

Poli P, Hersbach H, Dee DP, et al (2016) ERA-20C: An Atmospheric Reanalysis of the Twentieth Century. J Clim 29:4083–4097. https://doi.org/10.1175/JCLI-D-15-0556.1

Power S, Casey T, Folland C, et al (1999) Inter-decadal modulation of the impact of ENSO on Australia. Clim Dyn 15:319–324. https://doi.org/10.1007/s003820050284

Rayner NA, Parker DE, Horton EB, et al (2003) Global analyses of sea surface temperature, sea ice, and night marine air temperature since the late nineteenth century. J Geophys Res Atmos. https://doi.org/10.1029/2002jd002670

Ren HL, Scaife AA, Dunstone N, et al (2019) Seasonal predictability of winter ENSO types in operational dynamical model predictions. Clim Dyn 52:3869–3890. https://doi.org/10.1007/s00382-018-4366-1

Rodríguez-Fonseca B, Polo I, Serrano E, Castro M (2006) Evaluation of the North Atlantic SST forcing on the European and northern African winter climate. Int J Climatol 26:179–191. https://doi.org/10.1002/joc.1234

Ropelewski CF, Halpert MS (1989) Precipitation Patterns Associated with the High Index Phase of the Southern Oscillation. J Clim 2:268–284. https://doi.org/10.1175/1520-0442(1989)002<0268:ppawth>2.0.co;2

Ropelewski CF, Halpert MS (1986) North American precipitation and temperature patterns associated with the El Nino/Southern Oscillation (ENSO). Mon Weather Rev 114:2352–2362. https://doi.org/10.1175/1520-0493(1986)114<2352:NAPATP>2.0.CO;2

Ruggieri P, Kucharski F, Buizza R, Ambaum MHP (2017) The transient atmospheric response to a reduction of sea-ice cover in the Barents and Kara Seas. Q J R Meteorol Soc 143:1632–1640. https://doi.org/10.1002/qj.3034

Sardeshmukh PD, Hoskins BJ (1988) The generation of global rotational flow by steady idealized tropical divergence. J Atmos Sci 45:1228–1251. https://doi.org/10.1175/1520-0469(1988)045<1228:TGOGRF>2.0.CO;2

Scaife AA, Arribas A, Blockley E, et al (2014) Skillful long-range prediction of European and North American winters. Geophys Res Lett 41:2514–2519. https://doi.org/10.1002/2014GL059637

Scaife AA, Comer RE, Dunstone NJ, et al (2017) Tropical rainfall, Rossby waves and regional winter climate predictions. Q J R Meteorol Soc 143:1–11. https://doi.org/10.1002/qj.2910

Schopf PS, Suarez MJ (1988) Vacillations in a coupled ocean-atmosphere model. J Atmos Sci 45:. https://doi.org/10.1175/1520-0469(1988)045<0549:VIACOM>2.0.CO;2

Screen JA, Deser C, Smith DM, et al (2018) Consistency and discrepancy in the atmospheric response to Arctic sea-ice loss across climate models. Nat Geosci 11:155–163. https://doi.org/10.1038/s41561-018-0059-y

Slivinski LC, Compo GP, Whitaker JS, et al (2019) Towards a more reliable historical reanalysis: Improvements for version 3 of the Twentieth Century Reanalysis system. Q J R Meteorol Soc 145:2876–2908. https://doi.org/10.1002/qj.3598

Smith SR, O'Brien JJ (2001) Regional snowfall distributions associated with ENSO: Implications for seasonal forecasting. Bull Am Meteorol Soc 82:1179–1191. https://doi.org/10.1175/1520-0477(2001)082<1179:RSDAWE>2.3.CO;2

Smith TM, Reynolds RW, Peterson TC, Lawrimore J (2008) Improvements to NOAA's historical merged land-ocean surface temperature analysis (1880-2006). J Clim 21:2283–2296. https://doi.org/10.1175/2007JCLI2100.1

Sterl A, van Oldenborgh GJ, Hazeleger W, Burgers G (2007) On the robustness of ENSO teleconnections. Clim Dyn 29:469–485. https://doi.org/10.1007/s00382-007-0251-z

Straus D, Shukla J, Paolino D, et al (2003) Predictability of the seasonal mean atmospheric circulation during autumn, winter and spring. J Clim. https://doi.org/10.1175/1520-0442(2003)016<3629:POTSMA>2.0.CO;2

Sutton RT, Hodson DLR (2003) Influence of the ocean on North Atlantic climate variability 1871-1999. J Clim 16:3296–3313. https://doi.org/10.1175/1520-0442(2003)016<3296:IOTOON>2.0.CO;2

Taschetto AS, Ummenhofer CC, Stuecker MF, et al (2020) ENSO Atmospheric Teleconnections. In: El Niño Southern Oscillation in a Changing Climate. American Geophysical Union (AGU), pp 309–335

Terray L, Cassou C (2002) Tropical Atlantic sea surface temperature forcing of quasi-decadal climate variability over the North Atlantic-European region. J Clim 15:3170–3187. https://doi.org/10.1175/1520-0442(2002)015<3170:TASSTF>2.0.CO;2

Toniazzo T, Bentsen M, Craig C, et al (2020) Enforcing conservation of axial angular momentum in the atmospheric general circulation model CAM6. Geosci Model Dev 13:. https://doi.org/10.5194/gmd-13-685-2020

Toniazzo T, Scaife AA (2006) The influence of ENSO on winter North Atlantic climate. Geophys Res Lett 33:L24704. https://doi.org/10.1029/2006GL027881

Trenberth KE, Hurrell JW (1994) Decadal atmosphere-ocean variations in the Pacific. Clim Dyn 9:. https://doi.org/10.1007/BF00204745

Vallis GK, Gerber EP, Kushner PJ, Cash BA (2004) A mechanism and simple dynamical model of the North Atlantic Oscillation and annular modes. J Atmos Sci. https://doi.org/10.1175/1520-0469(2004)061<0264:amasdm>2.0.co;2

van Oldenborgh GJ (2005) Comments on "Predictability of winter climate over the North Atlantic European region during ENSO events." J Clim 18:2770–2772. https://doi.org/10.1175/JCLI3441.1

van Oldenborgh GJ, Burgers G (2005) Searching for decadal variations in ENSO precipitation teleconnections. Geophys Res Lett 32:. https://doi.org/10.1029/2005GL023110

van Oldenborgh GJ, Burgers G, Tank AK (2000) On the El Nino teleconnection to spring precipitation in Europe. Int J Climatol 20:565–574. https://doi.org/10.1002/(SICI)1097-0088(200004)20:5<565::AID-JOC488>3.0.CO;2-5

Venzke S, Allen MR, Sutton RT, Rowell DP (1999) The atmospheric response over the North Atlantic to decadal changes in sea surface temperature. J Clim 12:2562–2584. https://doi.org/10.1175/1520-0442(1999)012<2562:tarotn>2.0.co;2

Walsh JE, Chapman WL (2001) 20th-century sea-ice variations from observational data. Ann Glaciol. https://doi.org/10.3189/172756401781818671

Wang B, An SI (2001) Why the properties of El Niño changed during the late 1970s. Geophys Res Lett. https://doi.org/10.1029/2001GL012862

Wang C (2019) Three-ocean interactions and climate variability: a review and perspective. Clim Dyn 53:. https://doi.org/10.1007/s00382-019-04930-x

Wang C, Picaut J (2004) Understanding ENSO physics—a review. In: Geophysical Monograph Series. pp 21–48

Wanner H, Brönnimann S, Casty C, et al (2001) North Atlantic oscillation - Concepts and studies. Surv Geophys 22:321–382. https://doi.org/10.1023/A:1014217317898

Warner JL, Screen JA, Scaife AA (2019) Links between Barents-Kara sea ice and the Extratropical Atmospheric Circulation explained by internal variability and tropical forcing. Geophys Res Lett. https://doi.org/10.1029/2019gl085679

Wettstein JJ, Wallace JM (2010) Observed patterns of month-to-month storm-track variability and their relationship to the background flow. J Atmos Sci 67:1420–1437. https://doi.org/10.1175/2009JAS3194.1

Wilks DS (2019) Hypothesis Testing. In: Statistical Methods in the Atmospheric Sciences. pp 131–177

Woollings T, Franzke C, Hodson DLR, et al (2015) Contrasting interannual and multidecadal NAO

variability. Clim Dyn 45:539–556. https://doi.org/10.1007/s00382-014-2237-y

Zhang W, Mei X, Geng X, et al (2019a) A nonstationary ENSO-NAO relationship due to AMO modulation. J Clim 32:33–43. https://doi.org/10.1175/JCLI-D-18-0365.1

Zhang W, Wang L, Xiang B, et al (2015) Impacts of two types of La Niña on the NAO during boreal winter. Clim Dyn. https://doi.org/10.1007/s00382-014-2155-z

Zhang W, Wang Z, Stuecker MF, et al (2019b) Impact of ENSO longitudinal position on teleconnections to the NAO. Clim Dyn 52:257–274. https://doi.org/10.1007/s00382-018-4135-1

(a) 1909-1938

(b) 1919-1948

(c) 1929-1958

(d) 1939-1968

(e) 1949-1978

(f) 1959-1988

(g) 1969-1998
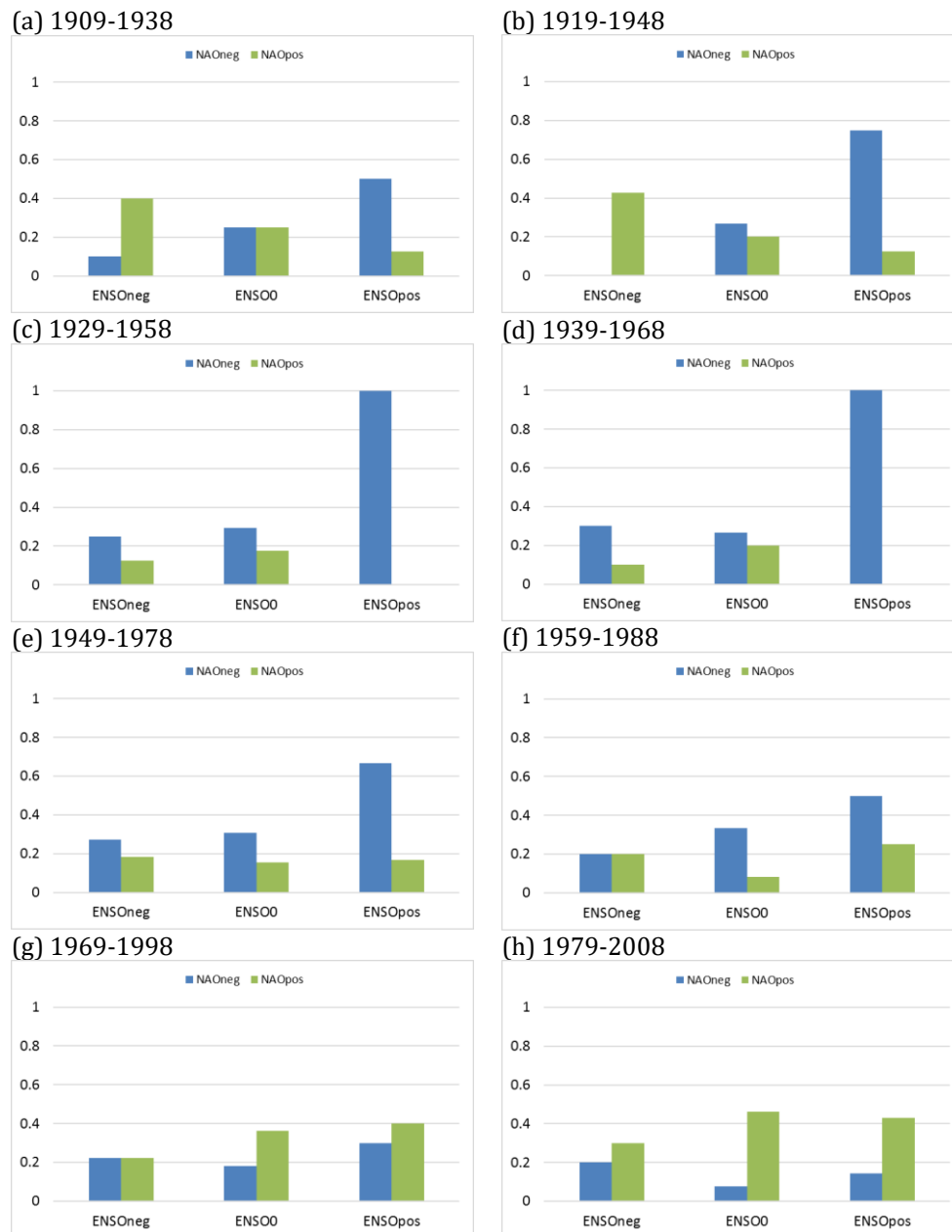
(h) 1979-2008

Appendix Figure A1 Probability distribution of NAO phases during a particular ENSO phase for the ERA-20C reanalysis data for (a) 1909-1938, (b) 1919-1948, (c) 1929-1958, (d) 1939-1968, (e) 1949-1978, (f) 1959-1988, (g) 1969-1998, and (h) 1979-2008. ENSO0 (neutral), ENSOneg (La Niña) and ENSOpos (El Niño) events are defined by the values of the JFM HadISST Niño 3.4 index (ENSO0: $-0.5\sigma \leq I \leq 0.5\sigma$, ENSOneg: $I < -0.5\sigma$, ENSOpos: $I > 0.5\sigma$). An analogous definition is made for NAO events sorted by the value of the JFM NAO index.
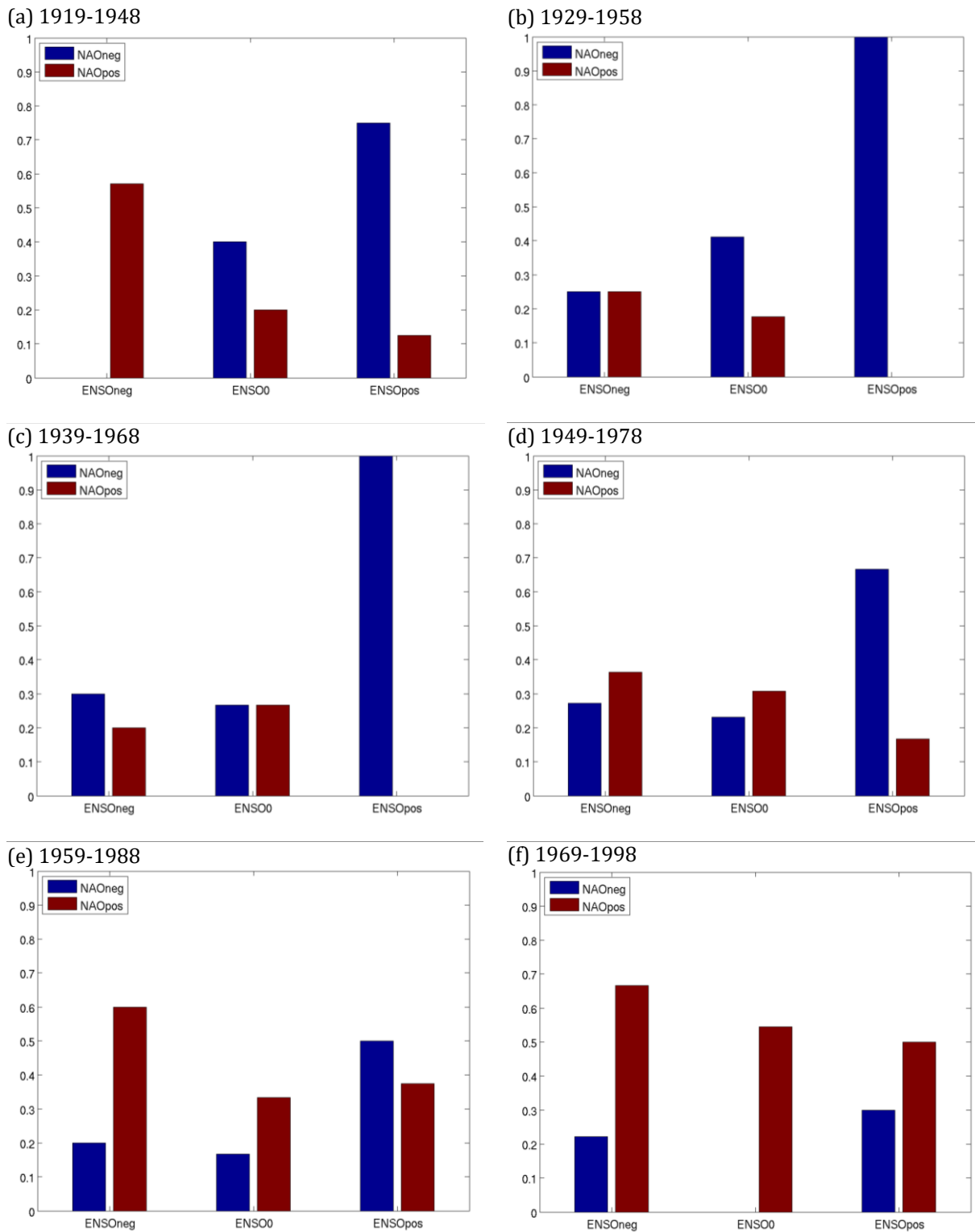
Appendix Figure A2 Probability distribution of NAO phases during a particular ENSO phase for (a) 1919-1948, (b) 1929-1958, (c) 1939-1968, (d) 1949-1978, (e) 1959-1988, and (f) 1969-1998. ENSO0 (neutral), ENSOneg (La Niña) and ENSOpos (El Niño) events are defined by the values of the JFM HadISST Niño 3.4 index (ENSO0: $-0.5\sigma \leq I \leq 0.5\sigma$, ENSOneg: $I < -0.5\sigma$, ENSOpos: $I > 0.5\sigma$). An analogous definition is made for NAO events and NAO index with removed decadal variability (31-year moving average of JFM Hurrell PC-based NAO index subtracted from the standardized JFM Hurrell PC-based NAO index).

(a) regr JFM (Niño 3.4, HadSLP) 1899-2015
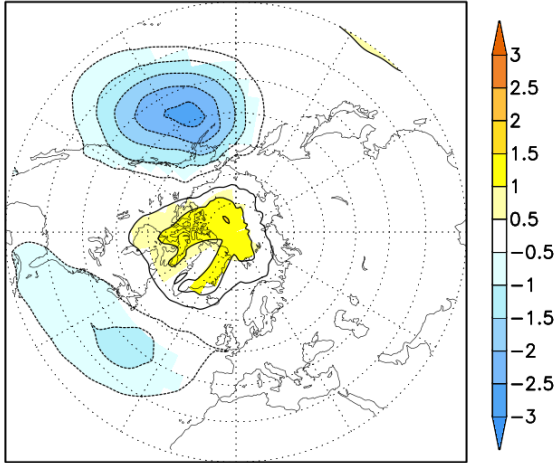
(b) regr JFM (Niño 3.4, HadSLP) 1899-1928
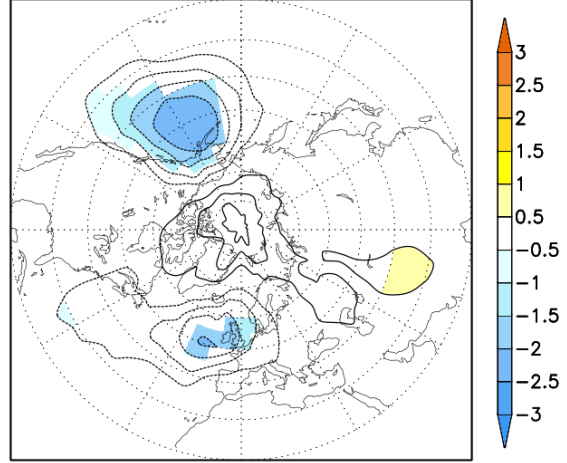
(c) regr JFM (Niño 3.4, HadSLP) 1909-1938
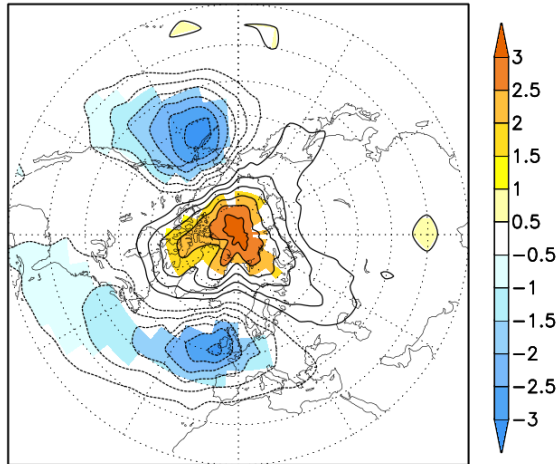
(d) regr JFM (Niño 3.4, HadSLP) 1919-1948
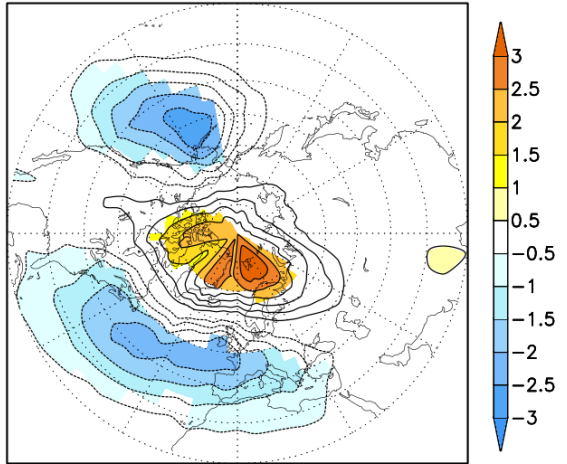
(e) regr JFM (Niño 3.4, HadSLP) 1929-1958
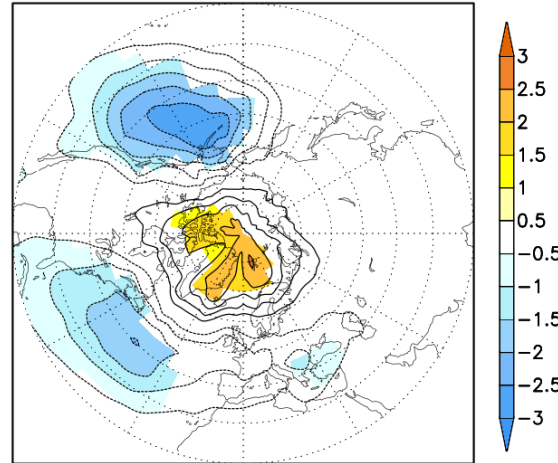
(f) regr JFM (Niño 3.4, HadSLP) 1939-1968
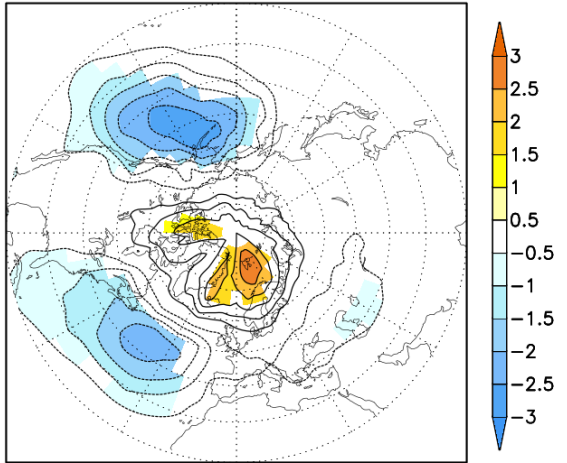
(g) regr JFM (Niño 3.4, HadSLP) 1949-1978
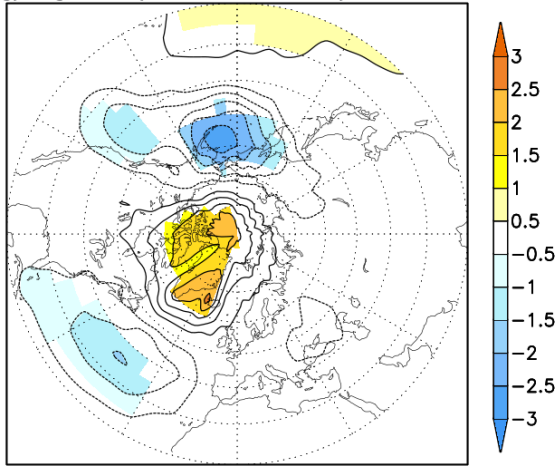
(h) regr JFM (Niño 3.4, HadSLP) 1959-1988
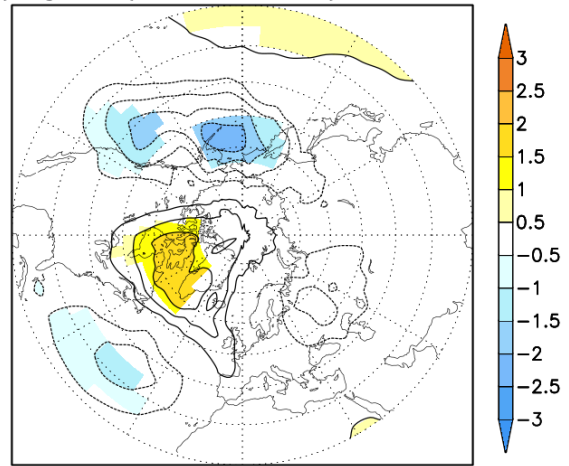
(i) regr JFM (Niño 3.4, HadSLP) 1969-1998
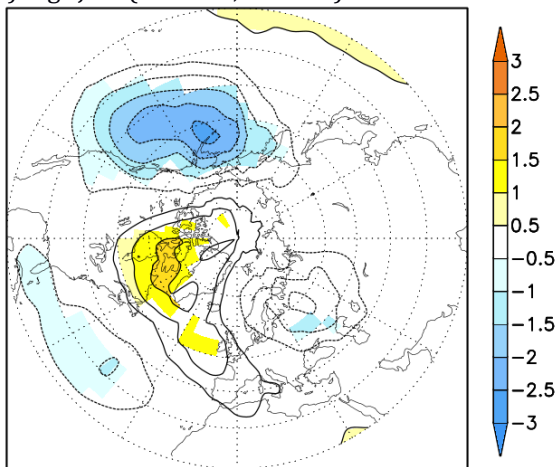
(j) regr JFM (Niño 3.4, HadSLP) 1979-2008
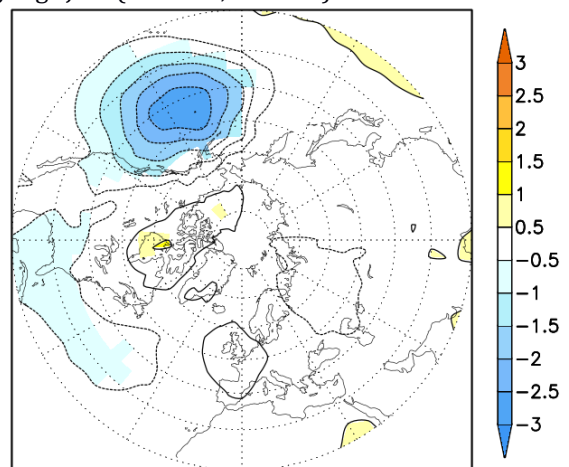
Appendix Figure A3 Regression of JFM HadSLP onto JFM Niño 3.4 index (HadISST) [hPa / °C] for (a) the whole con-sidered period 1899-2015, and (b)-(j) 30-year long sub-periods. Statistically significant results (p < 10%) are shaded.

(a) regr (Niño 3.4, 20CRV3 GH850) 1930-1959
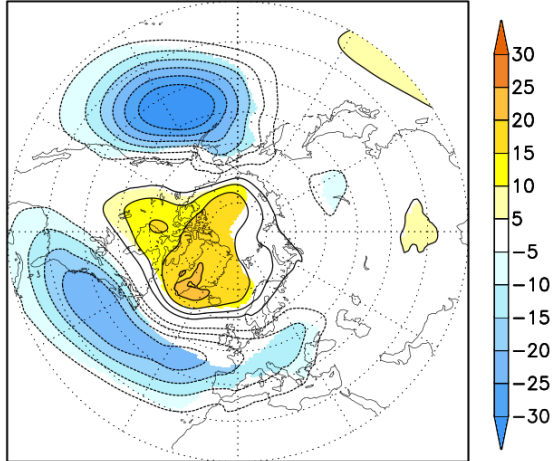
(b) regr (Niño 3.4, 20CRV3 GH850) 1970-1999
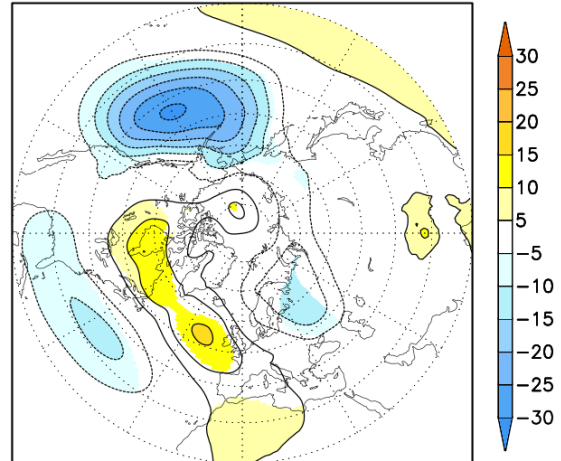
(c) regr (Niño 3.4, 20CRV3 GH500) 1930-1959
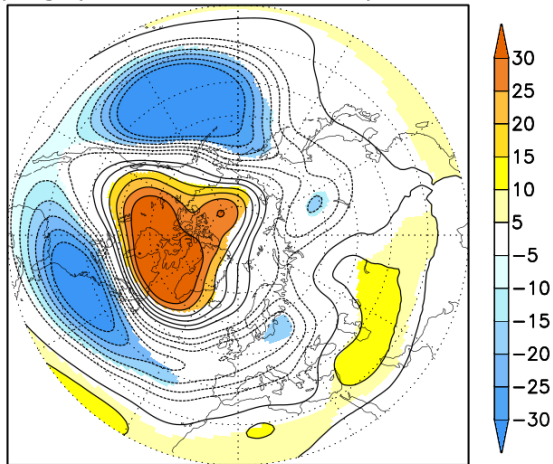
(d) regr (Niño 3.4, 20CRV3 GH500) 1970-1999
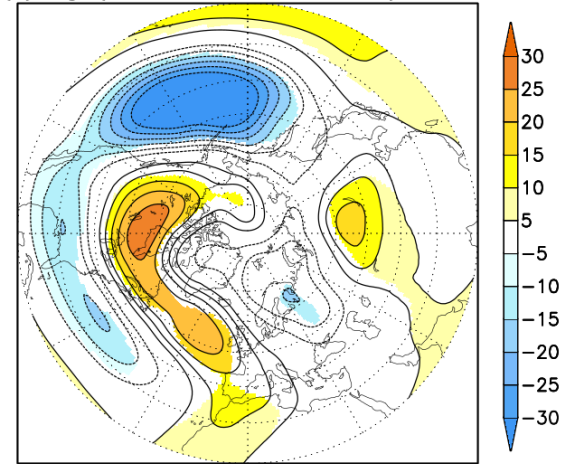
(e) regr (Niño 3.4, 20CRV3 GH200) 1930-1959
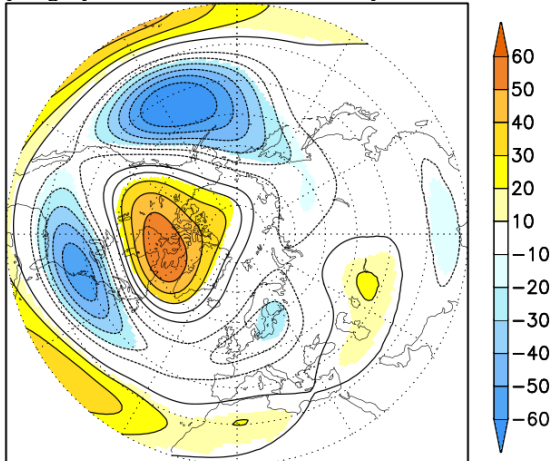
(f) regr (Niño 3.4, 20CRV3 GH200) 1970-1999
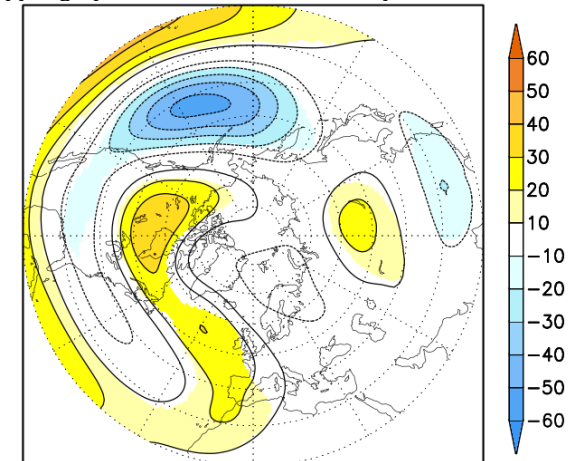
Appendix Figure A4 Regression of the JFM NOAA-CIRES-DOE 20th Century Reanalysis V3 GH850 onto JFM Niño3.4 index (HadISST) [m/ °C] for (a) 1930-1959 and (b) 1970-1999, regression of the JFM GH500 onto JFM Niño3.4 index [m/ °C] for (c) 1930-1959 and (d) 1970-1999 and regression of the JFM GH200 onto JFM Niño3.4 index [m/ °C] for (e) 1930-1959 and (f) 1970-1999. Statistically significant results (p < 10%) are shaded.

(a) u200 ('early' SST clim +'high' SIC) – ('late' SST clim +'low' SIC)
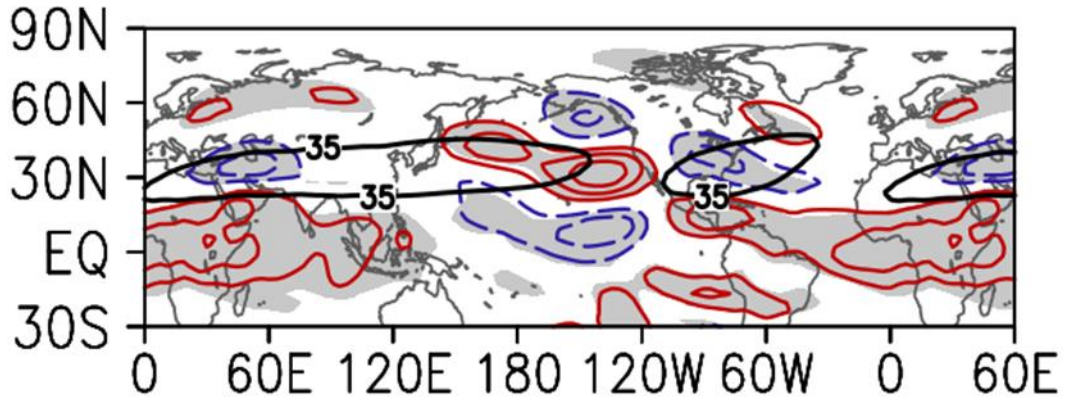
(b) u200 ('early' SST clim +'high' SIC) – ('late' SST clim in ATL & ARC+'low' SIC)
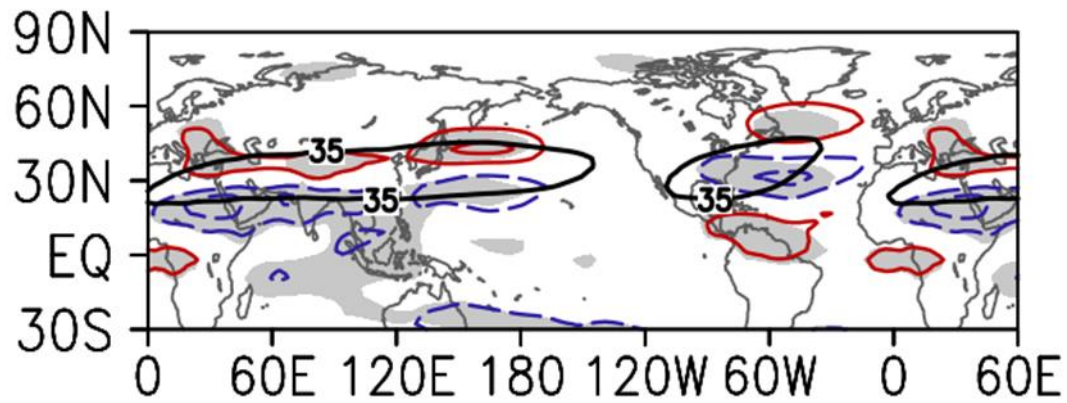
(c) u200 ('early' SST clim in ATL & ARC+'low' SIC) – ('late' SST clim +'low' SIC)
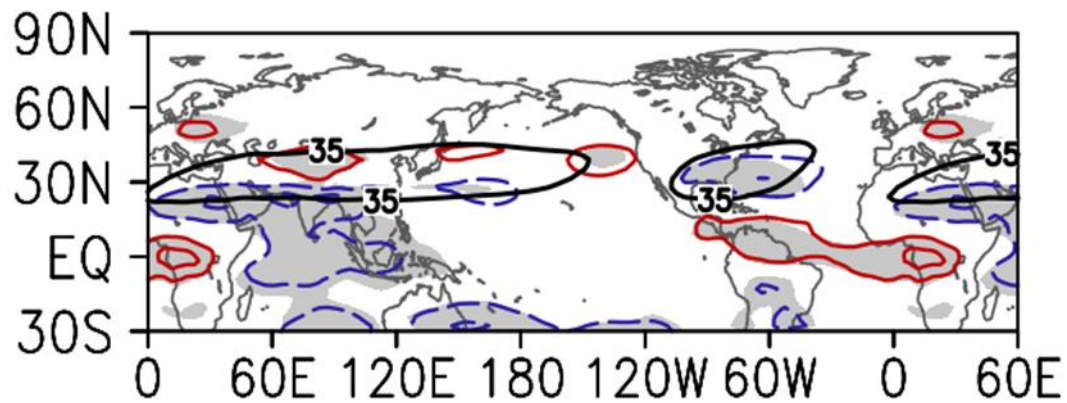
Appendix Figure A5 Changes of background states in the zonal wind on 200 hPa level (u200) shown in colour contours (red – positive values, blue – negative values; contour interval = 1 m/s) in Jan/Feb from three selected control experiments (i.e., without El Niño anomaly forcing) of ICTP AGCM. 'Early' SST climatology and 'high' sea-ice concentration refer to the 1979-1999 period, while the 'late' SST climatology and 'low' sea-ice concentration refer to the 2005-2015 period. The 35 m/s isoline for mean u200 is indicated by the black line, roughly illustrating the cores of jet streams. Grey shading is applied at the 95% two-tail significance level.

(a) 'High' SIC + 'early' SST clim (EM)
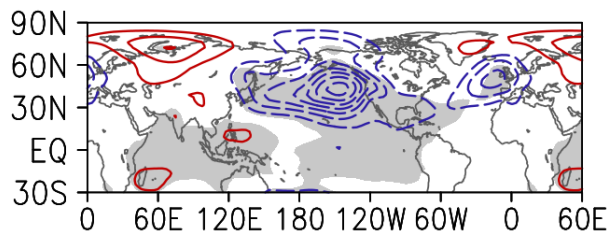
(b) 'Low' SIC + 'late' SST clim (EM)
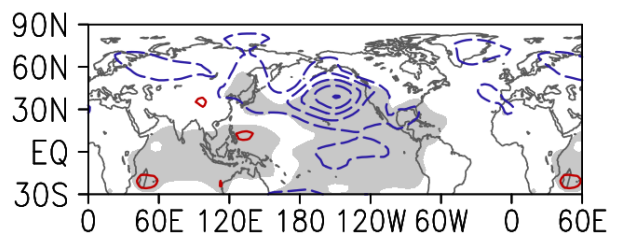
(c) 'Low' SIC + 'early' SST clim (EM)
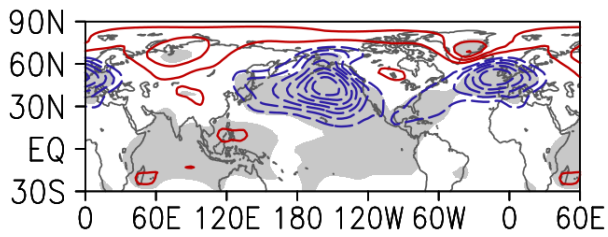
(d) 'High' SIC + 'late' SST clim (EM)
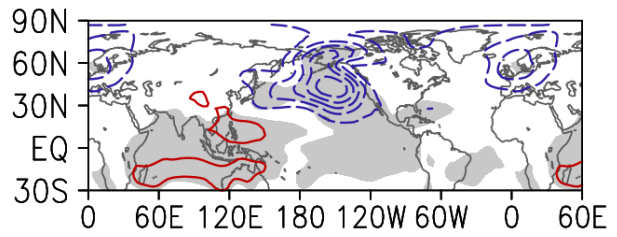
Appendix Figure A6 ICTP AGCM simulated MSLP response to El Niño Modoki (EM) in conditions with (a) 'high' sea-ice concentration and 'early' SST climatology, (b) 'low' sea-ice concentration and 'late' SST climatology, (c) 'low' sea-ice concentration and 'early' SST climatology and (d) 'high' sea-ice concentration and 'late' SST climatology. 'Early' SST climatology and 'high' sea-ice concentration refer to the 1979-1999 period, while the 'late' SST climatology and 'low' sea-ice concentration refer to the 2005-2015 period. The contouring interval is 0.5 hPa. Red contour – positive values, blue contour – negative values. Statistically significant results (p < 5%) are shaded in grey.

Appendix B

(a) JFM EOF1 GH200 (ExpVar 27.5%)   (b) JFM EOF2 GH200 (ExpVar 14.9%)
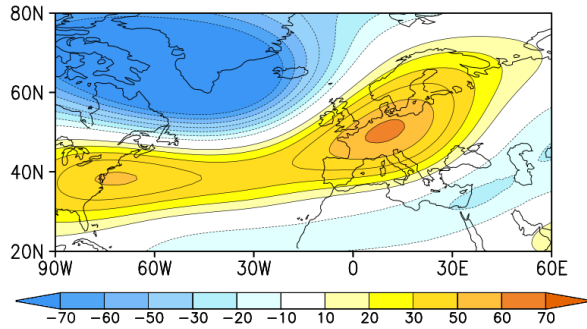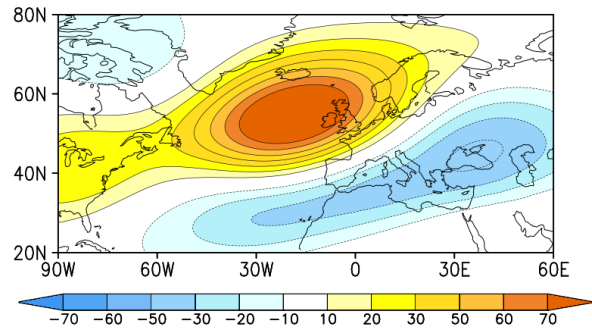
Appendix Figure B1 First and second EOF pattern of JFM geopotential heights at 200 hPa (GH200) [m] in the 1855-2010 period for NOAA-CIRES-DOE 20th Century Reanalysis V3. The percentage of explained variance (ExpVar) for each EOF pattern is shown in brackets.

Appendix C

(a) Jan variance signal Ctrl
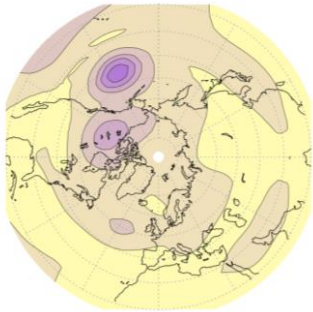
(b) Feb variance signal Ctrl
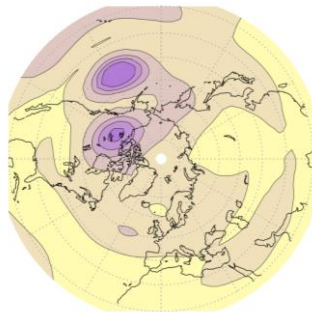
(c) Mar variance signal Ctrl
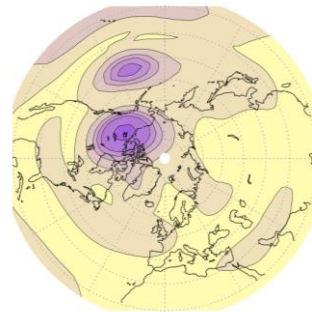
(d) Jan signal variance TroAtl
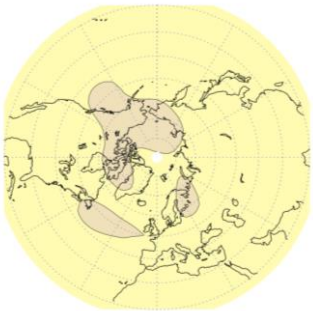
(e) Feb signal variance TroAtl
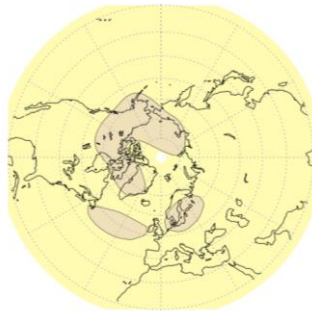
(f) Mar signal variance TroAtl
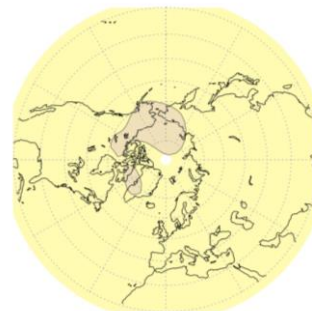
(g) Jan signal variance TroInd
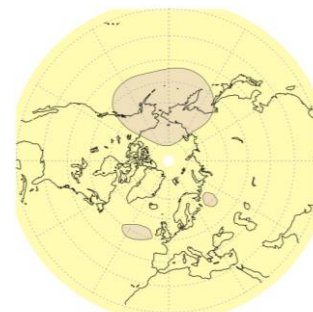
(h) Feb signal variance TroInd
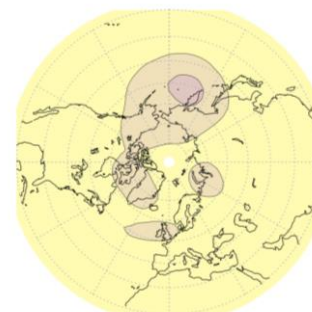
(i) Mar signal variance TroInd
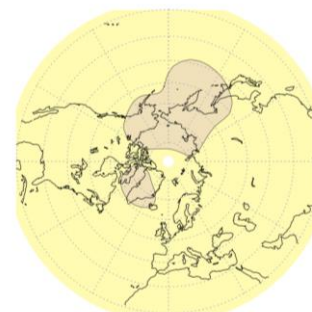
(j) Jan signal variance TroPac
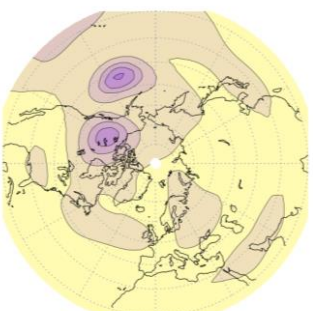
(k) Feb signal variance TroPac

(l) Mar signal variance TroPac

(m) Jan signal variance Tropics   (n) Feb signal variance Tropics   (o) Mar signal variance Tropics

(p) Jan signal variance Clim   (r) Feb signal variance Clim   (s) Mar signal variance Clim
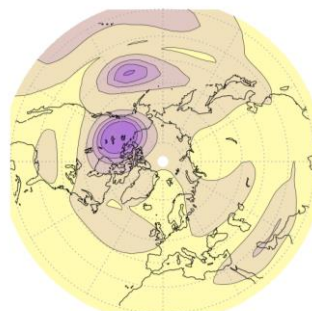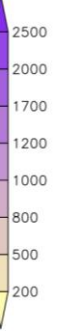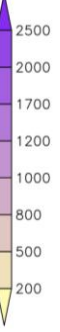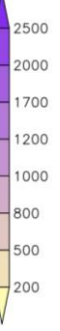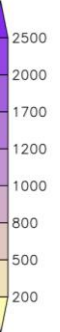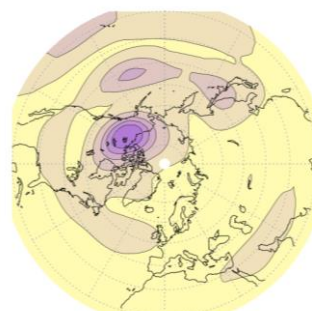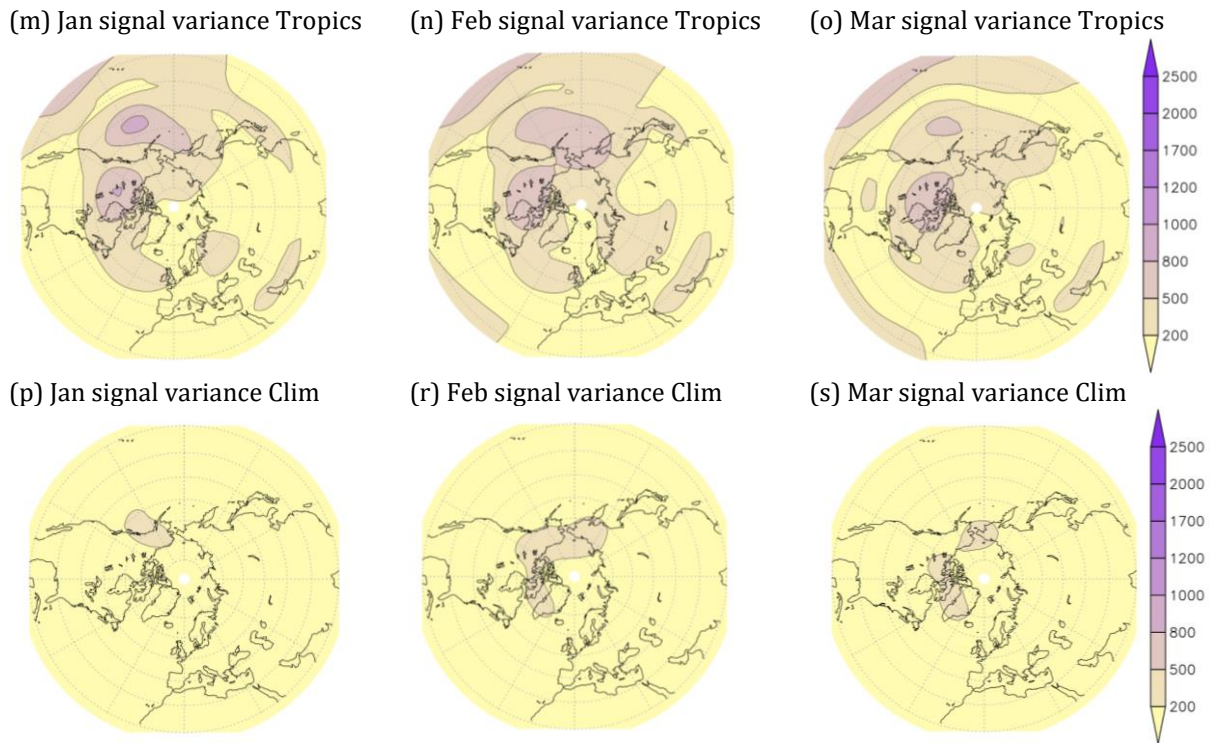
Appendix Figure C1 Signal variance of geopotential heights at 200 hPa [m^2] in January (left), February (middle), and March (right) for the whole 156-year period (1855-2010) in the ICTP AGCM experiments: Ctrl, TroAtl, TroInd, TroPac, Tropics, and Clim, respectively.

(a) Jan ENSO sig var Ctrl   (b) Feb ENSO sig var Ctrl   (c) Mar ENSO sig var Ctrl

(d) Jan ENSO sig var TroAtl   (e) Feb ENSO sig var TroAtl   (f) Mar ENSO sig var TroAtl
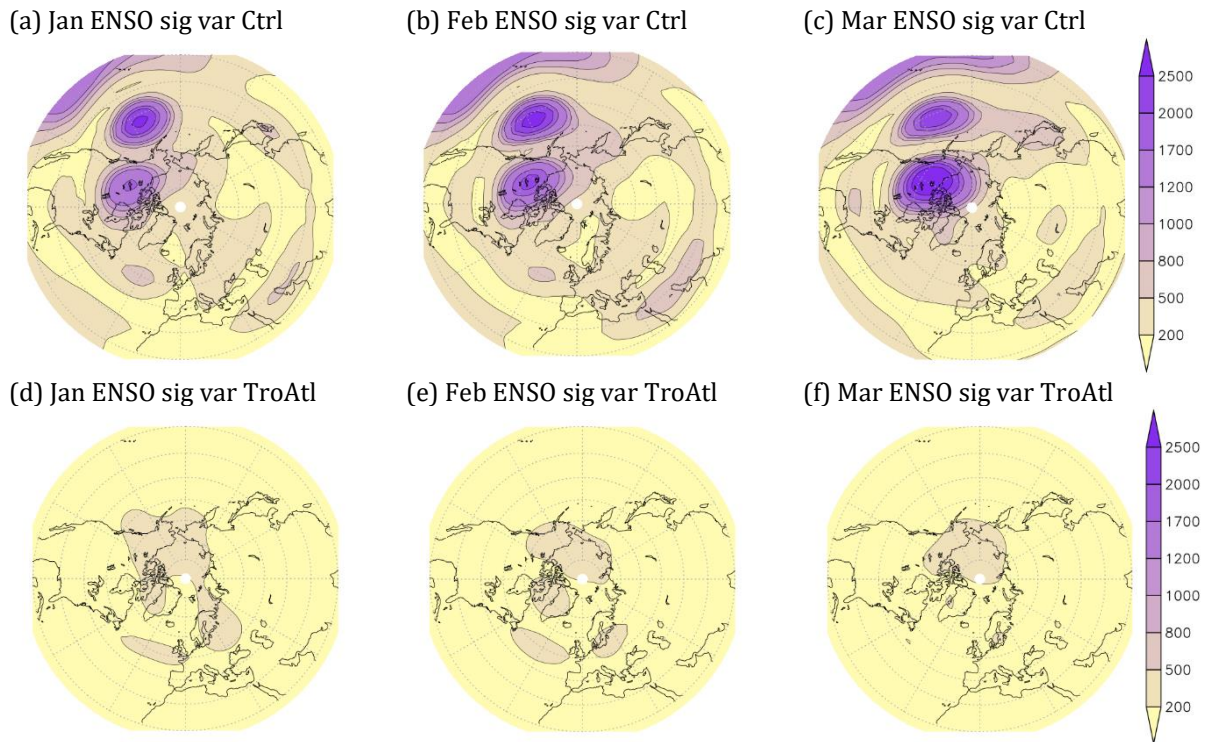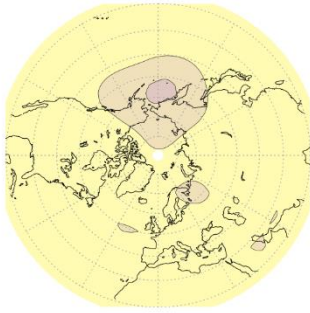
(g) Jan ENSO sig var TroInd (h) Feb ENSO sig var TroInd (i) Mar ENSO sig var TroInd
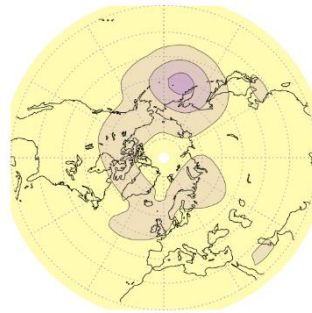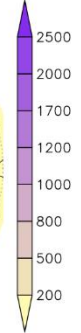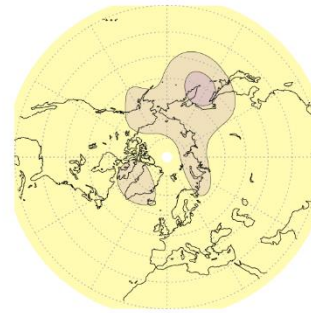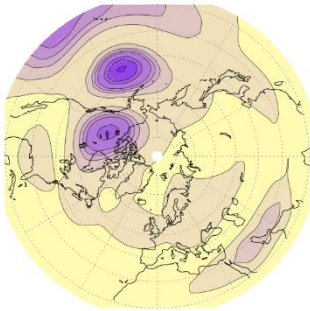
(i) Jan ENSO sig var TroPac (j) Feb ENSO sig var TroPac (l) Mar ENSO sig var TroPac
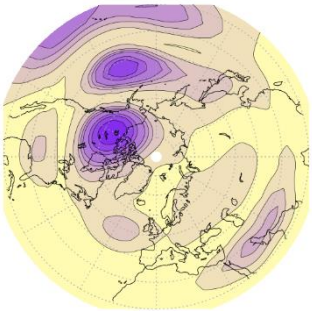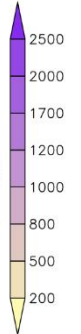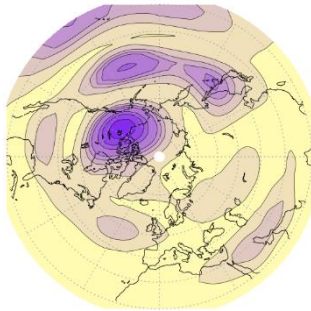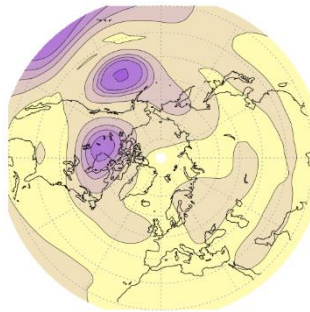
(m) Jan ENSO sig var Tropics (n) Feb ENSO sig var Tropics (o) Mar ENSO sig var Tropics
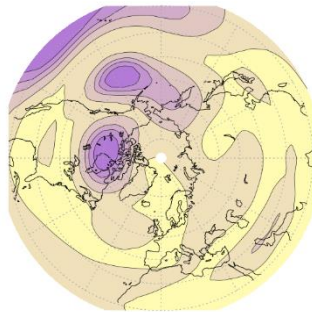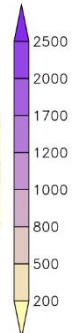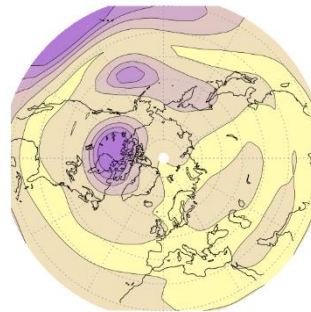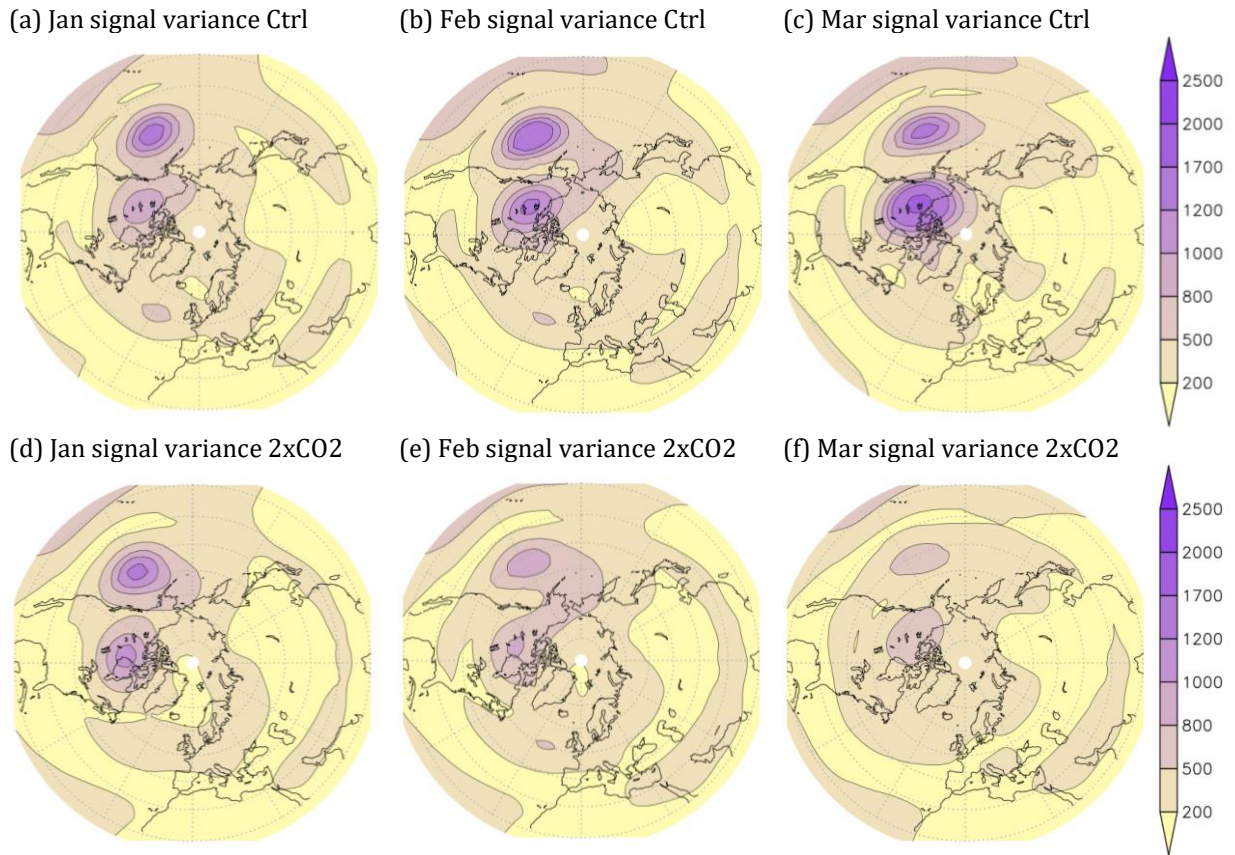
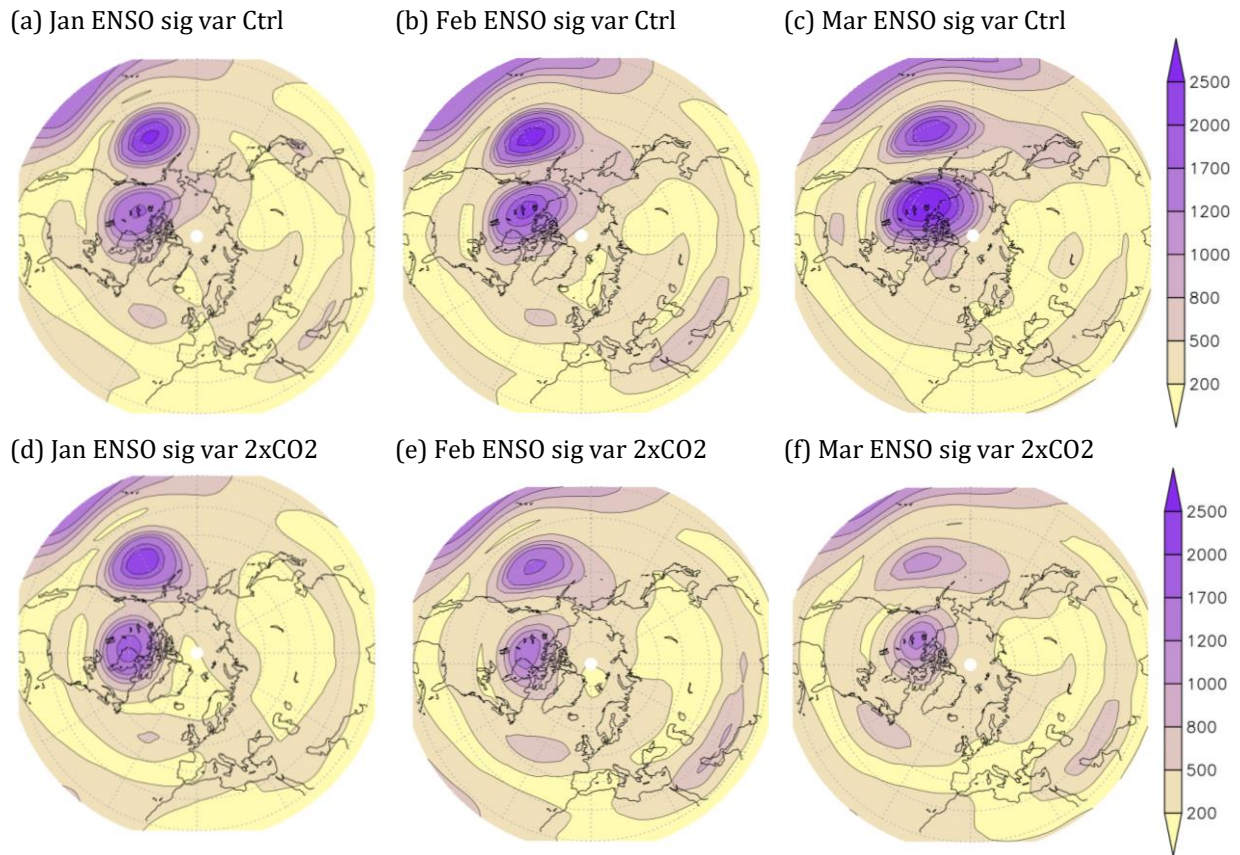(p) Jan ENSO sig var Clim (r) Feb ENSO sig var Clim (s) Mar ENSO sig var Clim
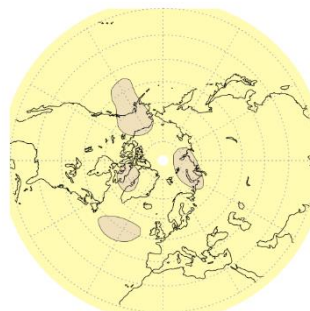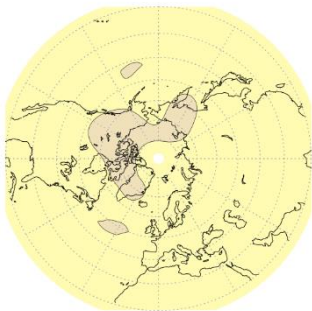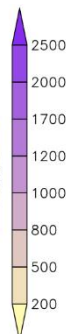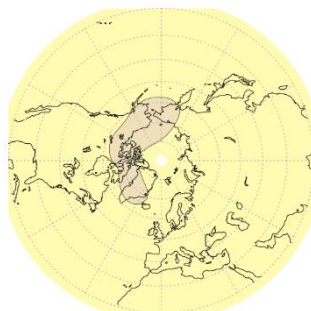
Appendix Figure C2 Signal variance (sig var) of geopotential heights at 200 hPa [m^2] in the 53 ENSO years in January (left), February (middle), and March (right) in the ICTP AGCM experiments: Ctrl, TroAtl, TroInd, TroPac, Tropics, and Clim, respectively. ENSO years were selected from the 156 years (1855-2010) according to the strength of the Niño3.4 index in the JFM season.

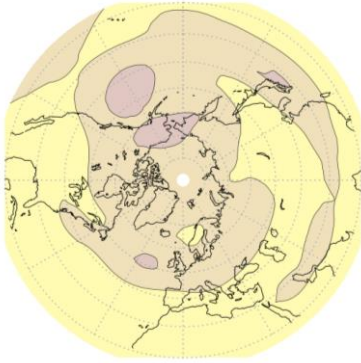(a) Jan non-ENSO sig var Ctrl (b) Feb non-ENSO sig var Ctrl (c) Mar non-ENSO sig var Ctrl
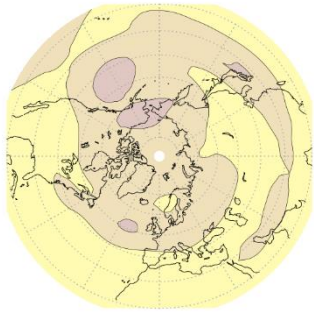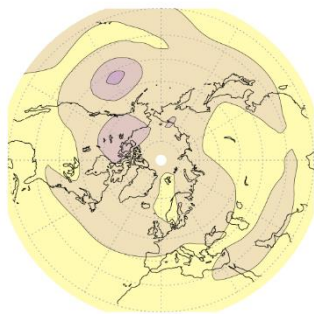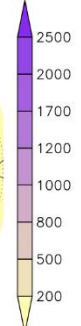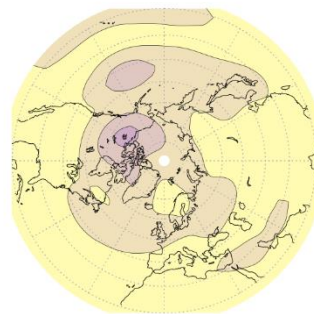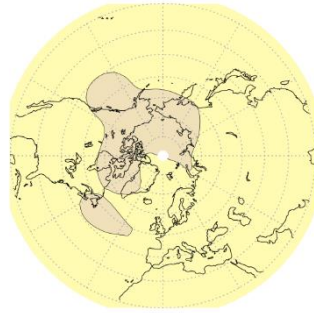
(d) Jan non-ENSO sig var TroAtl (e) Feb non-ENSO sig var TroAtl (f) Mar non-ENSO sig var TroAtl
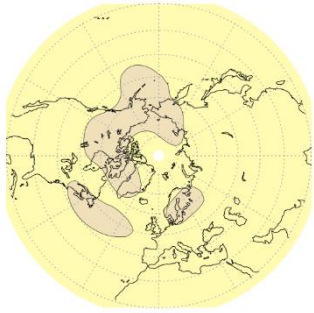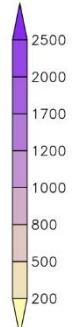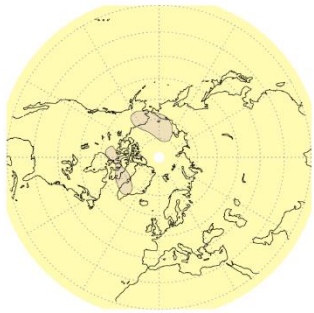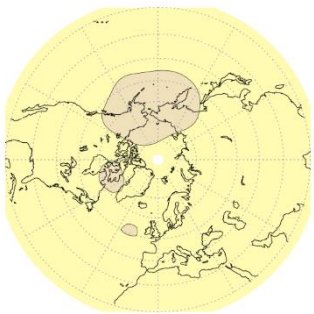
(g) Jan non-ENSO sig var TroInd (h)Feb non-ENSO sig var TroInd (i) Mar non-ENSO sig var TroInd
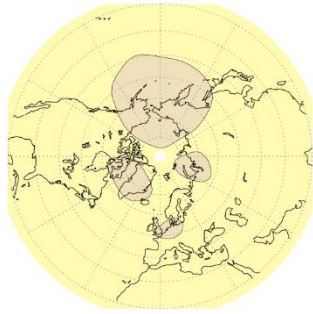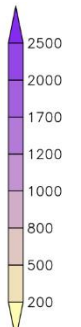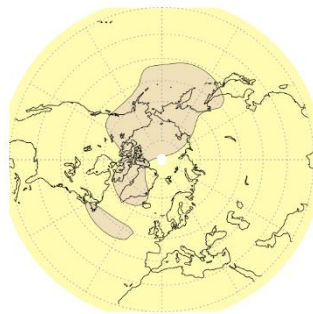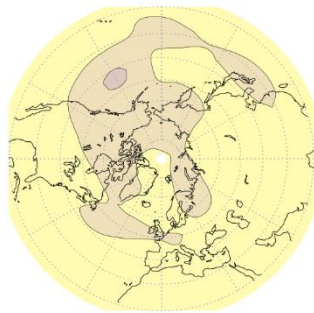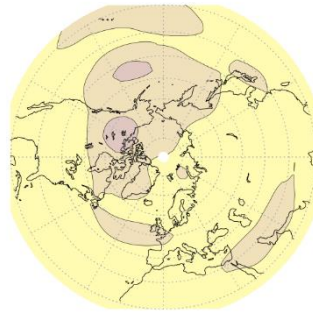
(i) Jan non-ENSO sig var TroPac (j) Feb non-ENSO sig var TroPac (l) Mar non-ENSO sig var TroPac
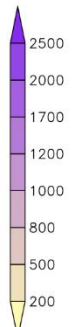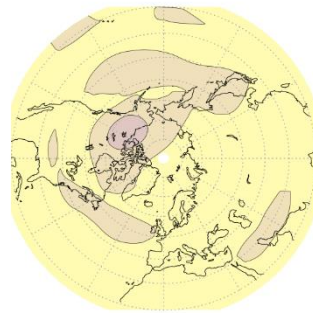
(m) Jan non-ENSO sig var Tropics
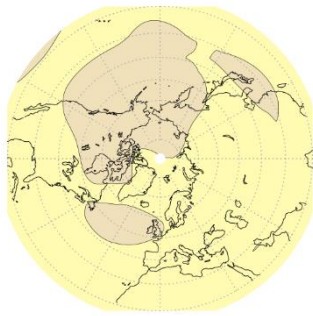
(n) Feb non-ENSO sig var Tropics
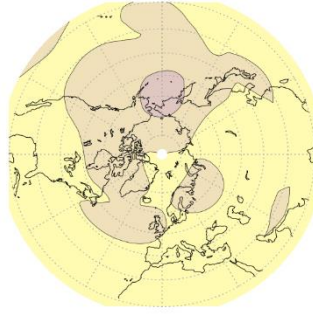
(o) Mar non-ENSO sig var Tropics
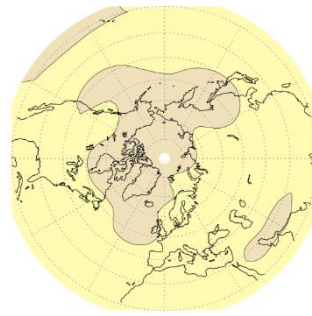
(p) Jan non-ENSO sig var Clim
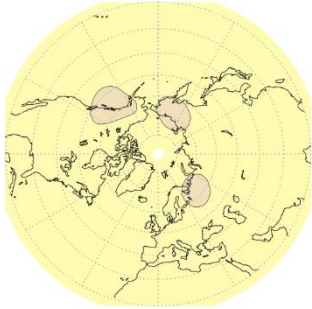
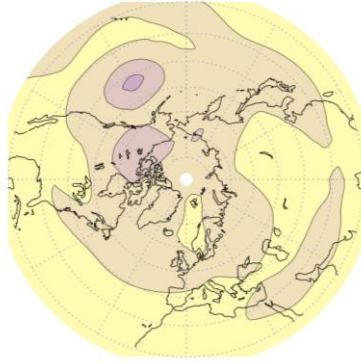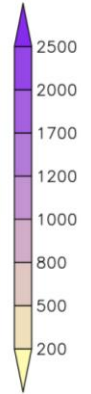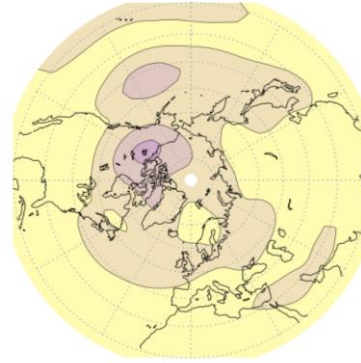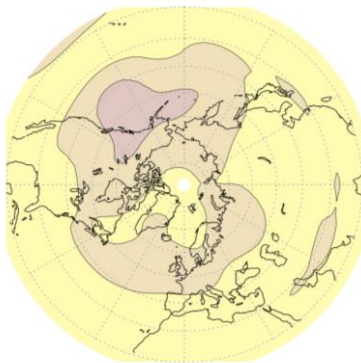(r) Feb non-ENSO sig var Clim
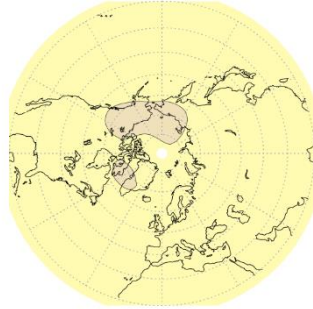
(s) Mar non-ENSO sig var Clim
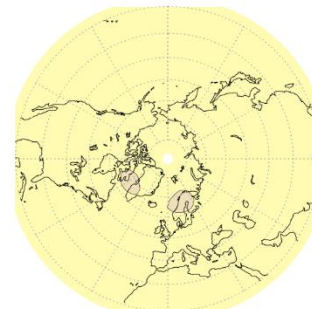
Appendix Figure C3 Signal variance (sig var) of geopotential heights at 200 hPa [m²] in the 57 non-ENSO years in January (left), February (middle), and March (right) in the ICTP AGCM experiments: Ctrl, TroAtl, TroInd, TroPac, Tropics, and Clim, respectively. The non-ENSO years were selected from 156 years (1855-2010) according to the strength of the Niño3.4 index in the JFM season.

Appendix D

(a) Jan signal variance Ctrl   (b) Feb signal variance Ctrl   (c) Mar signal variance Ctrl

(d) Jan signal variance 2xCO2   (e) Feb signal variance 2xCO2   (f) Mar signal variance 2xCO2

Appendix Figure D1 Signal variance (sig var) of geopotential heights at 200 hPa (GH200) [m^2] in all 156 years (1855-2010) in January (left), February (middle), and March (right)) in the Ctrl and 2xCO2 ICTP AGCM experiments.

(a) Jan ENSO sig var Ctrl   (b) Feb ENSO sig var Ctrl   (c) Mar ENSO sig var Ctrl
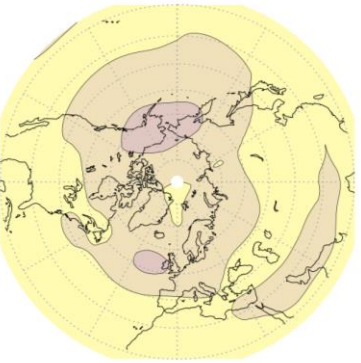
(d) Jan ENSO sig var 2xCO2   (e) Feb ENSO sig var 2xCO2   (f) Mar ENSO sig var 2xCO2

Appendix Figure D2 Signal variance (sig var) of geopotential heights at 200 hPa (GH200) [m^2] in the 53 ENSO years in January (left), February (middle), and March (right) in the Ctrl and 2xCO2 ICTP AGCM experiments. The ENSO years were selected from the 156 years (1855-2010) according to the strength of the Niño3.4 index in the JFM season.

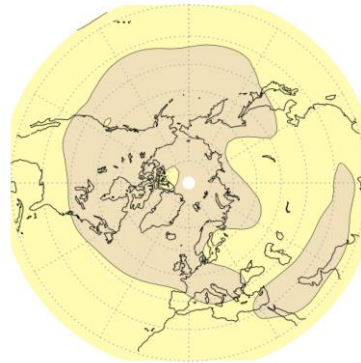(a) Jan non-ENSO sig var Ctrl   (b) Feb non-ENSO sig var Ctrl   (c) Mar non-ENSO sig var Ctrl

(d) Jan non-ENSO sig var 2xCO2   (e) Feb non-ENSO sig var 2xCO2   (f) Mar non-ENSO sig var 2xCO2
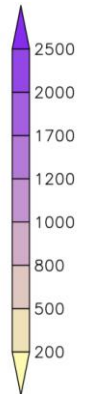
Appendix Figure D3 Signal variance (sig var) of geopotential heights at 200 hPa (GH200) [m^2] in the 57 non-ENSO years in January (left), February (middle), and March (right) in the Ctrl and 2xCO2 ICTP AGCM experiments. The non-ENSO years were selected from the 156 years (1855-2010) according to the strength of the Niño3.4 index in the JFM season.

Acknowledgements

Curriculum vitae

Sara Ivasić   sara.ivasic@gfz.hr

Education

2018-   Doctoral study in physics, module geophysics, Faculty of Science, University of Zagreb

2015 – 2018   Graduate course in physics - geophysics, module: meteorology and physical oceanography, Faculty of Science, University of Zagreb

2011– 2015   Undergraduate course in physics, Faculty of Science, University of Zagreb

Work experience

2018-   Research assistant on the project CroClimGoGreen, Department of Geophysics, Faculty of Science, University of Zagreb

Teaching assistant experience

2020- 2022   Dynamic meteorology I and II

Awards and scholarships

2022   Young Meteorologist Award by Croatian Meteorological Society

2010   City of Zagreb Scholarship

Skills

Programming   GrADS, Python, Matlab, CDO

Data analysis   Numerical model output analysis, Time series analysis

Applications   Microsoft Office, Libre Office

Professional training

2019   2nd Summer School on Theory, Mechanisms and Hierarchical Modelling of Climate Dynamics: Convective Organization and Climate Sensitivity, ICTP, Trieste, Italy

2022   3rd ICTP Summer School on Theory, Mechanisms and Hierarchical Modelling of Climate Dynamics: Convective Organization and Climate Sensitivity, ICTP, Trieste, Italy

Selected conference and workshop presentations

2022   *Impact of tropical SSTs on the variability and predictable components of late-winter atmospheric circulation in the North Atlantic-European region*, EMS Annual Meeting 2022, EMS2022, Bonn, Germany

2022   *Impact of tropical SSTs on the late-winter signal over the North Atlantic-European region*, Challenges in Meteorology 8, Zagreb, Croatia

2021   *Recent weakening in the winter ENSO teleconnection over the North Atlantic-European region*, EMS Annual Meeting, EMS2021

2020   *Impact of tropical ocean SSTs on the variability and predictable components of seasonal atmospheric circulation in the North Atlantic-European area*, Challenges in Meteorology 7, Zagreb, Croatia

2018   *ENSO and NAO influence on climate variability in Europe*, Challenges in Meteorology 6, Zagreb, Croatia

Scientific memberships

2022-   American Geophysical Union

2021-   Croatian Meteorological Society

List of publications

Original scientific papers in WoS database journals

1. Ivasić S, Herceg-Bulić I, King MP (2021) Recent weakening in the winter ENSO teleconnection over the North Atlantic-European region. *Clim Dyn.* https://doi.org/10.1007/s00382-021-05783-z

2. Ivasić S, Herceg-Bulić I (2022) A modelling study of the impact of tropical SSTs on the variability and predictable components of seasonal atmospheric circulation in the North Atlantic–European region. *Clim Dyn.* https://doi.org/10.1007/s00382-022-06357-3